JOURNAL OF PETROLOGY | VOLUME 48 | NUMBER 9 | PAGES 1641–1680 | 2007 | doi:10.1093/petrology/egm031

Whole-rock, Phosphate, and Silicate Compositional Trends across an Amphibolite- to Granulite-facies Transition, Tamil Nadu, India

EDWARD C. HANSEN[1] AND DANIEL E. HARLOV[2]*

[1]DEPARTMENT OF GEOLOGY, HOPE COLLEGE, HOLLAND, MI 49422, USA

[2]GEOFORSCHUNGSZENTRUM, TELEGRAFENBERG, D-14473 POTSDAM, GERMANY

RECEIVED MAY 28, 2006; ACCEPTED MAY 23, 2007
ADVANCE ACCESS PUBLICATION AUGUST 3, 2007

Chemical trends from north (amphibolite facies) to south (granulite facies) along a 95 km traverse in Tamil Nadu, Southern India, include: whole-rock depletion of Rb, Cs, Th and U, enrichment in Ti and F, and depletion in Fe and Mn in biotite and amphibole; increases in Al and decreases in Mn in orthopyroxene; enrichment of fluorapatite in F. K-feldspar blebs are widespread along quartz–plagioclase grain boundaries, and could indicate either partial melting or metasomatism. In the northernmost portion of the traverse the principal rare earth element (REE)-bearing minerals are allanite and titanite. South of a clinopyroxene isograd, monazite grains independent of fluorapatite are the major REE- and Th-bearing phase. Further south independent monazite is rare but Th-free monazite inclusions are common in fluorapatite. During prograde metamorphism, independent monazite was replaced by REE-rich fluorapatite in which the monazite inclusions later formed. The loss of independent monazite was accompanied by a loss of whole-rock Th and possibly a small depletion in light REE. Most mineralogical features along the traverse can be accounted for by progressive dehydration and oxidation reactions. Trace-element depletion is best explained by the action of an externally derived low H_2O activity brine migrating from a source at greater depth, possibly preceded or accompanied by partial melting.

KEY WORDS: *granulite facies; charnockite; metasomatism; Archean; Tamil Nadu, India; fluorapatite; monazite; allanite; titanite; biotite*

INTRODUCTION

Granulite-facies metamorphism is essentially an act of dehydration in which hydrous minerals, such as amphibole and sheet silicates, are transformed into non-hydrous minerals, such as pyroxenes, aluminosilicates and feldspar, liberating a fluid or melt, generally at temperatures and pressures >600°C and 400 MPa. High temperatures recorded in many granulite-facies orthogneisses indicate that partial melting, perhaps driven by magma intrusion, may also be important in the metamorphism of these rocks (Frost & Frost, 1987; Pattison *et al.*, 2003). However, there is also evidence that in intermediate and metabasite rocks granulite-facies metamorphism can occur by solid-state dehydration, induced by low H_2O activity fluids (e.g. Harlov & Förster, 2002*a*, 2002*b*; Harlov *et al.*, 2006*a*) via two simple pyroxene-forming reactions:

$$\underset{\text{biotite}}{\mathrm{K(Fe,Mg)_3AlSi_3O_{10}(OH)_2}} + 3\,\underset{\text{quartz}}{\mathrm{SiO_2}} = 3\,\underset{\text{orthopyroxene}}{\mathrm{(Fe,Mg)SiO_3}} + \underset{\text{K-feldspar}}{\mathrm{KAlSi_3O_8}} + \mathrm{H_2O} \quad (1)$$

and

$$\underset{\text{amphibole}}{\mathrm{Ca_2(Fe,Mg)_5Si_8O_{22}(OH)_2}} = 2\,\underset{\text{clinopyroxene}}{\mathrm{Ca(Fe,Mg)Si_2O_6}} + 3\,\underset{\text{orthopyroxene}}{\mathrm{(Fe,Mg)SiO_3}} + \underset{\text{quartz}}{\mathrm{SiO_2}} + \mathrm{H_2O}. \quad (2)$$

Many granulite-facies rocks have unusually low abundances of some large ion lithophile elements (LILE) including Rb, Cs, U, and Th (Rudnick & Presper, 1990). The rare earth element (REE) trends are not as clear, although Stähle *et al.* (1987), Raith & Srikantappa (1993) and Harlov *et al.* (2006*a*) presented evidence for the loss of heavy REE (HREE) in localized granulite-facies dehydration zones. Models explaining low trace-element

*Corresponding author. E-mail: dharlov@gfz-potsdam.de

abundances in granulite-facies rocks have generally focused on removal by a partial melt (Pride & Muecke, 1980), partitioning into a fluid phase (Collerson & Fryer, 1978), or metamorphism of a protolith already depleted in these elements (Rollinson & Tarney, 2005). Low trace-element abundances in a rock can reflect low modal abundances of the host minerals (Rudnick & Presper, 1990), low abundances of these elements in their hosts, or both (Hansen *et al.*, 2002). Which of these cases holds is critical in constraining the mechanism of trace-element depletion. The stability and composition of accessory minerals can play a dominant role in the behaviour of trace elements during high-grade metamorphism (Rudnick *et al.*, 1985), and phosphates can be particularly important for REE and Th.

Harlov & Förster (2002*a*, 2002*b*) studied silicate and phosphate textures and composition across both a local and a regional dehydration zone. The local zone occurs over 85 cm in the Seward Peninsula, Alaska, at the contact between a tonalitic orthogneiss and a marble (Todd & Evans, 1994). The regional zone consists of metabasites over a 12 km traverse, representing a 3–4 km thick crustal section in the Ivrea–Verbano zone, northern Italy. The two dehydration zones have a number of common features including K-feldspar micro-veins (referred to as K-feldspar blebs in this study) along quartz and plagioclase grain boundaries, replacement antiperthite in a selective scattering of plagioclase grains, biotite enriched in Ti and F, an increase of F in fluorapatite with increasing degree of dehydration, and the presence of monazite and/or xenotime inclusions in fluorapatite.

In this study the same techniques as used by Harlov & Förster (2002*a*, 2002*b*) are applied to intermediate and felsic gneisses over a 95 km traverse in northern Tamil Nadu. This traverse represents roughly a 10–15 km thick cross-section of crust ranging from high-grade granulite-facies to middle amphibolite-facies grade. The rocks in this region originated during a major period of continental crust formation in the late Archean. In northern Tamil Nadu metamorphism closely followed crustal accretion (Peucat *et al.*, 1993). A better understanding of the processes that operated during this period is critical to understanding the formation and evolution of the continental crust. One goal of this study is to determine whether the features identified by Harlov & Förster (2002*a*, 2002*b*) also occur in a larger-scale, regional, high-grade, metamorphic terrane that comprises a cross-section of Archean crust. A second goal of this study is to expand on studies of amphibolite- to granulite-facies transitions in general by including extensive whole-rock trace-element analyses for each sample across the traverse. Taken together, the information on trends in mineral associations, textures, and compositions, as well as the whole-rock composition, puts important constraints on the processes of trace-element depletion and their links to granulite-facies metamorphism.

GEOLOGY

This study (Fig. 1) focuses on a 95 km traverse, which begins 5 km north of the town of Krishnagiri and ends at the southern terminus of the Shevaroy Hills north of the city of Salem in the state of Tamil Nadu, India. The dominant rocks in the area are intermediate to felsic orthogneisses (Condie *et al.*, 1982; Rameshwar Rao *et al.*, 1991*a*), with the proportion of felsic rocks decreasing towards the south (Hansen *et al.*, 1995). Subordinate amounts of mafic gneisses and minor amounts of metasediments also occur. Peucat *et al.* (1993) showed that metamorphism in the northern portion of the traverse occurred close to 2·5 Ga shortly after crustal accretion at 2·7–2·5 Ga. Geochronology is lacking in the southern portion, but Hansen *et al.* (1995) noted that there appears to be an unbroken metamorphic transition to the southern margin of the area. Roughly 10 km to the south of this margin the metamorphic transition is cut off by a major shear zone of probable Proterozoic age (Fig. 1).

Hansen *et al.* (1995) divided the rocks in the study area from north to south into Amphibolite-Facies Gneisses; a Clinopyroxene Zone where clinopyroxene is the predominant ferromagnesian mineral in the orthogneiss; Lowland Charnockites in which the proportion of orthopyroxene to biotite and amphibole increases southwards; and the Highland Charnockites of the Shevaroy Hills area. In this study a modification of this scheme is used (see also Harlov & Hansen, 2005).

The Northern Amphibolite-Facies Zone (NAF) includes all rocks north of the first appearance of orthopyroxene in the felsic and intermediate orthogneisses (Fig. 1). The quartzo-feldspathic rocks in this zone all contain biotite, usually with amphibole. Epidote occurs in the northern half of the NAF. Clinopyroxene appears in the southern half of the zone.

The Central Granulite-Facies Zone (CGF) begins with the first appearance of orthopyroxene in intermediate and felsic orthogneisses several kilometres to the south of the clinopyroxene isograd (Fig. 1). Clinopyroxene is the dominant pyroxene in the northernmost part of this zone but orthopyroxene becomes more abundant southwards. The abundances of biotite and amphibole decrease to the south, indicating progressively greater amounts of dehydration (Hansen *et al.*, 1995, 2002). Condie *et al.* (1982) and Condie & Allen (1984) found no evidence of trace-element depletion in the rocks from the northernmost section of the CGF. Rollinson & Tarney (2005) have used this observation as one of their arguments against trace-element depletion during granulite-facies metamorphism. However, Rameshwar Rao *et al.* (1991*a*), and Hansen *et al.* (1995, 2002) have shown that depletions

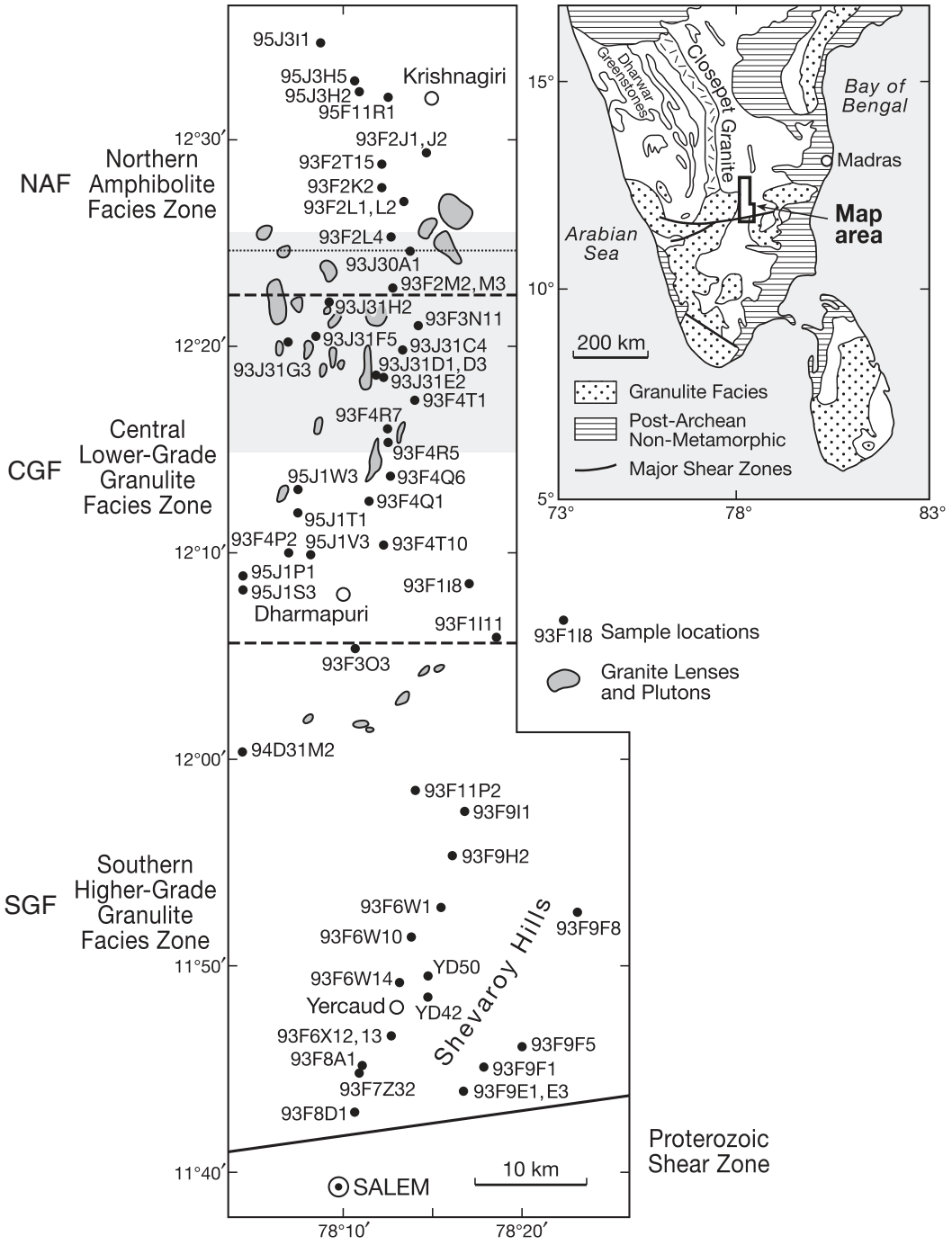

Fig. 1. Map of the Krishnagiri–Dharmapuri–Shevaroy area (Krishnagiri–Salem traverse) showing sample locations for the entire traverse. Also shown are petrological zones representing progressive metamorphic terranes starting with the southern higher-grade granulite-facies zone (SGF) through the central lower-grade granulite-facies zone (CGF) to the northern amphibolite-facies zone (NAF). Small, enclosed areas are mappable granitic bodies, mostly from Condie *et al.* (1982) and Rameshwar Rao *et al.* (1991*b*). The dotted line is the clinopyroxene isograd in felsic and intermediate orthogneisses. The dashed line just to the south of it (northern boundary of the CGF) is the orthopyroxene isograd for these same compositions. The lightly shaded area is the region in which independent monazite grains are relatively common. It also corresponds roughly to the clinopyroxene-rich zone of Hansen *et al.* (1995). The second dashed line between 12° 10′ and 12° 00′ marks the approximate boundary between the SGF and CGF. The principal country rock in all the zones is a quartzo-feldspathic gneiss. The Krishnagiri–Dharmapuri–Shevaroy area is indicated by a bold outline on the geological map insert of the Indian subcontinent.

in Rb, Cs, U, and Th appear further south in the middle of the CGF.

The Southern Granulite-Facies Zone (SGF) roughly coincides with the Highland Charnockites of Hansen *et al.* (1995) and Harlov *et al.* (1997) (Fig. 1). Many of the rocks in this zone contain only minor amounts of amphibole and biotite. Garnet is widespread, but not ubiquitous, in felsic and intermediate orthogneisses in the southernmost SGF; that is, the last 10 km of the traverse going southwards. It is rare in compositionally similar rocks in the northern SGF and totally absent in the CGF orthogneisses.

Geothermometry and geobarometery indicate paleopressures and temperatures of about 400 MPa and 600°C (Rameshwar Rao *et al.*, 1991*b*) in the NAF and 800 MPa (Gt–Opx–Plag–Qtz) and 850°C (Gt–Opx) at the southern end (Hansen *et al.*, 1995; Harlov *et al.*, 1997). Thus the northern portion of the traverse represents significantly higher crustal levels (13 km depth) than does the southern portion (25 km depth), indicating that the traverse represents a 12 km thick cross-section of lower Archean crust. Two-pyroxene thermometry indicates a relatively constant temperature of 780°C (±25°C) throughout the CGF and somewhat higher temperatures (840°C ± 70°C) for the SGF (Harlov & Hansen, 2005).

ANALYTICAL TECHNIQUES

Sample selection

Fifty samples were chosen for detailed study of the fluorapatite, monazite, allanite, titanite, biotite, and amphibole compositions across the SGF, CGF, and NAF zones. Samples were selected with regard to their major-element whole-rock compositions, which range from intermediate to felsic, as well as their positions along the traverse. In those cases in which whole-rock analyses were not available, the decision on whether or not a sample was intermediate or felsic was made based on its mineralogy, determined from petrographic examination of thin sections. A detailed description of the accessory mineralogy of these samples is given in Table 1.

Whole-rock analysis

Whole-rock analyses were carried out on kilogram-size samples. The major-element analyses were performed by X-ray fluorescence and have been described by Hansen *et al.* (1995). Trace-element analyses (Table 2) for approximately 50% of the samples were performed at Activation Laboratories LTD in Lancaster, Ontario using a combination of instrumental neutron activation analysis and inductively coupled-plasma mass spectrometry (ICP-MS). Detection limits are estimated to be 2 ppm for Pb, 3 ppm for Zr, 1 ppm for Hf, 2 ppm for Rb, 2 ppm for Sr, 0·1 ppm for all the REE except for Eu, Ho, and Lu (0·05 ppm), and 0·1 ppm for U and Th. Details of the analytical techniques are available from the company website at www.actlabs.com. The remaining 50% of the whole-rock trace-element analyses were carried out by ICP-MS at the GeoForschungsZentrum Potsdam (indicated by an asterisk in Table 2). Technique and uncertainties have been outlined by Dulski (2001).

Mineral analysis

Microscopic investigation was carried out using both transmitted light and back-scattered electron (BSE) imaging. BSE images were made on a Zeiss DSM 962 digital scanning electron microscope with either 15 or 20 kV acceleration voltage.

Electron microprobe analysis (EMPA) was carried out using the CAMECA SX50 and SX100 electron microprobes at the GeoForschungsZentrum Potsdam. The Cameca PAP program was used for matrix correction (Pouchou & Pichoir, 1985). Analytical conditions and standards are given in Table 3. Relative errors in EMPA are estimated to be <1% at the >10 wt % level, 5–10% at the 1 wt % level, 10–20% at the 0·2 to 1 wt % level, and 20–40% at the <0·1 wt % level. For concentrations below 0·1 wt %, the analytical precision for the actinides and Pb is much better (i.e. ~10%). Detection limits were ~500 ppm for (Y + REE), 200–300 ppm for Th and U, and 100 ppm for the remaining elements. Average or typical analyses are given of biotite (Table 4), amphibole (Table 5), fluorapatite (Table 6), monazite (Tables 7 and 8), allanite (Table 9), and titanite (Table 11). The full dataset is available for downloading as a set of Electronic Appendices from the *Journal of Petrology* website at http://www.petrology.oxfordjournals.org.

Anywhere from four to nine biotite or amphibole grains, scattered evenly over the length and breadth of the thin section, were analysed per sample. The one exception is 93 F8 D1, where only one biotite grain was found. To ensure that the relative differences observed are correct within EMPA error, silicate analyses per sample were obtained during a single measuring session including multiple checks of the calibration. H_2O concentrations in the biotite and amphibole were estimated by assuming that the sum of F, Cl, and OH in the calculated mineral formula is equal to four.

For most samples and elements the fluorapatite analyses listed in Table 6 represent the average of between four and 11 grains evenly scattered over the thin section. The one exception is F. Because F X-ray excitation tends to increase with time during EMPA (Stormer *et al.*, 1993), the fluorapatite grain in each sample with the lowest F concentration was chosen as the value of F included with the mean fluorapatite value in Table 6. Whenever possible, elongated fluorapatite grains were chosen for analysis. The assumption made was that, because such grains are roughly oriented parallel to [0001], this would minimize the increase in F X-ray excitation with time

Table 1: Mineralogy of the Tamil Nadu samples

	Sample	Zone	*D* (km)	Ep	Opx	Cpx	Amph	Bt	Kfs blebs*	Titanite	Allanite	FAp	Monazite
1	95 J3 I1	NAF	0	X			X	X	coarse	X	D	X	
2	95 J3 H5	NAF	3·53	X				X	coarse	X		X	
3	95 J3 H2	NAF	4·45	X			X	X		X		X	
4	93 F11 R1	NAF	4·82	X				X		X		X	
5	93 F2 J1	NAF	9·83				X	X	coarse	X	D	X	
6	93 F2 J2	NAF	9·83					X	coarse			X	
7	93 F2 K2	NAF	12·99					X	coarse	X	D	X	
8	93 F2 L1	NAF	14·30					X		X	D, RA	X†	SIA
9	93 F2 L2	NAF	14·30					X	coarse	X		X	
10	93 F2 L4	NAF	17·44				X	X			D, RA	X	D, SIA, LIA, RA
11	93 J30 A1	NAF	18·74				X	X	fine		RA, RM	X	D, SIA, LIA, RA
12	93 F2 M2	NAF	22·08			X	X	X			RA	X	D, SIA, LIA, RA
13	93 F2 M3	NAF	22·08			X		X			RA	X	D, SIA, LIA, RA
14	93 J31 H2	CGF	23·19		X	X	X	X			D	X	SIA, LIA, RA
15	93 F3 N11	CGF	25·42		X	X		X	moderate		RA	X	D, SIA, LIA, RA
16	93 J31 F5	CGF	26·35				X	X	coarse	X	D, RA	X‡	D, SIA, RA
17	93 J31 G3	CGF	26·90			X		X	coarse		RA	X	SIA, LIA, RA
18	93 J31 C4	CGF	27·64			X		X			RA	X	D, SIA, LIA, RA
19	93 J31 D1	CGF	29·87		X	X		X	coarse, RAP		RA	X	D, SIA, LIA, RA
20	93 J31 D3	CGF	29·87			X		X	coarse		RA	X	D, SIA, LIA, RA
21	93 J31 E2	CGF	30·06		X	X		X			RA	X	D, SIA, LIA, RA
22	93 F4 T1	CGF	32·10			X		X	coarse		RA	X	D, SIA, LIA, RA
23	93 F4 R7	CGF	34·70		X	X		X	coarse		RA	X	D, SIA, LIA, RA
24	93 F4 R5	CGF	35·99			X		X	coarse		RA	X	D, SIA, LIA, RA
25	93 F4 Q6	CGF	38·96				X	X	moderate, RAP		RA	X	SIA, LIA, RA
26	95 J1 W3	CGF	40·07		X	X		X			RA	X	D, SIA, LIA, RA
27	93 F4 Q1	CGF	41·19		X		X	X	coarse		RA	X	SIA, LIA, RA
28	93 F4 T10	CGF	45·10		X		X	X	coarse		RA (rare)	X	SIA, LIA, RA
29	93 F4 P2	CGF	45·82		X	X	X	X			RA (rare)	X	SIA, LIA, RA
30	95 J1 V3	CGF	46·01			X		X	moderate, RAP		RA	X	SIA, LIA
31	93 F1 I8	CGF	48·60		X	X	X	X	coarse			X	LIA, RA
32	95 J1 S3	CGF	49·17		X	X	X	X	coarse		RA (rare)	X	SIA, LIA, RA
33	93 F3 O3	SGF	54·36		X	X	X	X	coarse, RAP		RA	X	SIA, RA
34	94 D31 M2	SGF	63·82		X	X		X	coarse, RAP			X	SIA, RA
35	93 F11 P2	SGF	67·16		X			X	coarse, RAP		RA	X	SIA, RA
36	93 F9 I1	SGF	69·02	X	X			X	moderate			X	D, SIA, RA
37	93 F9 H2	SGF	73·10		X	X	X		RAP		RA	X	SIA, LIA, RA
38	93 F6 W1	SGF	77·73		X			X	moderate		RA	X	SIA, RA
39	93 F9 F8	SGF	78·11		X		X	X	moderate		RA	X	D, SIA, RA
40	93 F6 W10	SGF	80·33		X			X	moderate, RAP		RA	X	SIA, RA
41	YD50	SGF	83·86		X			X					
42	93 F6 W14	SGF	84·42		X		X		moderate		RA	X	SIA, RA
43	YD42	SGF	85·71		X			X	coarse, RAP		RA	X	LIA, RA
44	93 F6 X13	SGF	89·24		X		X		coarse, RAP		RA	X	LIA, RA
45	93 F9 F5	SGF	90·17		X	X	X	X	coarse		RA	X	LIA, RA
46	93 F8 A1	SGF	91·84		X	X			RAP		RA	X	SIA, LIA, RA

(continued)

Table 1: Continued

	Sample	Zone	*D* (km)	Ep	Opx	Cpx	Amph	Bt	Kfs blebs*	Titanite	Allanite	FAp	Monazite
47	93 F9 F1	SGF	92·02		X		X	X	coarse		RA	X	LIA, RA
48	93 F7 Z32	SGF	92·57		X		X		coarse, RAP		RA	X	SIA, LIA
49	93 F9 E3	SGF	94·20	X	X			X	coarse		RA	X	RA
50	93 F8 D1	SGF	94·99	X	X			X	coarse		RA	X	

*Kfs blebs are primarily found along plagioclase–quartz grain boundaries.
†A sparse scattering of small monazite inclusions are found in one fluorapatite grain.
‡Fluorapatite grains are magmatically zoned.
RAP, replacement antiperthite; D, discrete grain; SIA, numerous small Mnz inclusions in fluorapatite; LIA, large Mnz inclusions in fluorapatite; RA, rim grain on fluorapatite; RM, rim grain on monazite; Ep, epidote; Opx, orthopyroxene; Cpx, clinopyroxene; Amph, amphibole; Bt, biotite; Kfs, K-feldspar; FAp, fluorapatite.

during EMPA (Stormer *et al.*, 1993; Pyle *et al.*, 2002). Each fluorapatite grain was examined in BSE mode and areas free of monazite inclusions were chosen for analysis. Yttrium + REE analyses are listed in Table 6 only if the mean analysis was above the detection limits for the (Y + REE) and if more than half the individual analyses were above this detection limit. The last criterion was to limit the effect of the occasional large values that may have been associated with monazite inclusions beneath the fluorapatite grain surface and thus not detected in the BSE images.

All of the monazite inclusions and rim grains analyzed were at least 5 μm in diameter and only analyses that give a reasonable monazite stochiometry are reported in Table 7. For a selection of seven samples, the proportions of monazite inclusions and rim grains relative to the host fluorapatite were estimated by determining the areas occupied by light monazite grains and dark fluorapatite in the BSE images (Table 10). The areas were determined by counting squares on a grid overlain on an enlargement of the BSE image. A total of 15 fluorapatite grains per sample were counted.

WHOLE-ROCK COMPOSITIONS

In Fig. 2 selected major-element analyses of intermediate to felsic orthognesisses from Hansen *et al.* (1995) are plotted against distance from the north end of the Krishnagiri–Salem traverse. No systematic trends are evident in Fe/(Fe + Mg) (Fig. 2a). Although there is a great deal of scatter, there is a tendency for TiO_2 (Fig. 2b) and MnO (Fig. 2c) to be lower and SiO_2 (Fig. 2d) to be higher in the NAF than in either the SGF or CGF. There is no systematic trend in any of these elements south of the orthopyroxene isograd. There is a tendency for K_2O (Fig. 2e) to be somewhat higher at the northern end of the traverse than at the southern end. However, in the middle of the traverse (CGF and northern SGF) K_2O is extremely variable with no visible trend. On an O'Connor (1965) normative feldspar plot most of the orthogneiss analyses fall in the granodiorite field, with most of the analyses from the southern SGF clustering near the boundary with tonalite and the analyses from the NAF trending towards the boundary with quartz monzonite (Hansen *et al.*, 1995, fig. 8).

The changes in mineral assemblages and abundances are roughly paralleled by changes in the abundances of some LILE (Rameshwar Rao *et al.*, 1991*a*; Hansen *et al.*, 1995; this study) (Table 2; Fig. 3). Most intermediate and felsic gneisses in the NAF and northern CGF have moderate to high Rb (30–150 ppm), Cs (0·05–0·25 ppm), Th (4–27 ppm) and U (0·2–2·1 ppm) concentrations, and K/Rb ratios below 500 (Rameshwar Rao *et al.*, 1991*a*; Hansen *et al.*, 1995, 2002). Low concentrations of Rb (<30 ppm), Cs (<0·005 ppm), U (<0·2 ppm) and Th (<2 ppm), and high K/Rb ratios (>500 ppm) become common in the southern orthopyroxene-rich portion of the area (i.e. SGF and southern CGF; Fig. 3a–d). At the southern edge of the SGF a few quartzo-feldspathic gneisses anomalously rich in biotite have higher contents of these elements more characteristic of rocks from the NAF. Hansen *et al.* (2002) found that samples containing very low whole-rock concentrations of Rb and high K/Rb ratios are characterized by both relatively low abundances of biotite and low concentrations of Rb in biotite.

Total REE concentrations (Fig. 3e) show greater variability, with somewhat higher average values in the NAF and CGF. However, these regional trends are fairly weak. The average chondrite-normalized REE patterns for the three metamorphic zones are shown in Fig. 4. All zones show enrichment in light REE (LREE). The patterns from the NAF and CGF are parallel. In comparison, the pattern from the SGF is somewhat less LREE enriched, crossing the other two at a low angle.

Table 2: Whole-rock trace-element analyses (ppm)

	Sample	Zone	*D* (km)	Rb	Sr	Zr	Nb	Cs	Ba	Hf	Ta	Pb	Th	U	Y	La	Ce	Pr	Nd	Sm	Eu	Gd	Tb	Dy	Ho	Er	Tm	Yb	Lu	∑REE
1	95 J3 I1	NAF	0·00	54·0		143				3·30		17·0	3·95	1·22		30·7	91·1	6·13	26·8	4·20	1·00	3·59	0·39	1·91	0·33	1·05	0·15	0·89	0·13	168
2	95 J3 H5	NAF	3·53	63·0		93				2·20		26·0	5·46	1·54		20·8	42·1	3·80	15·9	2·52	0·65	2·08	0·24	1·14	0·21	0·64	0·09	0·62	0·09	91
3	95 J3 H2	NAF	4·45	48·0		138				1·70		10·0	3·70	0·80		22·0	40·0	4·08	15·0	2·50	1·31	1·70	0·20	1·00	0·20	0·50	0·06	0·40	0·07	89
4	93 F11 R1*	NAF	4·82	89·8	377	103	2·90	0·25	722	2·91	0·10	18·7	9·50	0·57	1·96	18·9	32·1	3·13	9·84	1·21	0·86	0·62	0·07	0·38	0·07	0·22	0·03	0·21	0·03	68
5	93 F2 J1*	NAF	9·83	96·1	508	588	32·6	0·24	1122	12·4	1·92	19·0	11·0	2·04	37·7	102	235	26·8	95·3	15·3	3·03	10·8	1·39	7·57	1·37	3·69	0·52	3·25	0·48	507
6	93 F2 J2*	NAF	9·83	145	447	193	2·43	0·19	2170	4·90	0·18	23·4	21·4	0·48	2·87	115	191	15·5	40·1	3·15	1·13	1·30	0·13	0·59	0·10	0·27	0·04	0·28	0·05	369
	93 F2 J15	NAF	10·94	75·0		245				6·10		29·0	5·12	0·60		49·2	108	14·0	64·6	12·1	2·10	10·1	1·36	6·93	1·25	3·69	0·60	3·48	0·49	278
7	93 F2 K2	NAF	12·99	107		129				3·40		39·0	20·2	1·02		57·9	96·0	8·53	28·7	3·04	0·77	2·97	0·17	0·74	0·13	0·38	0·04	0·29	0·05	200
8	93 F2 L1	NAF	14·30	62·0		103				3·00		14·0	0·70	0·10		13·0	20·0	1·72	5·50	0·70	0·77	0·40	0·10	0·20	0·10	0·10	0·05	0·10	0·03	43
9	93 F2 L2*	NAF	14·30	50·3	483	166	7·80	0·12	346	3·78	0·35	11·4	3·35	0·49	8·36	30·2	61·6	6·56	22·4	3·42	1·05	2·38	0·31	1·64	0·30	0·82	0·12	0·74	0·11	132
10	93 F2 L4*	NAF	17·44	33·7	493	93·5	2·76	0·06	330	2·33	0·09	9·97	1·30	0·16	3·89	16·4	28·0	2·88	9·96	1·60	0·75	1·18	0·14	0·76	0·14	0·38	0·05	0·33	0·05	63
11	93 J30 A1	NAF	18·74	8·10		57				1·60		12·0	0·84	0·22		14·7	32·9	3·56	15·7	3·29	1·18	3·02	0·45	2·44	0·49	1·43	0·21	1·37	0·20	81
12	93 F2 M2*	NAF	22·08	73·6	479	133	2·39	0·10	1226	3·13	0·06	17·5	5·02	0·32	5·53	43·3	72·1	6·99	22·9	3·05	1·48	1·98	0·23	1·16	0·20	0·54	0·07	0·43	0·07	155
13	93 F2 M3	NAF	22·08	88·0									26·5	0·50		100	161		48·0	5·61	1·98		0·40					0·58	0·06	
14	93 J31 H2	CGF	23·19	39·0									6·30			36·8	68·0		26·0	3·75	1·23		0·40					0·45	0·06	
15	93 F3 N11	CGF	25·42	51·0		153				3·80		12·0	5·50			22·0	47·0	5·73	23·0	4·60	1·03	3·30	0·50	2·30	0·40	1·10	0·15	0·90	0·11	112
16	93 J31 F5*	CGF	26·35	50·6	490	102	28·1	0·04	1706	2·34	0·84	19·5	2·86	0·10	48·9	136	294	34·8	131	21·9	4·09	16·1	2·05	10·7	1·89	4·71	0·60	3·42	0·47	662
17	93 J31 G3*	CGF	26·90	42·7	646	101	3·92	0·07	511	2·37	0·08	10·6	3·77	0·18	5·42	42·9	71·9	7·11	23·8	3·22	1·36	2·11	0·24	1·21	0·22	0·49	0·06	0·36	0·05	155
18	93 J31 C4*	CGF	27·64	46·1	584	155	6·04	0·09	587	3·71	0·20	12·0	5·94	0·67	11·0	45·3	83·3	8·95	32·1	5·03	1·45	3·58	0·44	2·30	0·42	1·09	0·13	0·85	0·13	185
19	93 J31 D1*	CGF	29·87	58·3	552	147	3·05	0·03	607	3·44	0·05	10·0	5·27	0·18	11·1	54·5	97·8	10·4	37·4	5·78	1·44	4·02	0·49	2·45	0·43	1·06	0·13	0·78	0·11	217
22	93 F4 T1	CGF	32·10	50·0									3·80	0·40		42·5	75·0		28·0	4·06	1·64		0·50					0·58	0·09	
23	93 F4 R7*	CGF	34·70	66·4	575	232	7·80	0·06	812	5·58	0·25	8·66	6·00	0·40	40·2	65·6	158	20·7	85·5	16·0	2·74	11·6	1·54	8·39	1·55	4·13	0·55	3·39	0·49	380
24	93 F4 R5*	CGF	35·99	62·4	737	146	3·81	0·05	1414	3·33	0·09	10·5	8·08	0·19	15·9	66·1	126	14·0	51·2	7·79	2·00	5·33	0·65	3·36	0·60	1·57	0·20	1·21	0·18	280
25	93 F4 Q6*	CGF	38·96	24·0	1258	79·2	2·19	<0·005	1143	1·95	0·08	13·4	0·35	0·08	6·67	40·4	73·7	8·01	29·6	4·37	1·49	2·66	0·30	1·36	0·23	0·63	0·08	0·48	0·06	163
26	95 J1 W3	CGF	40·07	58·0		218				5·10		18·0	3·28	0·17		74·9	135	15·6	66·5	10·9	2·10	9·69	1·10	5·08	0·88	2·64	0·36	1·83	0·25	327
27	93 F4 Q1*	CGF	41·19	16·7	406	139	3·08	0·02	372	3·53	0·11	8·17	0·58	0·26	5·79	28·0	48·7	4·92	16·9	2·48	0·96	1·77	0·23	1·17	0·21	0·63	0·08	0·53	0·08	107
	95 J1 T1	CGF	42·30	24·0		232				5·70		11·0	1·30	0·10		58·0	124	14·6	59·0	11·0	2·81	7·60	0·90	4·60	0·80	2·20	0·28	1·60	0·23	288
28	93 F4 T10	CGF	45·10	16·0									0·40			38·7	72·0		32·0	5·28	1·43		0·60					1·04	0·14	
29	93 F4 P2	CGF	45·82	5·00									0·60			25·7	46·0		18·0	2·86	1·10		0·30					0·53	0·07	
30	95 J1 V3	CGF	46·01	8·70		144				3·10		16·0	0·57	0·15		29·6	53·2	4·93	19·0	2·52	0·95	2·37	0·20	0·81	0·14	0·35	0·04	0·22	0·04	114
	95 J1 P1	CGF	47·86	1·90		68				1·50		12·0	0·12	0·08		20·2	34·3	3·18	12·2	1·66	0·83	1·52	0·13	0·57	0·10	0·26	0·03	0·21	0·04	75
32	95 J1 S3	CGF	49·17	12·0		187				4·60		11·0	0·51	0·12		28·9	53·6	5·39	21·9	3·18	0·99	2·80	0·27	1·23	0·22	0·55	0·08	0·45	0·08	120
	93 F1 I11	CGF	53·43	2·00		171				3·70		10·0	0·11	0·07		38·4	75·7	8·26	36·0	5·78	1·65	5·06	0·58	2·75	0·50	1·46	0·18	1·08	0·15	178

(continued)

Table 2: Continued

	Sample	Zone	*D* (km)	Rb	Sr	Zr	Nb	Cs	Ba	Hf	Ta	Pb	Th	U	Y	La	Ce	Pr	Nd	Sm	Eu	Gd	Tb	Dy	Ho	Er	Tm	Yb	Lu	∑REE
33	93 F3 O3	SGF	54·36	5·00												23·9	52·0		24·0	5·08	1·38		0·50					1·13	0·19	
34	94 D31 M2*	SGF	63·82	1·77	865	76·6	6·20	<0·005	789	1·97	0·14	5·77	0·04	0·02	21·7	43·0	94·2	12·5	51·8	9·43	2·41	7·10	0·88	4·62	0·85	2·15	0·28	1·67	0·24	231
35	93 F11 P2*	SGF	67·16	4·62	639	85·0	3·05	<0·005	413	1·91	0·08	8·34	0·04	0·05	1·47	16·3	24·9	2·35	7·51	0·89	0·99	0·54	0·06	0·30	0·05	0·15	0·02	0·15	0·03	54
36	93 F9 I1*	SGF	69·02	5·76	283	82·9	5·05	<0·005	350	2·17	0·24	12·0	2·10	0·21	21·8	25·0	44·1	4·61	16·9	3·14	1·26	3·42	0·59	3·82	0·80	2·39	0·34	2·25	0·33	109
37	93 F9 H2	SGF	73·10	12·0		219				5·70		12·0	0·40			23·0	49·0	6·00	26·0	5·70	1·55	4·80	0·70	3·40	0·60	1·70	0·24	1·40	0·20	124
38	93 F6 W1*	SGF	77·73	27·2	822	56·2	1·95	0·02	836	1·33	0·08	15·0	0·38	0·33	3·83	22·2	36·7	3·71	13·2	1·86	1·12	1·22	0·14	0·72	0·14	0·35	0·05	0·35	0·05	82
39	93 F9 F8	SGF	78·11	9·00									0·60			29·2	49·0		19·0	2·55	1·36		0·30					0·56	0·10	
40	93 F6 W10*	SGF	80·33	11·4	735	65·8	3·47	<0·005	555	1·83	0·11	9·06	0·25	0·08	13·8	28·1	63·7	8·51	36·8	6·98	1·78	5·07	0·60	3·04	0·53	1·36	0·17	1·07	0·15	158
42	93 F6 W14	SGF	84·42	9·00		25·0				0·60		16·0	0·17	0·07		12·0	22·8	2·23	9·46	1·59	0·78	1·44	0·16	0·80	0·15	0·41	0·05	0·33	0·05	52
43	YD 42*	SGF	85·71	6·37	637	68·3	5·00	<0·005	639	1·64	0·11	6·95	0·07	0·09	11·1	21·6	43·5	5·44	22·8	4·44	1·47	3·44	0·43	2·33	0·41	1·13	0·15	0·90	0·13	108
	93 F6 X5	SGF	86·46	21·0		340				8·40		13·0	0·55	0·42		34·7	66·8	6·72	29·7	6·35	1·71	6·47	1·05	6·04	1·21	3·44	0·54	3·08	0·45	168
	93 F6 Y11	SGF	89·00	5·20		281				6·50		15·0	1·29	0·40		30·1	50·2	4·65	18·9	3·74	1·29	4·67	0·92	6·14	1·38	4·22	0·69	4·29	0·63	132
	93 F6 X12	SGF	89·24	7·00		66·0				3·20		11·0	0·30			36·0	66·0	6·82	25·0	3·80	1·32	2·30	0·30	1·30	0·20	0·60	0·06	0·40	0·06	144
44	93 F6 X13*	SGF	89·24	11·0	616	81·5	3·68	<0·005	647	1·89	0·09	7·75	0·17	0·10	3·84	18·1	29·9	3·10	11·0	1·60	1·10	1·17	0·14	0·71	0·15	0·40	0·05	0·39	0·06	68
45	93 F9 F5*	SGF	90·17	52·1	640	106	2·14	<0·005	1639	2·51	0·05	15·0	12·3	0·16	11·0	89·3	144	13·8	44·7	5·75	1·41	3·67	0·46	2·39	0·42	1·15	0·13	0·83	0·13	308
46	93 F8 A1	SGF	91·84	50·0		168				4·30		21·0	1·50	0·20		41·0	83·0	9·00	35·0	6·50	1·65	4·90	0·70	3·50	0·70	1·90	0·27	1·60	0·24	190
47	93 F9 F1*	SGF	92·02	8·56	688	90·6	3·68	0·01	463	2·19	0·12	8·04	0·46	0·13	6·14	28·1	51·6	5·63	21·1	3·32	1·37	2·40	0·26	1·33	0·23	0·61	0·07	0·48	0·07	117
48	93 F7 Z32*	SGF	92·57	4·47	984	90·8	4·67	<0·005	646	2·00	0·13	7·36	0·54	0·09	12·3	40·4	80·2	9·41	37·1	6·34	1·83	4·36	0·53	2·62	0·46	1·15	0·15	0·90	0·13	186
	93 F9 E1	SGF	94·20	37·0		198				4·90		18·0	10·9	0·30		49·3	84·8	7·35	27·8	3·79	1·27	4·17	0·67	4·85	1·17	3·89	0·73	4·90	0·76	195
49	93 F9 E3*	SGF	94·20	33·7	352	110	5·46	0·03	371	2·79	0·28	8·96	3·61	0·28	14·3	29·8	56·6	6·25	22·5	3·77	1·15	3·10	0·43	2·62	0·56	1·65	0·24	1·61	0·24	131
50	93 F8 D1*	SGF	94·99	8·50	367	79·2	4·40	<0·005	342	1·88	0·13	7·17	0·18	0·12	17·2	16·8	29·0	3·07	11·5	2·22	1·32	2·61	0·45	2·94	0·63	1·96	0·29	1·99	0·30	75

*Rock samples analysed according to the method described by Dulski (2001).
Blank indicates element not analysed for.

Table 3: Analytical conditions

Mineral	Accelerating voltage (kV)	Spot size (μm)	Beam current (nA)	Elements	Counting time (s)	Standards
Amphibole + biotite	15	5	20	F, Cl	30	NS
				Ti, Mn, Ba, Na	20	
				Si, Al, Fe, Mg, Ca, K	10	
Fluorapatite	20	15	10	Ce, La, Nd, Sm, Gd, Dy, Yb, Y	50	NS, SREE
				Fe, Si, Na, Sr, Al, Mn, S, Ba	50	
				P, Ca, F, Cl	30	
Monazite	20	1	40	Pb	300	NS, SREE
				U	200	
				Th	100	
				Ce, La, Pr, Nd, Sm, Tb, Dy, Ho	50	
				Eu, Yb, Lu, Y	50	
				Al, Si, P, Ca	30	
				Fe	20	
Allanite	20	2	40	Th, U	100	NS, SREE
				La, Ce, Pr, Nd, Sm, Gd, Dy, Y	50	
				Fe, Mg, Al, Si, P, Ti, Ca, Mn, F	30	
Titanite	15	1	40	Nb, Th, U	100	NS, SREE
				Y, La, Ce, Nd, Sm, Mg, Na	60	
				Al, Zr	40	
				P, Mn, Fe, F	30	
				Ca, Ti, Si	20	

NS, natural and synthetic silicate and oxide minerals (Jarosewich *et al.*, 1980); SREE, Smithsonian REE phosphate standard set (Jarosewich & Boatner, 1991).

MINERAL TEXTURES AND COMPOSITION

K-feldspar

Discrete grains of K-feldspar occur only in the more felsic orthogneisses, but patches and blebs of K-feldspar along mineral grain boundaries are found in most samples along the traverse (Fig. 5; Table 1). They were first reported in rocks from the southern portion of this area by Hansen *et al.* (1995) and studied in more detail by Harlov *et al.* (1998), who described them as K-feldspar micro-veins. However, these often lack the crosscutting relationships and obvious interconnectivity associated with veins and so in this paper the alternative term K-feldspar grain boundary blebs is used. Most of the K-feldspar blebs (80–90%) occur along quartz–plagioclase grain boundaries (Fig. 5). They can also occur along grain boundaries between orthopyroxene and plagioclase, garnet and plagioclase, perthite and plagioclase, and plagioclase and plagioclase, although invariably quartz is nearby. The K-feldspar grain boundary blebs range from relatively thin nearly continuous networks along quartz–plagioclase grain boundaries (Fig. 5a) to discontinuous patches (Fig. 5b and c). These K-feldspar textures are similar to those in the Ivrea–Verbano zone, as described in more detail by Franz & Harlov (1998).

Biotite

Biotite in the NAF tends to occur as large grains not noticeably associated with any other mineral. The abundance of biotite decreases southward in the CGF (Hansen *et al.*, 2002). In samples from the SGF, biotite tends to occur as relatively small grains along or near orthopyroxene grain boundaries (see Hansen *et al.*, 2002; fig. 3b).

Various element concentrations in biotite are plotted against distance from the northern edge of the traverse in Fig. 6 (see Table 4). Titanium concentrations (Fig. 6a) increase southwards to the orthopyroxene isograd, where they level off for the rest of the traverse. Both Fe (Fig. 6b) and Mn (Fig. 6c) concentrations decrease steadily throughout the NAF and the CGF and then remain approximately constant throughout the SGF. Although not plotted, Mg shows the opposite trend.

Table 4: Mean biotite compositions (wt %)

	Sample	Zone	*D* (km)	No pts	SiO_2	TiO_2	Al_2O_3	FeO	MnO	MgO	CaO	BaO	K_2O	Na_2O	F	Cl	H_2O†	Sum	O = (F + Cl)	Total	$\log(f_{H_2O}/f_{HF})$*	$\log(f_{H_2O}/f_{HCl})^*$	$\log(f_{HF}/f_{HCl})^*$
1	95 J3 I1	NAF	0	20	38·0(2)	1·67(11)	15·8(1)	18·6(4)	0·34(2)	12·4(3)	0·01(1)	0·12(7)	8·81(13)	0·04(1)	0·20(3)	0·01(1)	3·90	100·0	0·09	99·9	5·24	4·68	−0·57
2	95 J3 H5	NAF	3·53	16	37·8(4)	1·84(10)	16·4(2)	18·9(3)	0·33(3)	11·6(4)	0·01(1)	0·07(7)	8·68(10)	0·06(1)	0·13(3)	0·02(1)	3·92	99·8	0·05	99·7	5·42	4·57	−0·85
3	95 J3 H2	NAF	4·45	20	38·1(3)	1·86(15)	16·2(3)	18·3(7)	0·33(3)	12·3(5)	0·04(3)	0·14(7)	8·67(11)	0·08(2)	0·13(8)	0·04(1)	3·94	100·1	0·07	100·1	5·43	4·20	−1·23
4	93 F11 R1	NAF	4·82	21	37·4(4)	1·99(9)	16·4(2)	20·0(6)	0·31(7)	10·8(4)	0·02(3)	0·08(6)	8·59(26)	0·08(2)	0·30(5)	0·10(1)	3·80	99·9	0·15	99·8	5·01	3·81	−1·19
5	93 F2 J1	NAF	9·83	14	37·9(4)	2·38(8)	15·0(2)	19·3(2)	0·38(3)	12·1(2)	0·01(1)	0·15(7)	8·72(9)	0·07(2)	0·81(5)	0·09(1)	3·57	100·4	0·36	100·1	4·59	3·82	−0·77
6	93 F2 J2	NAF	9·83	16	38·2(3)	3·01(17)	15·6(4)	19·0(4)	0·20(3)	11·5(4)	0·01(1)	0·17(8)	8·76(24)	0·05(2)	0·85(6)	0·08(1)	3·59	101·0	0·38	100·6	4·56	3·85	−0·72
7	93 F2 K2	NAF	12·99	6	38·2(2)	2·52(11)	15·6(2)	19·9(3)	0·25(3)	10·9(1)	0·01(1)	0·03(4)	8·83(5)	0·06(1)	1·19(6)	0·09(2)	3·41	100·9	0·52	100·4	4·36	3·82	−0·54
8	93 F2 L1	NAF	14·3	20	38·2(3)	2·94(7)	16·5(3)	17·9(3)	0·15(3)	12·0(1)	0·01(2)	0·16(5)	8·82(21)	0·04(2)	0·11(3)	0·13(1)	3·97	100·9	0·08	100·8	5·54	3·67	−1·87
9	93 F2 L2	NAF	14·3	20	37·6(3)	2·96(8)	16·5(3)	19·7(3)	0·19(2)	10·9(2)	0·01(1)	0·14(9)	8·96(12)	0·07(1)	0·16(2)	0·12(1)	3·91	101·2	0·10	101·1	5·29	3·73	−1·55
10	93 F2 L4	NAF	17·44	24	37·5(2)	4·04(8)	14·8(1)	17·5(3)	0·20(2)	13·0(2)	0·01(1)	0·19(7)	8·78(14)	0·07(1)	0·22(8)	0·13(2)	3·87	100·3	0·12	100·2	5·24	3·65	−1·59
11	93 J30 A1	NAF	18·74	20	37·3(4)	4·86(19)	14·9(3)	17·3(5)	0·20(2)	12·8(2)	0·04(3)	0·40(11)	8·60(15)	0·07(3)	0·07(4)	0·05(1)	3·98	100·6	0·04	100·5	5·75	4·06	−1·69
12	93 F2 M2	NAF	22·08	18	37·6(5)	4·04(14)	15·3(4)	16·9(6)	0·14(3)	12·9(5)	0·02(2)	0·14(6)	8·69(19)	0·07(2)	0·21(4)	0·08(1)	3·91	100·1	0·11	100·0	5·28	3·88	−1·40
13	93 F2 M3	NAF	22·08	21	38·4(2)	4·09(13)	15·5(3)	16·4(4)	0·13(5)	13·3(3)	0·01(1)	0·20(8)	8·71(36)	0·07(3)	0·25(5)	0·11(1)	3·93	101·0	0·12	100·9	5·22	3·73	−1·49
14	93 J31 H2	CGF	23·19	14	37·3(2)	4·39(14)	15·4(2)	19·0(4)	0·09(3)	11·7(2)	0·01(1)	0·36(9)	8·68(9)	0·07(1)	0·16(4)	0·07(1)	3·93	101·2	0·09	101·1	5·17	3·91	−1·27
15	93 F3 N11	CGF	25·42	20	38·3(3)	4·70(15)	14·6(2)	15·1(4)	0·14(4)	14·9(3)	0·01(1)	0·29(7)	8·87(6)	0·03(1)	0·50(5)	0·09(1)	3·84	101·4	0·23	101·2	4·79	3·72	−1·08
16	93 J31 F5	CGF	26·35	24	38·8(3)	3·34(17)	14·0(2)	16·0(3)	0·21(4)	14·8(4)	0·02(1)	0·30(9)	8·83(8)	0·07(2)	2·13(9)	0·12(1)	3·02	101·6	0·93	100·7	4·04	3·51	−0·53
17	93 J31 G3	CGF	26·90	20	38·1(4)	4·59(27)	15·7(4)	15·7(6)	0·16(5)	13·5(7)	0·01(1)	0·25(10)	8·86(8)	0·04(2)	0·23(7)	0·09(1)	3·96	101·2	0·12	101·1	5·10	3·76	−1·34
18	93 J31 C4	CGF	27·64	20	37·9(4)	5·38(22)	14·6(2)	16·1(4)	0·15(4)	13·6(2)	0·01(1)	0·34(7)	8·85(9)	0·02(1)	0·27(3)	0·07(1)	3·92	101·2	0·13	101·1	5·02	3·85	−1·18
19	93 J31 D1	CGF	29·87	15	38·0(3)	5·26(26)	14·3(2)	16·1(3)	0·14(4)	13·9(2)	<0·01	0·23(7)	8·90(12)	0·03(2)	0·51(4)	0·12(1)	3·80	101·3	0·25	101·1	4·74	3·61	−1·13
20	93 J31 D3	CGF	29·87	10	38·1(4)	4·84(21)	14·9(3)	15·8(4)	0·16(3)	13·9(2)	0·06(5)	0·19(5)	8·58(27)	0·05(1)	0·54(4)	0·11(1)	3·79	100·9	0·26	100·7	4·72	3·64	−1·09
21	93 J31 E2	CGF	30·06	15	37·9(4)	4·98(37)	14·9(4)	15·8(4)	0·12(3)	13·7(4)	0·02(1)	0·31(7)	8·73(6)	0·04(2)	0·31(7)	0·09(2)	3·89	100·8	0·15	100·7	4·97	3·76	−1·21

(continued)

Table 4: Continued

	Sample	Zone	D (km)	No pts	SiO_2	TiO_2	Al_2O_3	FeO	MnO	MgO	CaO	BaO	K_2O	Na_2O	F	Cl	H_2O†	Sum	O = (F + Cl)	Total	$\log(f_{H_2O}/f_{HF})$*	$\log(f_{H_2O}/f_{HCl})$*	$\log(f_{HF}/f_{HCl})$*
22	93 F4 T1	CGF	32·10	20	38·2(2)	4·90(19)	14·8(2)	15·4(2)	0·19(3)	14·3(3)	0·01(1)	0·42(6)	8·77(9)	0·03(2)	0·31(7)	0·11(1)	3·92	101·4	0·15	101·2	4·99	3·67	−1·32
23	93 F4 R7	CGF	34·70	20	38·5(3)	4·16(20)	14·8(2)	14·8(3)	0·12(2)	15·1(2)	<0·01	0·49(9)	8·85(10)	0·04(2)	0·53(3)	0·11(1)	3·82	101·4	0·25	101·1	4·78	3·63	−1·15
24	93 F4 R5	CGF	35·99	20	38·1(3)	5·08(15)	14·8(4)	15·4(4)	0·11(4)	14·4(3)	<0·01	0·50(8)	8·76(8)	0·04(2)	0·42(5)	0·11(2)	3·87	101·6	0·20	101·4	4·85	3·66	−1·20
25	93 F4 Q6	CGF	38·96	15	38·7(4)	4·04(17)	14·5(4)	12·8(2)	0·11(3)	16·5(2)	0·02(2)	0·22(6)	8·80(10)	0·04(1)	1·42(5)	0·08(2)	3·41	100·7	0·62	100·1	4·36	3·72	−0·63
26	95 J1 W3	CGF	40·07	25	38·1(6)	5·23(23)	14·6(2)	14·2(3)	0·11(3)	15·1(3)	0·01(1)	0·37(6)	8·85(7)	0·04(2)	0·61(6)	0·14(1)	3·77	101·1	0·29	100·8	4·72	3·52	−1·20
27	93 F4 Q1	CGF	41·19	5	37·7(3)	5·31(6)	14·2(1)	15·0(2)	0·10(2)	14·5(1)	0·01(1)	0·48(9)	8·83(8)	0·03(1)	0·67(4)	0·08(1)	3·71	100·7	0·30	100·4	4·65	3·78	−0·87
28	93 F4 T10	CGF	45·10	20	39·1(3)	4·77(19)	14·8(3)	11·8(6)	0·04(3)	17·0(4)	0·03(3)	0·43(19)	8·87(10)	0·04(1)	1·25(10)	0·10(2)	3·54	101·8	0·55	101·3	4·45	3·59	−0·87
29	93 F4 P2	CGF	45·82	7	38·0(9)	4·40(39)	15·6(7)	11·3(20)	0·12(5)	17·8(13)	0·10(5)	0·47(14)	7·94(88)	0·04(1)	0·61(12)	0·13(2)	3·81	100·4	0·29	100·1	4·81	3·52	−1·29
30	95 J1 V3	CGF	46·01	10	37·9(6)	5·24(14)	15·3(3)	13·6(2)	0·02(2)	15·0(2)	0·03(2)	0·53(10)	8·59(6)	0·06(1)	0·18(5)	0·13(2)	3·98	100·6	0·11	100·5	5·28	3·57	−1·71
31	93 F1 I8	CGF	48·60	24	40·2(4)	3·80(33)	13·7(7)	9·07(80)	0·03(2)	20·1(7)	0·03(3)	0·09(9)	9·24(17)	0·03(1)	3·00(56)	0·14(2)	2·74	102·2	1·29	100·9	4·05	3·30	−0·75
32	95 J1 S3	CGF	49·17	4	38·2(2)	5·36(20)	15·6(2)	14·4(1)	0·03(1)	14·5(2)	<0·01	0·31(9)	8·86(4)	0·02(1)	0·21(2)	0·07(1)	4·01	101·5	0·11	101·4	5·20	3·83	−1·37
33	93 F3 O3	SGF	54·36	14	39·2(6)	4·32(35)	14·8(11)	11·5(9)	0·02(2)	17·5(7)	0·02(3)	0·40(21)	8·69(45)	0·04(2)	2·62(21)	0·14(2)	2·88	102·2	1·13	101·0	4·06	3·36	−0·70
34	94 D31 M2	SGF	63·82	10	38·4(3)	4·45(50)	14·0(4)	12·6(4)	0·04(3)	16·4(6)	2·73(23)	0·08(5)	9·00(35)	0·05(1)	2·33(22)	0·41(4)	2·93	103·3	1·07	102·3	3·92	2·87	−1·05
35	93 F11 P2	SGF	67·16	15	38·9(8)	4·16(30)	15·3(7)	11·0(10)	0·04(2)	17·5(11)	0·46(10)	0·08(6)	9·25(20)	0·03(1)	1·47(14)	0·08(2)	3·46	101·8	0·64	101·2	4·40	3·69	−0·70
36	93 F9 I1	SGF	69·02	21	39·2(3)	5·27(14)	14·9(2)	12·0(5)	0·02(2)	16·4(3)	<0·01	0·20(14)	9·05(9)	0·02(1)	0·86(5)	0·04(1)	3·75	101·7	0·37	101·4	4·47	3·97	−0·50
38	93 F6 W1	SGF	77·73	9	39·4(4)	3·82(89)	14·7(5)	10·0(6)	0·05(2)	18·3(3)	0·38(4)	0·32(2)	9·30(9)	0·05(1)	1·90(6)	0·05(1)	3·25	101·6	0·81	100·8	4·13	3·77	−0·36
39	93 F9 F8	SGF	78·11	21	38·5(3)	4·63(26)	14·5(4)	11·6(5)	0·02(2)	17·1(3)	0·30(5)	0·14(5)	9·25(15)	0·02(1)	1·51(10)	0·05(1)	3·40	101·1	0·64	100·5	4·20	3·88	−0·32
40	93 F6 W10	SGF	80·33	13	39·5(6)	4·45(22)	14·0(3)	10·9(9)	0·02(2)	18·1(7)	0·04(2)	0·27(14)	9·05(13)	0·03(1)	2·11(9)	0·03(1)	3·15	101·6	0·90	100·7	4·05	4·05	0·00
41	YD50	SGF	83·86	22	39·1(4)	5·40(13)	14·5(1)	11·8(5)	0·04(2)	16·8(5)	0·01(1)	0·12(9)	9·07(8)	0·03(1)	1·39(7)	0·08(2)	3·48	101·8	0·61	101·2	4·24	3·63	−0·61
43	YD42	SGF	85·71	11	39·0(4)	4·60(21)	15·1(3)	11·9(6)	0·02(2)	16·8(5)	0·01(2)	0·31(12)	8·87(11)	0·03(1)	1·35(9)	0·04(1)	3·51	101·6	0·58	101·0	4·26	3·98	−0·28
44	93 F6 X13	SGF	89·24	14	38·9(5)	4·10(29)	14·4(3)	11·2(5)	0·01(2)	17·8(4)	0·28(4)	0·15(4)	9·10(42)	0·04(1)	2·10(21)	0·04(1)	3·12	101·2	0·89	100·3	4·04	3·88	−0·16
45	93 F9 F5	SGF	90·17	32	38·6(3)	4·51(19)	14·9(2)	12·0(6)	0·02(2)	16·8(5)	0·03(2)	0·18(11)	8·98(17)	0·04(1)	1·29(11)	0·05(1)	3·50	100·8	0·55	100·3	4·27	3·85	−0·42
47	93 F9 F1	SGF	92·02	39	38·8(4)	4·89(16)	14·8(3)	12·6(2)	0·02(2)	16·5(3)	0·02(2)	0·29(7)	8·95(13)	0·04(1)	1·25(13)	0·03(1)	3·54	101·6	0·54	101·1	4·27	4·09	−0·18
49	93 F9 E3	SGF	94·20	22	39·0(3)	4·81(19)	14·3(4)	13·0(4)	0·02(2)	16·0(4)	0·01(1)	0·45(9)	9·00(8)	0·05(1)	1·54(7)	0·04(1)	3·38	101·5	0·67	100·9	4·15	3·91	−0·24
50	93 F8 D1	SGF	94·99	5	39·4(4)	4·35(33)	16·2(4)	12·7(3)	0·01(2)	15·0(5)	0·04(8)	0·19(9)	8·65(13)	0·13(17)	0·11(6)	0·09(1)	4·09	101·0	0·07	100·9	5·37	3·67	−1·70

*Calculated using the formulation of Munoz (1992).
†Calculated assuming the (F,Cl,OH) site is filled.

Table 5: Mean amphibole compositions (wt %)

	Sample	Zone	*D* (km)	No. pts	SiO_2	TiO_2	Al_2O_3	FeO	MgO	MnO	CaO	K_2O	Na_2O	F	Cl	H_2O^*	Sum	O = (F + Cl)	Total
1	95 J3 I1	NAF	0	20	45·1(3)	0·79(6)	9·06(20)	18·7(3)	10·5(2)	0·46(3)	11·7(1)	0·88(3)	1·36(8)	<0·01	0·01(1)	1·99	100·4	0·00	100·4
3	95 J3 H2	NAF	4·45	22	44·9(4)	1·16(27)	9·37(40)	18·5(4)	10·4(2)	0·47(3)	11·7(1)	1·00(4)	1·46(6)	<0·01	0·02(1)	2·00	100·9	0·00	100·9
5	93 F2 J1	NAF	9·83	6	43·9(2)	1·06(8)	9·69(12)	19·5(3)	9·39(21)	0·56(7)	11·5(1)	1·18(3)	1·58(6)	0·28(4)	0·09(1)	1·83	100·6	0·14	100·4
10	93 F2 L4	NAF	17·44	22	44·9(3)	1·26(9)	9·69(25)	16·3(4)	11·2(2)	0·34(4)	11·7(1)	1·10(3)	1·40(9)	0·02(3)	0·11(1)	1·97	100·1	0·03	100·1
11	93 J30 A1	NAF	18·74	21	45·0(4)	1·65(12)	9·76(18)	15·9(3)	12·0(2)	0·36(3)	11·8(1)	1·07(3)	1·33(9)	0·01(5)	0·04(1)	2·02	100·9	0·01	100·9
12	93 F2 M2	NAF	22·08	18	48·3(10)	0·64(8)	7·79(80)	14·3(6)	14·1(6)	0·60(4)	11·8(1)	0·72(9)	1·15(15)	0·09(3)	0·04(1)	2·02	101·6	0·05	101·5
14	93 J31 H2	CGF	23·19	6	44·6(6)	1·14(9)	10·7(3)	16·8(2)	11·3(3)	0·34(2)	11·8(4)	1·15(6)	1·11(7)	0·02(3)	0·05(1)	2·01	101·1	0·02	101·0
16	93 J31 F5	CGF	26·35	21	43·3(3)	1·40(14)	10·4(3)	17·2(4)	11·1(2)	0·46(4)	11·6(1)	1·49(5)	1·72(11)	0·85(4)	0·13(1)	1·56	101·1	0·39	100·7
25	93 F4 Q6	CGF	38·96	20	46·4(5)	1·74(17)	8·54(29)	13·6(4)	13·4(2)	0·31(2)	11·4(2)	1·02(3)	1·78(16)	0·50(6)	0·04(1)	1·79	100·5	0·22	100·3
27	93 F4 Q1	CGF	41·19	18	44·5(6)	2·09(12)	9·92(22)	14·1(3)	12·6(2)	0·24(3)	11·6(1)	1·22(4)	1·50(10)	0·22(5)	0·06(1)	1·90	99·8	0·11	99·7
28	93 F4 T10	CGF	45·10	17	44·3(3)	1·89(18)	10·5(2)	13·8(4)	12·7(2)	0·17(3)	11·6(2)	1·37(4)	1·41(17)	0·42(4)	0·10(1)	1·80	100·0	0·20	99·8
29	93 F4 P2	CGF	45·82	4	45·4(2)	1·99(2)	10·0(0)	13·3(0)	13·2(1)	0·13(2)	11·8(1)	1·18(3)	1·75(6)	0·24(3)	0·10(0)	1·92	101·1	0·12	101·0
31	93 F1 I8	CGF	48·60	26	44·4(5)	1·51(20)	11·2(6)	12·3(8)	13·5(5)	0·14(5)	11·8(2)	1·74(13)	1·74(13)	1·24(7)	0·19(2)	1·41	101·2	0·57	100·7
32	95 J1 S3	CGF	49·17	3	43·5(2)	1·75(14)	12·0(3)	14·1(2)	12·0(1)	0·10(4)	11·8(0)	1·48(3)	1·28(4)	0·03(3)	0·09(2)	2·00	100·2	0·03	100·2
33	93 F3 O3	SGF	54·36	27	43·5(5)	2·10(16)	11·6(5)	13·1(4)	12·4(2)	0·13(3)	11·6(1)	1·84(7)	1·65(7)	1·04(7)	0·16(1)	1·46	100·6	0·47	100·2
37	93 F9 H2	SGF	73·10	20	44·1(8)	1·67(15)	12·0(5)	13·2(6)	12·4(4)	0·11(3)	11·9(1)	1·82(7)	1·43(11)	0·89(6)	0·09(1)	1·60	101·3	0·40	100·9
39	93 F9 F8	SGF	78·11	5	43·8(5)	1·24(59)	12·4(3)	12·2(6)	13·0(5)	0·13(3)	12·1(2)	1·73(8)	1·33(13)	0·64(11)	0·06(1)	1·73	100·4	0·28	100·1
42	93 F6 W14	SGF	84·42	10	42·2(7)	1·54(19)	12·7(6)	15·3(4)	10·6(3)	0·13(2)	11·8(1)	2·03(14)	1·41(11)	0·66(5)	0·21(3)	1·63	100·2	0·33	99·9
44	98 F6 X13	SGF	89·24	7	43·8(6)	1·41(25)	12·8(6)	12·6(4)	12·7(3)	0·10(2)	11·8(4)	1·90(13)	1·39(6)	0·90(7)	0·06(1)	1·61	101·0	0·39	100·6
45	93 F9 F5	SGF	90·17	26	43·0(6)	1·78(29)	11·9(5)	13·3(5)	12·2(4)	0·14(3)	11·6(2)	1·60(11)	1·72(12)	0·49(5)	0·06(1)	1·76	99·6	0·22	99·3
47	93 F9 F1	SGF	92·02	41	44·1(3)	1·63(30)	12·3(7)	12·6(4)	12·7(3)	0·14(3)	11·7(1)	1·58(10)	1·68(12)	0·55(5)	0·03(1)	1·78	100·9	0·24	100·7
48	93 F7 Z32	SGF	92·57	15	43·3(3)	1·79(27)	12·0(3)	12·2(5)	12·8(3)	0·10(2)	12·1(1)	2·11(11)	1·46(12)	1·00(9)	0·18(3)	1·52	100·6	0·46	100·1

*Calculated assuming the (F,Cl,OH) site is filled.

Table 6: Mean fluorapatite compositions (wt %)

	Sample	Zone	*D* (km)	No. grains	P_2O_5	SiO_2	SO_2	La_2O_3	Ce_2O_3	Nd_2O_3	CaO	FeO*	MnO	SrO	Na_2O	F	Cl	H_2O†	Sum	O = (F + Cl)	Total	$(Y + LREE)_2O_3$
1	95 J3 I1	NAF	0	6	41·5(3)	0·11(5)	0·12(9)	<0·05	<0·05	<0·05	54·7(2)	0·01(1)	0·03(1)	0·06(2)	0·04(3)	3·28	0·01(1)	0·21	100·1	1·38	98·7	0·00
2	95 J3 H5	NAF	3·53	6	41·9(4)	0·13(9)	0·10(4)	<0·05	<0·05	<0·05	54·6(2)	0·01(2)	0·05(1)	0·06(1)	0·02(2)	3·28	0·02(1)	0·22	100·4	1·39	99·0	0·00
3	95 J3 H2	NAF	4·45	6	41·7(4)	0·17(8)	0·11(3)	<0·05	0·11(8)	<0·05	54·9(2)	0·01(1)	0·04(2)	0·05(3)	0·02(2)	3·37	0·02(1)	0·17	100·6	1·42	99·2	0·11
4	93 F11 R1	NAF	4·82	6	41·7(3)	0·22(26)	0·10(3)	0·09(12)	0·19(20)	<0·05	54·7(4)	0·03(4)	0·04(2)	0·04(3)	0·02(1)	3·45	0·04(1)	0·13	100·8	1·46	99·3	0·28
5	93 F2 J1	NAF	9·83	8	41·3(6)	0·31(10)	0·22(6)	0·14(10)	0·22(7)	<0·05	54·9(3)	0·04(4)	0·04(1)	0·06(3)	0·05(3)	3·66	0·03(1)	0·03	101·0	1·55	99·5	0·36
6	93 F2 J2	NAF	9·83	7	41·2(6)	0·23(12)	0·08(2)	<0·05	0·23(8)	0·11(9)	54·5(3)	0·04(4)	0·04(1)	0·06(2)	0·04(3)	3·68	0·03(1)	0·01	100·3	1·56	98·7	0·34
7	93 F2 K2	NAF	12·99	5	41·4(7)	0·28(25)	0·03(2)	<0·05	0·31(31)	0·11(10)	54·5(5)	0·06(7)	0·03(2)	0·03(2)	0·01(0)	3·87	0·02(1)	0·00	100·6	1·63	99·0	0·42
8	93 F2 L1	NAF	14·30	4	41·4(2)	0·24(11)	0·10(4)	<0·05	0·11(11)	0·16(16)	54·5(3)	0·03(3)	0·04(2)	0·04(1)	0·03(2)	3·30	0·19(6)	0·16	100·3	1·43	98·9	0·27
9	93 F2 L2	NAF	14·30	6	41·6(6)	0·21(12)	0·09(5)	<0·05	0·11(8)	0·11(11)	54·6(3)	0·02(2)	0·03(2)	0·06(2)	0·03(3)	3·49	0·08(2)	0·10	100·6	1·49	99·1	0·22
10	93 F2 L4	NAF	17·44	9	41·4(5)	0·15(7)	0·08(5)	<0·05	0·11(9)	0·09(9)	54·9(4)	0·04(3)	0·03(2)	0·05(2)	0·04(2)	3·11	0·23(6)	0·23	100·4	1·36	99·0	0·20
11	93 J30 A1	NAF	18·74	6	41·8(3)	0·22(20)	0·07(3)	<0·05	0·08(8)	<0·05	54·6(2)	0·03(3)	0·04(3)	0·05(2)	0·05(6)	3·28	0·17(5)	0·18	100·6	1·42	99·2	0·08
12	93 F2 M2	NAF	22·08	10	41·3(5)	0·26(10)	0·07(3)	<0·05	0·27(15)	0·24(11)	54·6(3)	0·06(3)	0·09(3)	0·06(2)	0·07(2)	3·17	0·16(4)	0·22	100·5	1·37	99·1	0·50
13	93 F2 M3	NAF	22·08	9	41·5(9)	0·19(5)	0·05(3)	<0·05	0·13(6)	0·14(8)	54·7(4)	0·03(2)	0·07(1)	0·07(2)	0·07(3)	3·13	0·24(8)	0·22	100·5	1·37	99·1	0·27
14	93 J31 H2	CGF	23·19	6	41·3(4)	0·26(7)	0·01(2)	<0·05	0·16(4)	0·19(9)	54·3(2)	0·08(2)	0·06(2)	0·04(1)	0·02(2)	3·20	0·12(3)	0·21	100·0	1·37	98·6	0·35
15	93 F3 N11	CGF	25·42	5	41·5(5)	0·28(15)	0·06(3)	0·08(7)	0·19(11)	0·17(12)	54·2(3)	0·09(6)	0·06(3)	0·04(3)	0·06(3)	3·20	0·23(3)	0·19	100·3	1·40	98·9	0·44
16	93 J31 F5	CGF	26·35	6	41·0(8)	0·54(26)	0·06(3)	0·36(24)	0·68(28)	0·27(13)	54·1(6)	0·20(6)	0·05(3)	0·02(3)	0·05(2)	3·78	0·04(2)	0·00	101·2	1·60	99·6	1·31
17	93 J31 G3	CGF	26·90	6	41·4(6)	0·35(9)	0·07(3)	<0·05	0·21(8)	0·20(11)	54·3(5)	0·09(5)	0·12(3)	0·05(2)	0·04(2)	2·99	0·24(2)	0·29	100·4	1·31	99·0	0·41
18	93 J31 C4	CGF	27·64	8	41·6(4)	0·31(8)	0·09(2)	<0·05	0·20(7)	0·20(7)	54·7(2)	0·24(16)	0·10(3)	0·04(2)	0·05(3)	3·27	0·18(3)	0·18	101·2	1·42	99·8	0·40
19	93 J31 D1	CGF	29·87	6	41·0(4)	0·44(5)	0·07(2)	0·10(7)	0·42(8)	0·31(8)	54·0(1)	0·08(6)	0·05(2)	0·05(3)	0·02(1)	3·17	0·29(5)	0·18	100·2	1·40	98·8	0·83
20	93 J31 D3	CGF	29·87	8	41·0(4)	0·40(7)	0·07(5)	<0·05	0·40(14)	0·28(10)	54·3(3)	0·19(8)	0·08(3)	0·03(2)	0·05(4)	3·25	0·23(4)	0·16	100·4	1·42	99·0	0·68
21	93 J31 E2	CGF	30·06	8	41·5(4)	0·26(10)	0·05(5)	<0·05	0·20(12)	0·13(5)	54·7(4)	0·21(9)	0·07(3)	0·06(4)	0·06(3)	3·07	0·19(4)	0·27	100·7	1·34	99·4	0·33
22	93 F4 T1	CGF	32·10	6	41·4(6)	0·33(15)	0·13(4)	<0·05	0·27(20)	0·21(18)	54·2(5)	0·08(1)	0·09(4)	0·04(3)	0·06(1)	3·24	0·33(5)	0·15	100·4	1·44	99·0	0·48
23	93 F4 R7	CGF	34·70	8	41·5(3)	0·43(10)	0·07(5)	<0·05	0·30(13)	0·34(9)	54·5(3)	0·17(14)	0·04(2)	0·06(3)	0·03(3)	3·27	0·26(4)	0·16	101·1	1·44	99·6	0·64
24	93 F4 R5	CGF	35·99	6	40·7(4)	0·48(12)	0·13(4)	0·11(5)	0·48(15)	0·31(10)	53·6(2)	0·06(5)	0·07(2)	0·04(2)	0·06(4)	2·97	0·30(9)	0·26	99·5	1·32	98·2	0·90
25	93 F4 Q6	CGF	38·96	6	41·3(8)	0·32(16)	0·15(3)	<0·05	0·31(19)	0·22(12)	54·3(4)	0·03(2)	0·03(2)	0·10(2)	0·05(2)	3·69	0·10(2)	0·00	100·6	1·58	99·0	0·53

(continued)

Table 6: Continued

	Sample	Zone	*D* (km)	No. grains	P_2O_5	SiO_2	SO_2	La_2O_3	Ce_2O_3	Nd_2O_3	CaO	FeO*	MnO	SrO	Na_2O	F	Cl	H_2O†	Sum	O = (F + Cl)	Total	$(Y + LREE)_2O_3$
26	95 J1 W3	CGF	40·07	6	41·5(3)	0·32(10)	0·11(5)	<0·05	0·24(10)	0·19(3)	53·8(8)	0·14(5)	0·09(2)	0·07(2)	0·04(2)	3·11	0·37(8)	0·20	100·2	1·39	98·8	0·43
27	93 F4 Q1	CGF	41·19	10	41·6(6)	0·28(13)	0·08(3)	<0·05	0·30(14)	0·22(10)	54·8(2)	0·17(6)	0·05(2)	0·04(3)	0·05(3)	3·34	0·16(2)	0·16	101·2	1·44	99·8	0·52
28	93 F4 T10	CGF	45·10	7	41·6(4)	0·29(27)	0·09(4)	<0·05	0·09(6)	0·12(8)	54·7(5)	0·38(44)	0·04(1)	0·05(2)	0·05(3)	3·40	0·21(7)	0·13	101·1	1·48	99·6	0·21
29	93 F4 P2	CGF	45·82	6	40·6(6)	0·36(9)	0·14(9)	<0·05	0·20(6)	0·25(6)	54·6(3)	0·10(4)	0·02(2)	0·03(1)	0·05(4)	3·23	0·33(2)	0·14	100·0	1·43	98·6	0·45
30	95 J1 V3	CGF	46·01	1	40·6	0·63	0·10	<0·05	0·42	0·26	53·8	0·13	<0·05	0·03	0·05	3·04	0·24	0·00	99·3	1·33	98·0	0·68
31	93 F1 I8	CGF	48·60	6	41·3(8)	0·49(27)	0·09(6)	<0·05	0·23(24)	0·21(10)	54·2(4)	0·09(3)	0·03(2)	0·04(2)	0·04(2)	3·59	0·20(4)	0·01	100·5	1·56	99·0	0·44
32	95 J1 S3	CGF	49·17	7	40·4(5)	0·26(11)	0·04(4)	0·09(6)	0·12(9)	0·17(9)	54·6(3)	0·11(5)	0·03(3)	0·04(2)	0·04(3)	3·18	0·23(7)	0·18	99·5	1·39	98·1	0·38
33	93 F3 O3	SGF	54·36	8	41·0(5)	0·29(4)	0·03(2)	<0·05	0·25(11)	0·17(10)	54·0(6)	0·14(10)	0·03(1)	0·04(3)	0·02(2)	3·88	0·13(2)	0·00	100·0	1·66	98·3	0·42
34	94 D31 M2	SGF	63·82	7	41·4(10)	0·40(24)	0·04(5)	<0·05	<0·05	<0·05	54·0(5)	0·26(17)	0·04(2)	0·08(3)	0·04(3)	3·38	0·44(12)	0·05	100·1	1·52	98·6	0·00
35	93 F11 P2	SGF	67·16	6	41·9(4)	0·52(51)	0·09(8)	<0·05	0·11(11)	0·15(9)	54·5(6)	0·06(4)	0·02(2)	0·05(3)	0·06(3)	3·56	0·13(2)	0·06	101·2	1·53	99·7	0·26
36	93 F9 I1	SGF	69·02	8	41·9(2)	0·16(17)	0·01(2)	<0·05	<0·05	0·08(10)	55·0(3)	0·15(13)	0·02(2)	0·04(2)	0·04(5)	3·49	0·08(5)	0·11	101·1	1·49	99·6	0·08
37	93 F9 H2	SGF	73·10	10	41·6(4)	0·27(25)	0·03(5)	<0·05	<0·05	<0·05	54·7(5)	0·11(15)	0·02(2)	0·05(3)	0·03(3)	3·78	0·06(1)	0·00	100·6	1·61	99·0	0·00
38	93 F6 W1	SGF	77·73	9	41·8(5)	0·25(5)	0·17(6)	<0·05	0·15(7)	0·12(9)	54·9(2)	0·09(11)	0·02(1)	0·07(1)	0·05(1)	3·61	0·08(3)	0·05	101·4	1·54	99·8	0·27
39	93 F9 F8	SGF	78·11	6	41·4(3)	0·51(26)	0·13(10)	<0·05	0·50(62)	0·25(21)	54·5(11)	0·13(7)	0·02(2)	0·04(2)	0·04(3)	3·73	0·10(1)	0·00	101·3	1·59	99·7	0·75
40	93 F6 W10	SGF	80·33	10	41·6(3)	0·33(6)	0·15(7)	<0·05	0·21(8)	0·13(8)	55·1(2)	0·14(9)	0·01(1)	0·04(2)	0·05(3)	3·66	0·04(1)	0·03	101·4	1·55	99·8	0·34
42	93 F6 W14	SGF	84·42	6	41·3(3)	0·24(3)	0·01(1)	<0·05	0·22(7)	0·16(7)	54·6(2)	0·06(5)	0·02(2)	0·06(3)	0·01(1)	3·71	0·13(5)	0·00	100·5	1·59	98·9	0·38
43	YD42	SGF	85·71	6	41·5(4)	0·24(16)	0·05(6)	<0·05	<0·05	<0·05	54·5(6)	0·11(7)	0·02(4)	0·06(2)	0·04(2)	3·37	0·06(1)	0·16	100·1	1·43	98·7	0·00
44	93 F6 X13	SGF	89·24	7	41·2(7)	0·42(7)	0·12(7)	<0·05	0·20(13)	0·17(10)	54·3(6)	0·17(13)	0·01(1)	0·04(4)	0·05(3)	3·63	0·06(6)	0·03	100·5	1·54	98·9	0·37
45	93 F9 F5	SGF	90·17	7	41·4(6)	0·35(16)	0·06(5)	<0·05	0·12(13)	0·12(13)	54·3(3)	0·10(5)	0·02(2)	0·06(3)	0·04(2)	3·83	0·08(2)	0·00	100·4	1·63	98·8	0·24
46	93 F8 A1	SGF	91·84	11	41·5(7)	0·49(46)	0·04(6)	<0·05	<0·05	0·11(10)	54·5(5)	0·08(7)	0·02(2)	0·04(3)	0·08(14)	2·89	0·23(13)	0·35	100·3	1·27	99·1	0·11
47	93 F9 F1	SGF	92·02	9	42·2(5)	0·15(14)	0·06(6)	<0·05	<0·05	0·12(7)	55·2(3)	0·27(25)	0·03(3)	0·07(2)	0·05(2)	3·72	0·04(1)	0·02	101·9	1·58	100·3	0·12
48	93 F7 Z32	SGF	92·57	6	41·5(4)	0·33(18)	0·14(7)	<0·05	0·14(10)	0·17(11)	54·7(4)	0·06(6)	0·03(1)	0·06(3)	0·02(2)	3·62	0·15(3)	0·03	101·0	1·56	99·4	0·32
49	93 F9 E3	SGF	94·20	1	41·5	0·11	0·00	<0·05	<0·05	<0·05	55·8	0·06	0·01	0·05	0·02	4·55	0·03	0·00	102·1	1·92	100·2	0·00
50	93 F8 D1	SGF	94·99	6	41·8(6)	0·12(11)	0·01(2)	<0·05	<0·05	<0·05	54·8(6)	0·07(3)	0·02(2)	0·05(2)	0·05(1)	3·09	0·09(3)	0·28	100·3	1·32	99·0	0·00

*Total Fe as FeO.
†Calculated to be zero assuming the (F,Cl,OH) site is filled.

Table 7: Representative analyses of monazite inclusions and rim grains associated with fluorapatite

	Sample	Zone	*D* (km)	Type	P_2O_5	SiO_2	ThO_2	Y_2O_3	La_2O_3	Ce_2O_3	Pr_2O_3	Nd_2O_3	Sm_2O_3	Gd_2O_3	Tb_2O_3	Dy_2O_3	Ho_2O_3	Er_2O_3	Yb_2O_3	Lu_2O_3	CaO	PbO	FeO*	Total
10	93 F2 L4	NAF	17·44	Rim	29·6	0·63	<0·02	0·15	17·8	36·3	3·13	9·46	0·59	0·23	<0·05	<0·05	<0·05	0·05	<0·05	<0·05	0·77	<0·01	0·01	98·7
11	93 J30 A1	NAF	18·74	Rim	28·4	0·56	<0·02	0·04	20·8	35·8	2·68	7·52	0·39	0·11	<0·05	<0·05	<0·05	0·09	<0·05	<0·05	1·19	<0·01	0·54	98·2
12	93 F2 M2	NAF	22·08	Rim	29·2	0·38	<0·02	0·09	21·7	35·7	2·54	7·33	0·53	0·21	<0·05	<0·05	<0·05	<0·05	<0·05	<0·05	1·02	<0·01	0·34	99·1
13	93 F2 M3	NAF	22·08	Rim	28·4	0·69	<0·02	0·27	19·0	35·1	3·08	9·87	0·99	0·38	<0·05	<0·05	<0·05	<0·05	<0·05	<0·05	0·69	<0·01	0·06	98·5
14	93 J31 H2	CGF	23·19	Incl	30·0	0·69	<0·02	0·28	15·9	33·5	3·22	12·6	1·30	0·59	<0·05	<0·05	<0·05	<0·05	<0·05	<0·05	0·62	0·02	0·05	98·8
15	93 F3 N11	CGF	25·42	Rim	29·2	0·30	<0·02	0·36	15·9	35·2	3·53	11·8	1·13	0·54	<0·05	0·05	0·05	0·10	<0·05	<0·05	0·41	<0·01	0·63	99·2
				Incl	31·0	0·33	<0·02	0·50	13·8	35·0	3·68	13·2	1·45	0·63	<0·05	<0·05	<0·05	0·06	<0·05	<0·05	1·03	<0·01	0·09	100·7
16	93 J31 F5	CGF	26·35	Rim	29·2	0·40	<0·02	0·05	29·0	31·7	1·82	4·97	0·21	0·14	<0·05	0·05	<0·05	<0·05	<0·05	<0·05	0·79	<0·01	0·16	98·5
17	93 J31 G3	CGF	26·90	Rim	31·3	0·35	<0·02	0·40	16·8	33·8	3·17	10·9	1·19	0·61	0·06	<0·05	<0·05	0·12	<0·05	<0·05	1·18	<0·01	0·18	100·1
				Incl	31·2	0·36	<0·02	0·50	15·7	34·2	3·40	12·2	1·40	0·74	<0·05	0·14	<0·05	0·10	<0·05	<0·05	2·21	<0·01	0·02	102·1
18	93 J31 C4	CGF	27·64	Rim	29·8	0·33	<0·02	0·71	15·5	35·1	3·49	12·4	1·49	0·84	<0·05	<0·05	<0·05	0·05	<0·05	<0·05	0·60	<0·01	0·10	100·3
19	93 J31 D1	CGF	29·87	Rim	29·0	0·38	<0·02	0·30	19·2	36·0	3·07	9·75	0·90	0·43	<0·05	<0·05	<0·05	<0·05	<0·05	<0·05	0·27	<0·01	0·10	99·3
20	93 J31 D3	CGF	29·87	Rim	30·0	0·32	<0·02	0·19	18·3	35·1	3·10	10·3	0·84	0·34	<0·05	<0·05	<0·05	<0·05	<0·05	<0·05	0·52	<0·01	0·17	99·2
				Incl	29·7	0·40	<0·02	0·39	15·5	34·8	3·37	12·4	1·35	0·53	<0·05	<0·05	<0·05	<0·05	<0·05	<0·05	0·95	<0·01	0·05	99·5
21	93 J31 E2	CGF	30·06	Rim	29·0	0·38	<0·02	0·47	15·5	35·7	3·51	12·6	1·35	0·67	<0·05	<0·05	0·05	<0·05	<0·05	<0·05	0·29	<0·01	0·06	99·5
22	93 F4 T1	CGF	32·10	Incl	28·3	0·51	<0·02	0·31	18·6	35·2	3·02	10·1	1·07	0·41	<0·05	0·05	<0·05	<0·05	<0·05	<0·05	1·40	<0·01	0·01	99·0
23	93 F4 R7	CGF	34·70	Rim	27·5	0·46	<0·02	0·27	17·2	35·0	3·29	11·1	1·05	0·41	<0·05	<0·05	<0·05	0·07	<0·05	<0·05	0·94	<0·01	0·03	97·3
24	93 F4 R5	CGF	35·99	Incl	29·1	0·38	<0·02	0·33	15·1	35·3	3·54	12·7	1·13	0·59	<0·05	<0·05	<0·05	0·05	<0·05	<0·05	1·15	<0·01	0·04	99·5
25	93 F4 Q6	CGF	38·96	Rim	29·0	0·59	<0·02	0·20	18·5	35·6	3·18	9·77	0·84	0·29	<0·05	<0·05	<0·05	<0·05	<0·05	<0·05	0·69	<0·01	0·08	98·8
26	95 J1 W3	CGF	40·07	Rim	28·3	0·36	<0·02	0·22	17·9	36·4	3·33	10·7	0·83	0·37	<0·05	<0·05	0·08	<0·05	<0·05	<0·05	0·71	<0·01	0·13	99·3
27	93 F4 Q1	CGF	41·19	Rim	29·8	0·36	<0·02	0·26	18·4	36·6	3·08	9·79	0·82	0·37	0·05	<0·05	<0·05	<0·05	<0·05	<0·05	0·49	<0·01	0·09	100·0
28	93 F4 T10	CGF	45·10	Rim	29·3	0·40	<0·02	0·15	21·1	35·4	2·76	8·42	0·62	0·24	<0·05	<0·05	0·06	<0·05	<0·05	<0·05	0·61	<0·01	<0·01	99·1
				Incl	29·5	0·35	<0·02	0·24	17·1	35·8	3·21	10·8	1·03	0·44	<0·05	0·08	<0·05	0·12	<0·05	<0·05	0·71	<0·01	0·03	99·4
29	93 F4 P2	CGF	45·82	Rim	29·1	0·40	<0·02	0·26	16·4	35·3	3·33	11·9	1·02	0·49	<0·05	0·05	0·05	0·06	<0·05	<0·05	1·09	<0·01	0·01	99·5
31	93 F1 I8	CGF	48·60	Rim	30·6	0·46	<0·02	0·19	19·5	35·6	2·87	9·30	0·72	0·35	<0·05	<0·05	0·05	0·09	<0·05	<0·05	1·21	<0·01	0·02	100·9
				Incl	29·9	0·24	<0·02	0·30	14·1	35·1	3·62	12·4	1·18	0·51	<0·05	<0·05	0·08	<0·05	<0·05	<0·05	3·06	<0·01	0·35	100·9
32	95 J1 S3	CGF	49·17	Rim	29·5	0·26	<0·02	0·23	18·0	34·3	3·24	10·9	0·93	0·51	<0·05	<0·05	<0·05	<0·05	<0·05	<0·05	0·79	<0·01	0·67	99·3
				Incl	29·1	0·32	<0·02	0·22	17·2	35·8	3·18	11·1	0·87	0·34	<0·05	<0·05	<0·05	0·11	<0·05	<0·05	0·83	<0·01	0·03	99·0

(continued)

Table 7: Continued

	Sample	Zone	*D* (km)	Type	P_2O_5	SiO_2	ThO_2	Y_2O_3	La_2O_3	Ce_2O_3	Pr_2O_3	Nd_2O_3	Sm_2O_3	Gd_2O_3	Tb_2O_3	Dy_2O_3	Ho_2O_3	Er_2O_3	Yb_2O_3	Lu_2O_3	CaO	PbO	FeO*	Total
33	93 F3 O3	SGF	54·36	Rim	29·5	0·38	<0·02	0·25	17·4	34·6	3·05	10·6	0·94	0·49	<0·05	0·08	0·07	<0·05	<0·05	<0·05	2·85	<0·01	<0·01	100·1
				Incl	28·5	1·24	<0·02	0·29	14·6	35·8	3·65	12·4	1·08	0·48	<0·05	<0·05	<0·05	0·05	<0·05	<0·05	0·77	<0·01	0·15	99·0
34	94 D31 M2	SGF	63·82	Rim	29·2	0·47	<0·02	0·26	18·2	34·6	3·05	10·8	1·03	0·40	<0·05	<0·05	<0·05	0·05	<0·05	<0·05	0·84	<0·01	<0·01	98·9
				Incl	29·5	0·36	<0·02	0·51	12·3	34·8	4·02	15·1	1·62	0·86	<0·05	0·11	<0·05	<0·05	<0·05	<0·05	0·69	<0·01	0·10	100·0
35	93 F11 P2	SGF	67·16	Incl	29·5	0·28	<0·02	0·20	12·5	36·5	3·96	14·3	1·21	0·46	<0·05	<0·05	<0·05	<0·05	<0·05	<0·05	0·68	<0·01	0·25	99·9
36	93 F9 I1	SGF	69·02	Rim	27·9	0·67	<0·02	0·11	12·2	32·9	4·27	17·3	2·24	0·80	<0·05	<0·05	<0·05	<0·05	<0·05	<0·05	0·47	<0·01	0·17	99·0
				Incl	29·4	0·31	<0·02	0·08	12·3	32·5	4·01	17·1	2·11	0·77	<0·05	<0·05	<0·05	0·08	<0·05	<0·05	1·64	<0·01	<0·01	100·3
37	93 F9 H2	SGF	73·10	Rim	29·4	0·38	<0·02	0·15	19·4	35·7	3·00	10·2	0·72	0·33	<0·05	<0·05	<0·05	0·11	<0·05	<0·05	0·32	<0·01	<0·01	99·6
38	93 F6 W1	SGF	77·73	Rim	29·6	0·37	<0·02	0·14	20·2	35·0	2·85	9·07	0·69	0·41	0·06	<0·05	<0·05	0·10	<0·05	0·07	1·05	<0·01	<0·01	99·7
39	93 F9 F8	SGF	78·11	Rim	29·5	0·33	<0·02	0·40	11·3	35·7	3·92	14·8	1·45	0·62	<0·05	0·07	<0·05	<0·05	<0·05	<0·05	1·50	<0·01	0·32	99·9
40	93 F6 W10	SGF	80·33	Rim	29·9	0·36	<0·02	0·09	19·9	35·7	3·09	9·48	0·71	0·19	<0·05	<0·05	<0·05	0·19	<0·05	<0·05	0·78	<0·01	0·28	100·7
43	YD42	SGF	85·71	Rim	30·3	0·28	<0·02	0·16	16·8	35·4	3·41	11·4	0·88	0·35	0·09	<0·05	0·08	0·05	<0·05	<0·05	0·71	<0·01	<0·01	99·9
44	93 F6 X13	SGF	89·24	Rim	28·9	0·42	0·11	0·23	18·6	35·5	3·17	10·2	0·74	0·45	<0·05	0·09	<0·05	0·08	<0·05	<0·05	0·64	<0·01	0·29	99·4
45	93 F9 F5	SGF	90·17	Incl	29·5	0·35	<0·02	0·24	21·0	35·6	2·79	8·76	0·62	0·38	<0·05	0·08	<0·05	<0·05	<0·05	<0·05	0·59	<0·01	<0·01	99·8
46	93 F8 A1	SGF	91·84	Incl	29·3	0·44	<0·02	0·32	17·6	35·3	3·30	11·0	1·02	0·50	0·06	<0·05	<0·05	0·08	<0·05	<0·05	0·71	<0·01	0·07	99·7
47	93 F9 F1	SGF	92·02	Rim	29·5	0·30	<0·02	0·20	16·7	34·6	3·39	12·4	0·95	0·38	<0·05	<0·05	<0·05	0·11	<0·05	<0·05	0·59	<0·01	0·03	99·1
				Incl	29·7	0·34	<0·02	0·20	16·8	34·9	3·32	11·6	1·01	0·48	<0·05	0·05	<0·05	<0·05	<0·05	<0·05	1·52	<0·01	<0·01	99·9
48	93 F7 Z32	SGF	92·57	Rim	27·5	0·69	<0·02	0·39	17·0	35·3	3·41	11·7	1·05	0·63	0·07	0·07	<0·05	0·11	<0·05	<0·05	0·63	<0·01	0·04	98·6
49	93 F9 E3	SGF	94·20	Rim	30·5	0·29	<0·02	0·11	12·9	33·9	4·03	15·8	2·19	0·97	<0·05	<0·05	<0·05	0·08	<0·05	<0·05	0·67	<0·01	0·05	101·5
				Incl	29·5	0·36	0·45	<0·05	17·9	35·0	3·22	12·0	1·14	0·44	<0·05	<0·05	<0·05	0·13	0·05	<0·05	0·12	0·11	0·69	101·0
50	93 F8 D1	SGF	94·99	Rim	30·1	0·29	<0·02	<0·05	10·5	34·2	4·37	17·6	1·48	0·39	<0·05	<0·05	<0·05	<0·05	<0·05	<0·05	1·23	<0·01	0·02	100·2

*Total Fe as FeO·
Rim, rim grain on fluorapatite; Incl, inclusion in fluorapatite·

Table 8: Representative independent monazite grain compositions

	Sample	Zone	*D* (km)	Grain	Description	P_2O_5	SiO_2	ThO_2	UO_2	Y_2O_3	La_2O_3	Ce_2O_3	Pr_2O_3	Nd_2O_3	Sm_2O_3	Gd_2O_3	Tb_2O_3	Dy_2O_3	Ho_2O_3	Er_2O_3	Yb_2O_3	Lu_2O_3	CaO	PbO	FeO*	Total
10	93 F2 L4	NAF	17·44	Mnz 1	dark area	27·8	0·99	2·16	<0·02	0·08	20·9	34·3	2·53	7·17	0·43	0·08	<0·05	<0·05	<0·05	<0·05	<0·05	<0·05	1·25	0·16	<0·01	97·7
					light area	27·0	1·84	7·16	0·08	0·18	18·7	31·5	2·56	7·43	0·60	0·27	<0·05	<0·05	<0·05	0·06	<0·05	<0·05	1·02	0·73	<0·01	99·1
					light area	26·6	1·90	7·36	0·06	0·20	18·8	31·6	2·54	7·50	0·51	0·16	<0·05	<0·05	<0·05	<0·05	<0·05	<0·05	1·02	0·78	0·01	99·1
						27·3	1·32	4·48	0·03	0·11	20·5	32·6	2·58	7·39	0·45	0·21	<0·05	<0·05	<0·05	0·06	<0·05	<0·05	1·04	0·40	0·03	98·5
					dark area	27·5	1·00	2·25	<0·02	0·08	20·7	34·2	2·57	7·22	0·42	0·15	<0·05	<0·05	<0·05	<0·05	<0·05	<0·05	1·32	0·12	0·01	97·6
					dark area	27·3	0·92	1·85	<0·02	0·06	20·5	33·7	2·57	7·48	0·48	0·21	<0·05	<0·05	<0·05	<0·05	<0·05	<0·05	1·38	0·03	0·02	96·6
					dark area	27·2	0·93	2·24	<0·02	0·06	21·0	33·8	2·47	6·94	0·33	0·18	<0·05	<0·05	<0·05	<0·05	<0·05	<0·05	1·27	0·08	0·00	96·5
					dark area	27·3	0·95	1·87	<0·02	0·05	20·4	33·9	2·55	7·42	0·43	0·15	<0·05	<0·05	<0·05	<0·05	<0·05	<0·05	1·37	0·04	0·01	96·5
					light area	26·5	1·65	6·82	0·07	0·16	19·2	31·3	2·40	6·97	0·45	0·22	<0·05	<0·05	<0·05	<0·05	<0·05	<0·05	1·00	0·66	0·01	97·4
					light area	26·4	1·72	7·22	0·07	0·16	18·7	31·3	2·42	7·25	0·51	0·23	<0·05	<0·05	<0·05	<0·05	<0·05	<0·05	1·00	0·72	<0·01	97·6
					light area	26·3	1·78	7·42	0·07	0·18	18·6	31·1	2·43	7·13	0·53	0·18	<0·05	<0·05	<0·05	0·10	<0·05	<0·05	0·99	0·73	<0·01	97·6
				Mnz 2		27·3	1·27	4·78	0·05	0·05	20·9	32·7	2·28	6·96	0·38	0·08	<0·05	<0·05	0·11	0·08	<0·05	<0·05	1·14	0·45	0·01	98·5
						27·3	1·28	4·59	0·02	0·14	19·9	32·5	2·50	7·53	0·57	0·23	0·05	<0·05	0·10	0·10	<0·05	<0·05	1·05	0·43	0·01	98·2
					light area	26·6	1·67	6·65	0·06	0·06	20·3	30·9	2·26	6·58	0·41	0·15	<0·05	<0·05	<0·05	<0·05	<0·05	<0·05	1·37	0·65	0·05	97·7
						27·0	1·26	5·55	0·03	0·04	20·6	31·7	2·33	6·85	0·44	0·20	<0·05	<0·05	<0·05	<0·05	0·33	<0·05	1·15	0·52	0·01	98·0
					light area	25·9	1·94	8·46	0·07	0·04	20·1	30·3	2·16	6·37	0·35	0·17	<0·05	<0·05	<0·05	<0·05	0·36	<0·05	1·14	0·86	0·10	98·2
						26·9	1·33	5·27	0·06	0·04	20·5	31·9	2·38	6·96	0·40	0·14	<0·05	<0·05	<0·05	<0·05	0·29	<0·05	1·05	0·48	<0·01	97·7
11	93 J30 A1	NAF	18·74	Mnz 2	surrounded by allanite rim	26·5	1·86	9·07	0·10	0·03	20·7	30·1	2·02	5·76	0·31	0·14	<0·05	<0·05	<0·05	<0·05	<0·05	<0·05	0·93	0·98	<0·01	98·5
						23·4	3·88	18·0	0·24	0·05	17·6	25·6	1·79	5·17	0·30	0·11	<0·05	<0·05	<0·05	<0·05	<0·05	<0·05	0·86	2·04	<0·01	99·0
				Mnz 3	surrounded by allanite rim	22·1	4·45	17·9	0·21	0·04	17·4	25·5	1·75	5·09	0·31	0·07	<0·05	<0·05	<0·05	0·08	<0·05	<0·05	0·96	1·90	0·01	97·7
				Mnz 4	surrounded by allanite rim	26·9	1·47	7·17	0·08	0·04	21·3	30·8	2·09	5·59	0·25	0·10	<0·05	<0·05	<0·05	<0·05	<0·05	<0·05	1·07	0·73	0·01	97·6
						26·2	1·79	7·54	0·07	0·07	21·0	31·4	2·16	5·82	0·30	0·09	<0·05	<0·05	<0·05	<0·05	<0·05	<0·05	0·76	0·80	0·05	97·9
				Mnz 5		26·2	1·89	9·11	0·11	0·04	21·2	29·9	2·02	5·67	0·26	0·17	<0·05	<0·05	<0·05	<0·05	<0·05	<0·05	0·84	0·99	0·04	98·5
12	93 F2 M2	NAF	22·08	Mnz 3		26·6	1·80	8·25	0·14	0·16	18·5	30·6	2·41	7·46	0·54	0·32	<0·05	<0·05	<0·05	<0·05	<0·05	<0·05	0·63	0·96	0·24	98·6
				Mnz 4		29·3	0·34	0·19	<0·02	0·22	20·7	35·1	2·76	8·52	0·74	0·40	<0·05	<0·05	<0·05	<0·05	<0·05	<0·05	0·30	0·00	0·03	98·6
				Mnz 5		27·7	1·23	5·49	0·07	0·13	19·6	32·1	2·49	7·79	0·55	0·21	0·06	<0·05	<0·05	<0·05	<0·05	<0·05	0·54	0·60	0·01	98·6

(continued)

Table 8: Continued

Sample	Zone	*D* (km)	Grain	Description	P_2O_5	SiO_2	ThO_2	UO_2	Y_2O_3	La_2O_3	Ce_2O_3	Pr_2O_3	Nd_2O_3	Sm_2O_3	Gd_2O_3	Tb_2O_3	Dy_2O_3	Ho_2O_3	Er_2O_3	Yb_2O_3	Lu_2O_3	CaO	PbO	FeO*	Total
14 93 J31 H2	CGF	23·19	Mnz 2	inclusion in allanite	29·0	0·88	1·62	<0·02	0·18	18·2	33·1	2·87	9·35	0·86	0·34	<0·05	<0·05	<0·05	<0·05	<0·05	<0·05	1·01	0·17	0·62	98·2
15 93 F3 N11	CGF	25·42	Mnz 4		29·7	0·47	0·63	<0·02	0·26	19·4	34·7	2·81	8·85	0·75	0·29	<0·05	<0·05	<0·05	<0·05	<0·05	<0·05	0·50	0·01	0·12	98·5
			Mnz 5	associated with Mt and Ilm	28·7	0·42	<0·02	<0·02	0·23	19·3	35·4	2·90	9·52	0·72	0·31	<0·05	<0·05	<0·05	<0·05	<0·05	<0·05	0·26	<0·01	0·46	98·2
			Mnz 10	inclusion in Bt	28·3	0·78	1·79	<0·02	0·24	19·5	33·6	2·82	8·77	0·77	0·31	<0·05	<0·05	<0·05	<0·05	<0·05	<0·05	0·68	0·11	0·06	97·8
18 93 J31 C4	CGF	27·64	Mnz 1		29·0	0·51	1·00	<0·02	0·30	20·4	34·7	2·86	8·93	0·85	0·49	0·06	0·09	<0·05	<0·05	0·07	<0·05	0·53	0·09	<0·01	99·9
					28·2	0·98	3·96	<0·02	0·15	21·4	33·4	2·44	7·51	0·47	0·17	<0·05	<0·05	<0·05	<0·05	<0·05	<0·05	0·72	0·43	0·03	99·8
			Mnz 2		27·7	0·96	2·81	0·03	0·18	21·0	33·4	2·53	7·80	0·52	0·23	<0·05	<0·05	<0·05	<0·05	0·07	<0·05	1·00	0·26	0·01	98·5
			Mnz 3		28·1	1·06	3·51	<0·02	0·18	20·8	33·5	2·56	7·66	0·59	0·20	<0·05	<0·05	<0·05	<0·05	0·08	<0·05	0·75	0·29	0·01	99·2
					29·6	0·35	0·04	<0·02	0·26	20·4	35·2	2·97	9·42	0·77	0·33	<0·05	0·09	<0·05	<0·05	<0·05	<0·05	0·31	0·03	0·08	99·8
			Mnz 5	rim grain on allanite	27·2	1·45	6·03	0·08	0·17	20·1	32·2	2·42	7·65	0·69	0·27	<0·05	<0·05	<0·05	<0·05	0·49	<0·05	0·82	0·62	0·12	100·3
21 93 J31 E2	CGF	30·06	Mnz 2	rim grain on allanite	29·0	0·38	<0·02	<0·02	0·47	15·5	35·7	3·51	12·6	1·35	0·67	<0·05	<0·05	<0·05	<0·05	<0·05	<0·05	0·29	<0·01	0·06	99·5
22 93 F4 T1	CGF	32·1	Mnz 3		28·6	0·66	0·78	<0·02	0·18	21·5	34·6	2·60	8·39	0·62	0·29	0·16	<0·05	<0·05	<0·05	<0·05	<0·05	0·78	<0·01	0·09	99·3
			Mnz 4		28·7	0·76	1·91	<0·02	0·20	20·2	33·9	2·72	8·63	0·67	0·35	<0·05	<0·05	<0·05	<0·05	<0·05	<0·05	0·99	0·15	0·02	99·2
					28·0	0·91	2·58	<0·02	0·20	20·4	33·6	2·61	8·51	0·63	0·34	<0·05	0·06	<0·05	<0·05	<0·05	<0·05	1·02	0·18	0·04	99·1
23 93 F4 R7	CGF	34·7	Mnz 3		27·8	0·61	0·76	<0·02	0·20	19·8	33·9	2·78	8·95	0·62	0·35	<0·05	0·08	<0·05	<0·05	<0·05	<0·05	0·95	0·02	0·06	96·8
			Mnz 4		25·8	1·92	7·91	0·06	0·17	18·3	30·6	2·54	7·90	0·62	0·30	<0·05	<0·05	<0·05	<0·05	<0·05	<0·05	1·18	0·82	<0·01	98·1
			Mnz 5		25·6	1·68	6·03	0·04	0·16	19·3	31·2	2·31	7·72	0·50	0·21	<0·05	<0·05	<0·05	0·05	0·69	<0·05	1·17	0·60	<0·01	97·2
24 93 F4 R5	CGF	35·99	Mnz 3		28·5	0·85	2·28	0·02	0·17	19·7	33·7	2·79	8·75	0·74	0·29	<0·05	<0·05	<0·05	0·10	<0·05	<0·05	0·81	0·20	0·38	99·2
26 95 J1 W3	CGF	40·07	Mnz 3		26·1	1·58	6·02	0·03	0·17	19·0	31·5	2·55	7·83	0·64	0·29	<0·05	<0·05	<0·05	<0·05	<0·05	<0·05	1·20	0·57	0·02	97·5
			Mnz 4		26·6	1·37	4·73	<0·02	0·19	19·9	31·3	2·29	7·40	0·43	0·26	<0·05	<0·05	<0·05	<0·05	<0·05	0·05	1·56	0·41	0·07	96·6
36 93 F9 I1	SGF	69·02	Mnz 1	rim grain on zircon	29·2	0·46	1·11	0·08	<0·05	16·4	33·9	3·25	12·6	1·35	0·37	<0·05	<0·05	<0·05	<0·05	<0·05	<0·05	0·30	0·19	0·06	99·3
			Mnz 2	inclusion in quartz	29·4	0·20	<0·02	<0·02	<0·05	18·5	34·9	3·14	11·1	1·46	0·40	<0·05	<0·05	<0·05	<0·05	<0·05	<0·05	0·20	<0·01	0·01	99·2
39 93 F9 F8	SGF	78·11	Mnz 4		28·9	0·40	<0·02	<0·02	0·27	14·8	35·8	3·54	12·5	1·13	0·40	<0·05	<0·05	<0·05	<0·05	<0·05	<0·05	0·73	<0·01	0·06	98·5

*Total Fe as FeO.

Table 9: Mean and representative allanite compositions (wt %)

	Sample	Zone	*D* (km)	Description	No. pts	P_2O_5	SiO_2	TiO_2	ThO_2	Al_2O_3	Y_2O_3	La_2O_3	Ce_2O_3	Pr_2O_3	Nd_2O_3	Sm_2O_3	Gd_2O_3	FeO	CaO	MgO	MnO	Na_2O	Cl	F	Total
5	93 F2 J1	NAF*	9·83	ind.grain	21	0·02(1)	31·8(6)	1·19(15)	0·79(7)	13·6(6)	0·05(3)	8·05(1)	11·4(6)	0·71(6)	1·77(17)	0·07(4)	0·06(3)	13·8(5)	11·1(6)	1·39(22)	0·20(3)	0·05(2)	0·03(3)	0·23(5)	96·2
8	93 F2 L1	NAF*	14·3	ind.grain	4	<0·01	32·5(9)	0·36(5)	<0·02	18·1(7)	0·03(1)	5·08(83)	7·16(91)	0·56(4)	1·65(16)	0·14(6)	0·05(5)	12·3(3)	15·8(10)	<0·01	0·10(1)	0·01(0)	0·01(0)	0·03(3)	93·8
10	93 F2 L4	NAF*	17·44	ind.grain	4	0·06(6)	31·6(11)	0·70(23)	0·10(6)	15·4(73)	0·04(1)	5·61(48)	10·6(5)	0·91(3)	2·61(18)	0·23(4)	0·09(3)	12·5(5)	12·2(9)	1·20(9)	0·13(4)	0·10(16)	0·03(5)	0·12(3)	94·2
		NAF†	17·44	rim on FAp	1	0·03	32·1	0·04	<0·02	18·6	0·08	4·27	10·4	0·94	3·45	0·34	0·11	9·91	13·4	1·11	0·15	0·05	0·01	0·08	95·1
14	93 J31 H2	CGF*	23·19	ind.grain	1	0·03	30·6	0·55	0·05	15·5	0·04	6·10	11·2	1·00	3·60	0·35	0·12	12·3	11·3	1·32	0·06	0·01	0·01	0·16	94·3
19	93 J31 D1	CGF†	29·87	rim on FAp	2	0·07(4)	29·6(5)	0·14(1)	<0·02	15·3(2)	<0·05	5·87(13)	12·5(0)	1·09(1)	3·50(3)	0·22(1)	0·12(4)	12·2(0)	11·1(2)	1·44(5)	0·11(1)	<0·01	0·02(1)	0·20(3)	93·3
28	93 F4 T10	CGF†	45·1	rim on FAp	2	<0·01	29·3(8)	0·10(2)	<0·02	16·1(4)	0·03(1)	5·30(36)	12·2(1)	1·14(10)	3·78(17)	0·32(4)	0·09(3)	10·9(0)	12·4(5)	1·32(8)	<0·01	<0·01	0·02(1)	0·20(1)	93·2
39	93 F9 F8	SGF†	78·11	rim on FAp	2	0·08(1)	35·8(30)	0·05(1)	<0·02	19·0(4)	0·03(1)	4·38(42)	10·3(11)	1·07(8)	3·60(27)	0·32(1)	0·12(4)	9·82(71)	11·4(13)	1·57(9)	<0·01	0·03(1)	<0·01	0·10(1)	97·5
48	93 F7 Z32	SGF†	92·57	rim on FAp	1	0·09	30·5	0·15	<0·02	18·2	0·05	5·21	10·7	0·97	3·31	0·38	0·14	9·15	12·9	1·46	<0·01	0·04	0·01	0·09	93·2

*Individual grain.
†Rim on FAp.

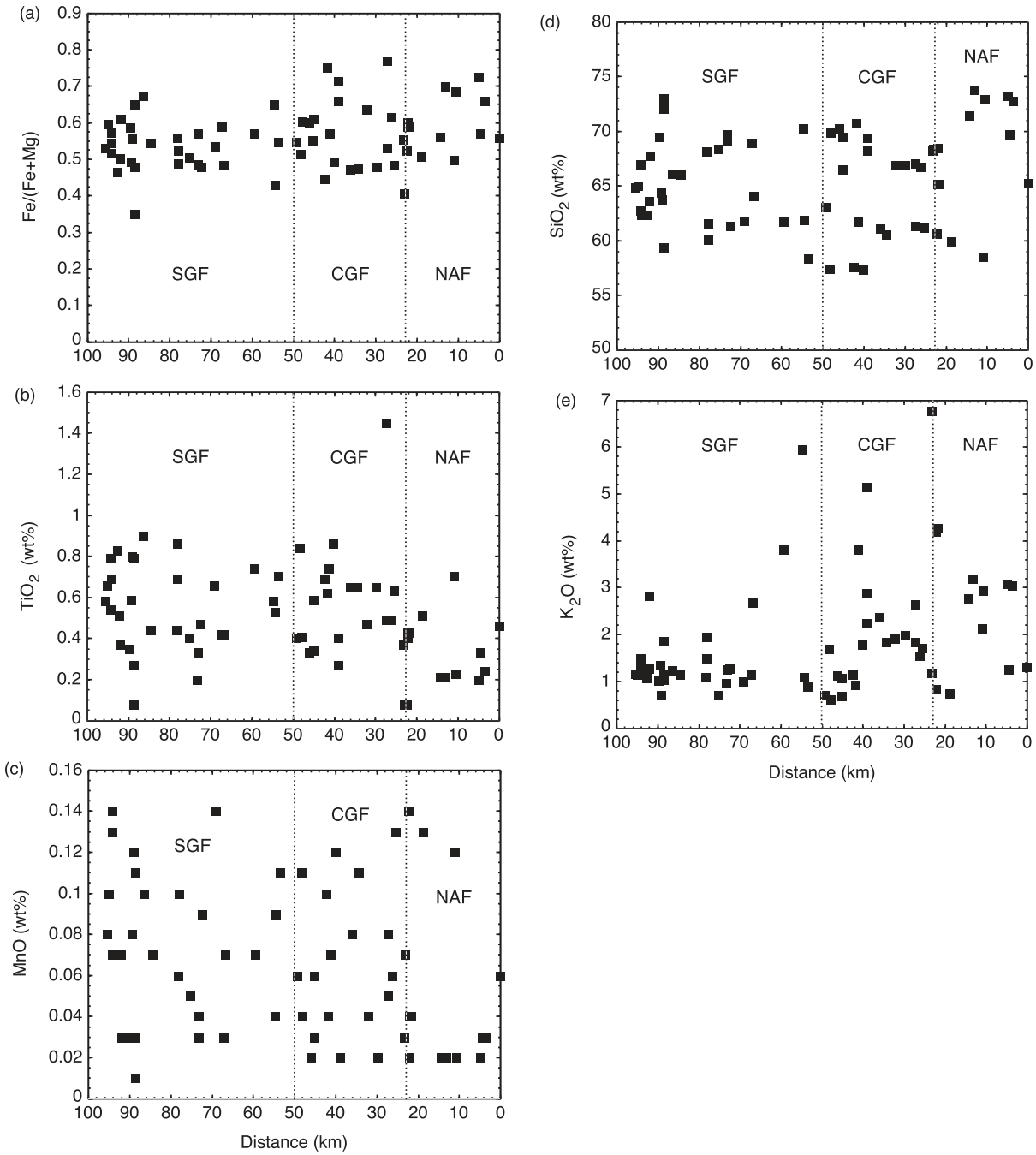

Fig. 2. Plot of whole-rock Fe/(Fe + Mg) atomic ratio (a), TiO_2 (b), MnO (c), SiO_2 (d), and K_2O (e) as a function of distance along a traverse going southwards from the northernmost sample (i.e. 95 J3 I1; see Fig. 1). Dotted lines designate the approximate boundaries between the higher-grade southern granulite-facies zone (SGF), the lower-grade central granulite-facies zone (CGF) and the northern amphibolite-facies zone (NAF).

Despite some scatter, F concentrations (Fig. 6d) show a tendency to be higher in the SGF. Chlorine analyses also show a great deal of scatter but tend to be higher in the CGF and southern NAF than in either the northern NAF or the SGF (Fig. 6e).

Amphibole

In the NAF, amphibole occurs as large grains not confined to any particular mineral association whereas in the SGF it often occurs as small grains directly associated with clinopyroxene and/or orthopyroxene. Amphibole tends

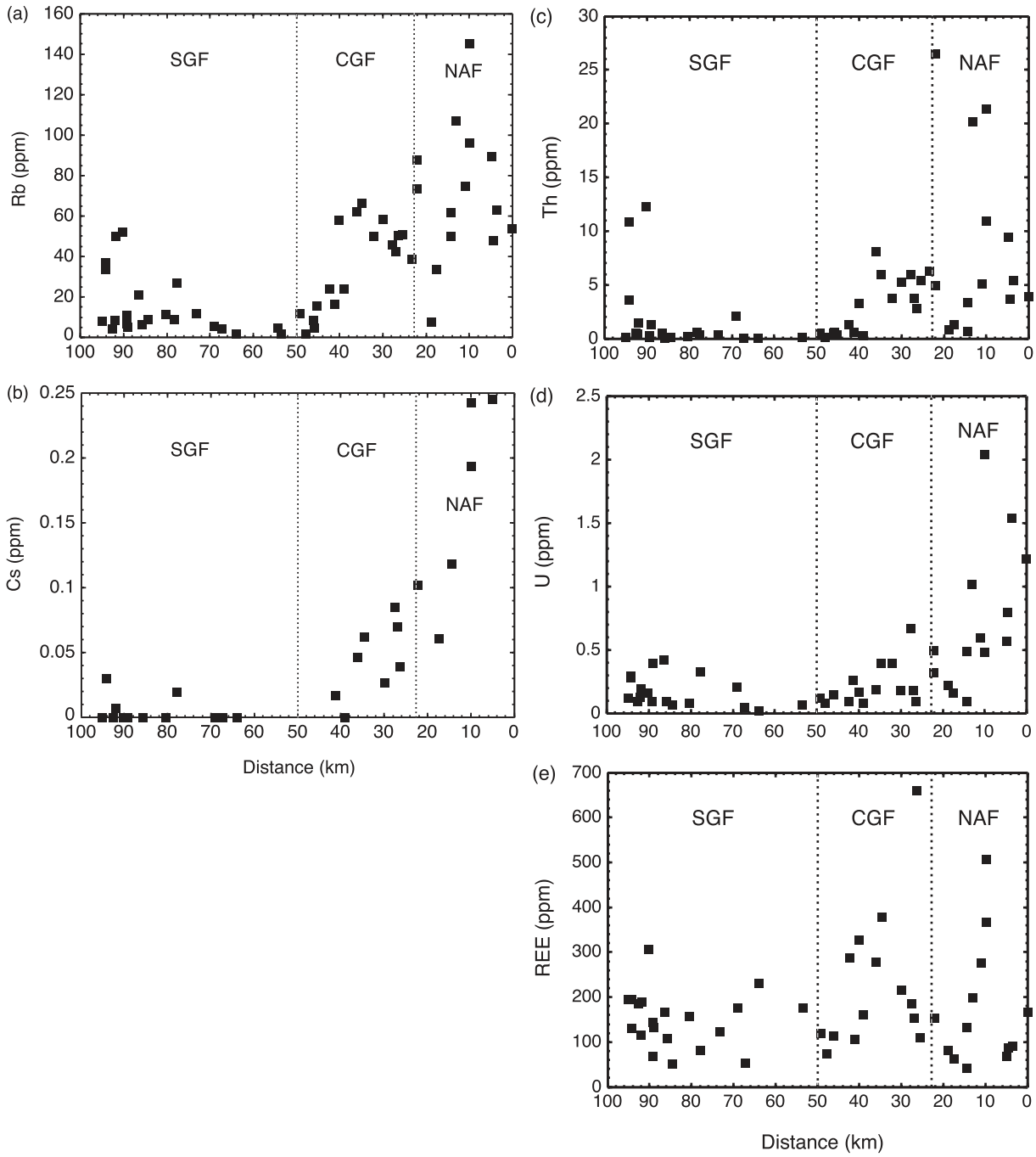

Fig. 3. Plot of whole-rock Rb (a), Cs (b), Th (c), U (d), and total REE (e) (ppm) as a function of distance along a traverse going southwards from the northernmost sample (i.e. 95 J3 1l; see Fig. 1). Data are from Table 2. Dotted lines designate the approximate boundaries between the higher-grade southern granulite-facies zone (SGF), the lower-grade central granulite-facies zone (CGF) and the northern amphibolite-facies zone (NAF).

to show many of the same chemical trends as biotite (Table 5; Fig. 7). Titanium concentrations (Fig. 7a) are too scattered for a regional trend to be clearly discerned, although the lowest values do occur in the amphibolite-facies zone and the highest in the granulite-facies rocks. There is a clear tendency for Fe (Fig. 7b) and Mn (Fig. 7c) to decrease from the northern edge of the traverse to the northern edge of the SGF and then level off. Both K (Fig. 7d) and F (Fig. 7e) concentrations tend to be higher in the southern part of the terrain. In contrast, no clear pattern is discernible in the Cl concentrations (Fig. 7f).

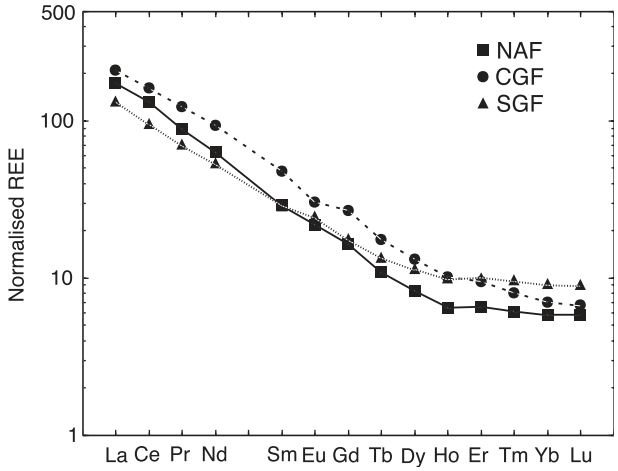

Fig. 4. Average chondrite-normalized whole-rock REE patterns for the northern amphibolite-facies zone (NAF) (continuous line and squares, 14 samples), central granulite-facies zone (CGF) (dashed line and circles, 19 samples) and the southern granulite-facies zone (SGF) (dotted line and triangles, 21 samples). The analyses from which these were calculated are given in Table 2. For normalization the average chondrite composition of Anders & Grevesse (1989) was used.

Orthopyroxene

Orthopyroxene EMPA data were taken from Harlov *et al.* (1997) and Harlov & Hansen (2005) to construct Fig. 8. Alumina concentration (Fig. 8a) increases and Mn content (Fig. 8b) decreases southwards with increasing metamorphic grade. In contrast, except for the far southern margin of the SGF, Fe is relatively constant in orthopyroxene across the traverse (Fig. 8c).

Fluorapatite

In most samples fluorapatite is abundant, with the exception of YD50, which contained no fluorapatite, and 95 J1 V3, in which only two grains were found despite extensive searching. The majority of the fluorapatite grains are euhedral to subhedral and show no obvious preferred orientation or preferential mineral association. Exceptions include zircon, which is frequently associated with 3–4 fluorapatite grains per sample either as an inclusion or, more commonly, as a rim grain, and ilmenite and magnetite, which can be intergrown with anywhere from one to multiple fluorapatite grains.

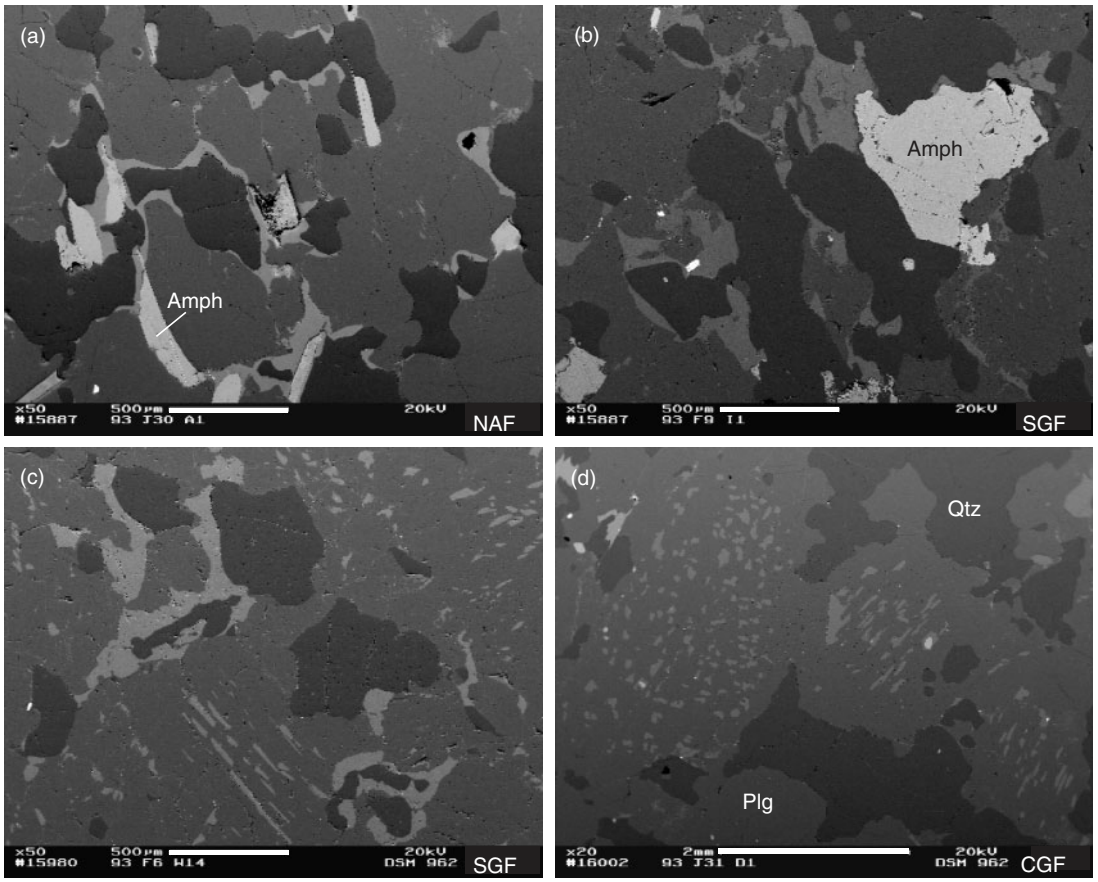

Fig. 5. High-contrast BSE images of various examples of K-feldspar blebs along plagioclase–quartz grain boundaries and Fe–Mg silicate–plagioclase grain boundaries and replacement antiperthite in a series of samples across the Krishnigiri–Salem traverse (see Fig. 1). K-feldspar blebs (light grey) along quartz (black)–plagioclase(dark grey) grain boundaries are shown in (a)–(c). The replacement antiperthite is indicated by the patches of K-feldspar (light grey) in plagioclase (darker grey) in (c) and (d).

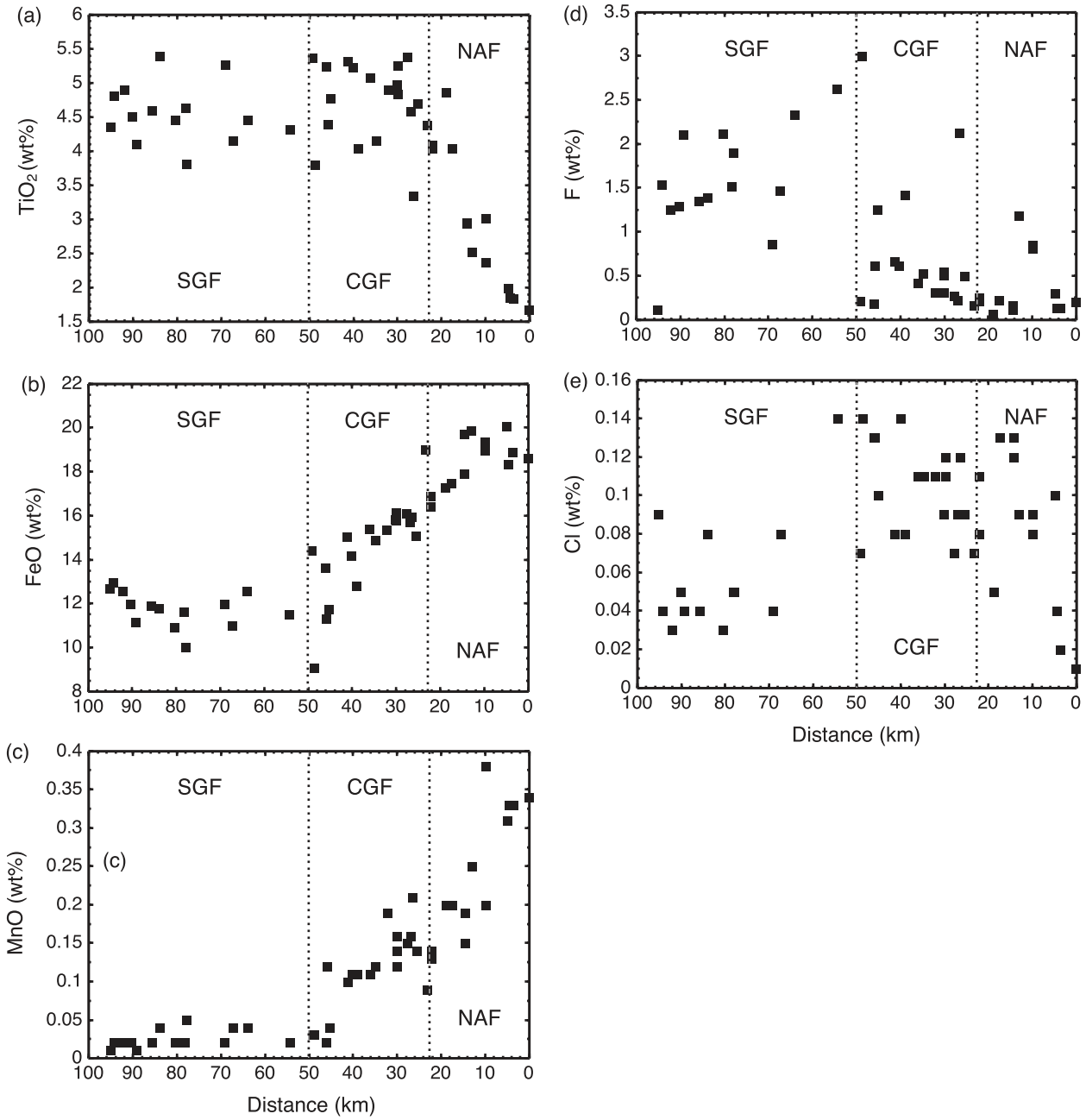

Fig. 6. Plot of biotite composition for TiO_2 (a), FeO (b), MnO (c), F (d), and Cl (e), as a function of distance along a traverse going southwards from the northernmost sample (i.e. 95 J3 1l; see Fig. 1). Dotted lines designate the approximate boundaries between the higher-grade southern granulite-facies zone (SGF), the lower-grade central granulite-facies zone (CGF) and the northern amphibolite-facies zone (NAF).

With the exception of one sample, the fluorapatite along the traverse is unzoned. The exception is sample 95 J31 F5 from the northern border of the CGF. The fluorapatite grains in this sample typically have a darker core surrounded by a light mid section that in some cases gives way to a darker rim (Fig. 9a). Total REE contents of these fluorapatite grains ranged from 2·5 wt % in the light areas to 0·83 wt % in the dark areas (Electronic Appendix 3). Small monazite inclusions occur in a few of the fluorapatite grains in this sample but are much less abundant than in other samples from the CGF and SGF.

In the northern half of the NAF the fluorapatite grains contain no monazite inclusions. Monazite inclusions and rim grains are associated with 10–30% of the fluorapatite in the clinopyroxene zone in the southern half of the NAF (Fig. 1; Table 1). South of the orthopyroxene isograd monazite inclusions and rim grains occur in 80–90% of the fluorapatite grains (Fig. 9). The monazite inclusions vary from multiple

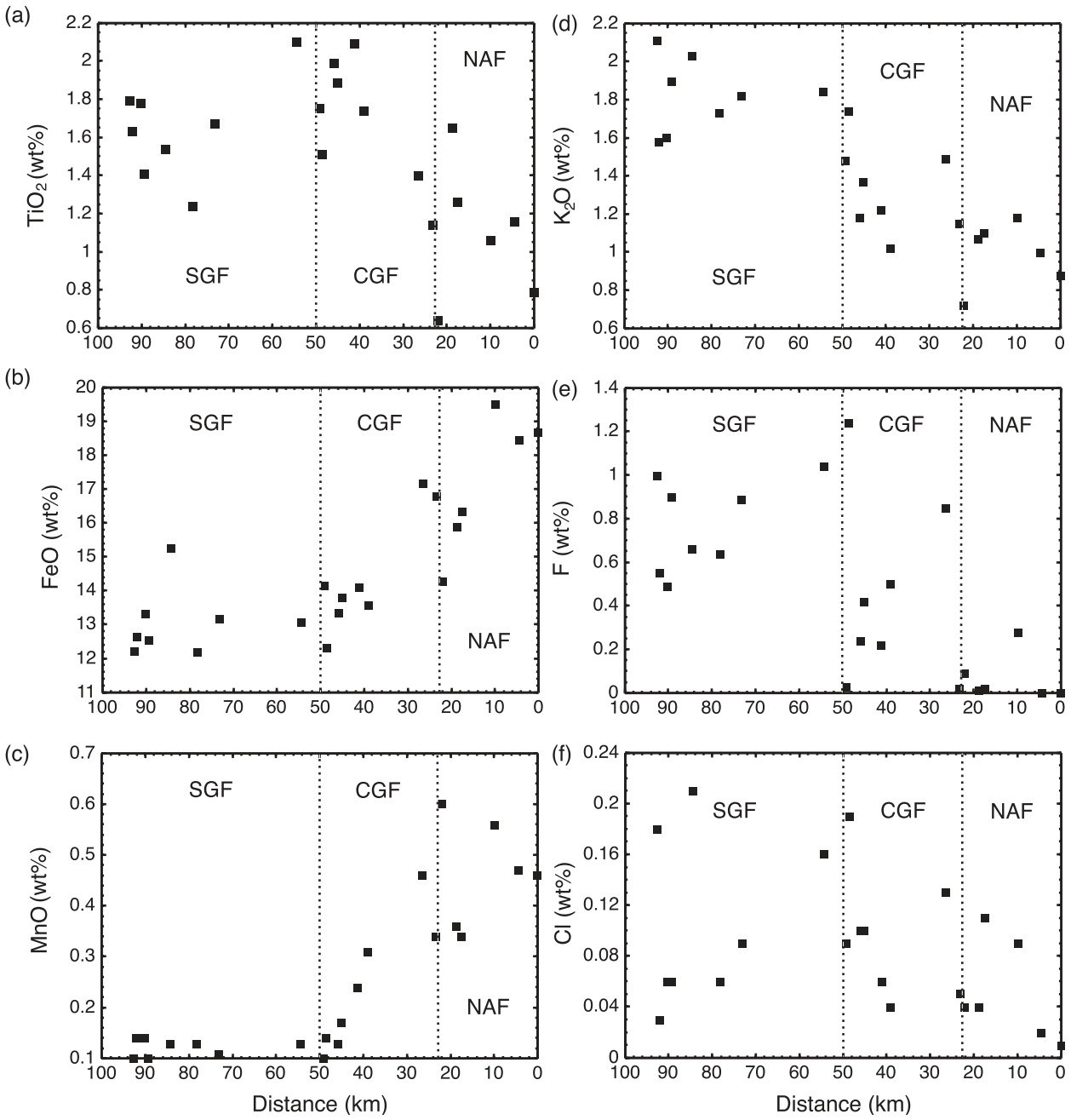

Fig. 7. Plot of amphibole composition for TiO_2 (a), FeO (b), MnO (c), K_2O (d), F (e), and Cl (f) as a function of distance along a traverse going southwards from the northernmost sample (i.e. 95 J3 11; see Fig. 1). Dotted lines designate the approximate boundaries between the higher-grade southern granulite-facies zone (SGF), the lower-grade central granulite-facies zone (CGF), and the northern amphibolite-facies zone (NAF).

very large (>10 μm) inclusions (Fig. 9b and f), to moderately large (>1 μm) inclusions (Fig. 9c), and to numerous, very fine (<1 μm) inclusions (Fig. 9d and g), although these may be interspersed with moderately large inclusions (Fig. 9e). In these cases there may be a halo devoid of small inclusions around the larger ones (Fig. 9e). The very fine monazite inclusions tend to be elongated in cross-sections of fluorapatite cut parallel or obliquely to the *c*-axis (Fig. 9d) and as numerous small dots (Fig. 9g) in fluorapatite grains cut perpendicular to the *c*-axis. In some grains, the monazite inclusions are found associated with micro-voids in the fluorapatite (Fig. 9h). Typically, monazite inclusions from the SGF tend to be coarser, larger, and more sparsely distributed than observed in the CGF (Table 1).

Fluorapatite analyses are given in Table 6 and plotted against distance from the northern edge of the traverse in Fig. 10. All samples with REE concentrations below detection limits occur at the northern or the

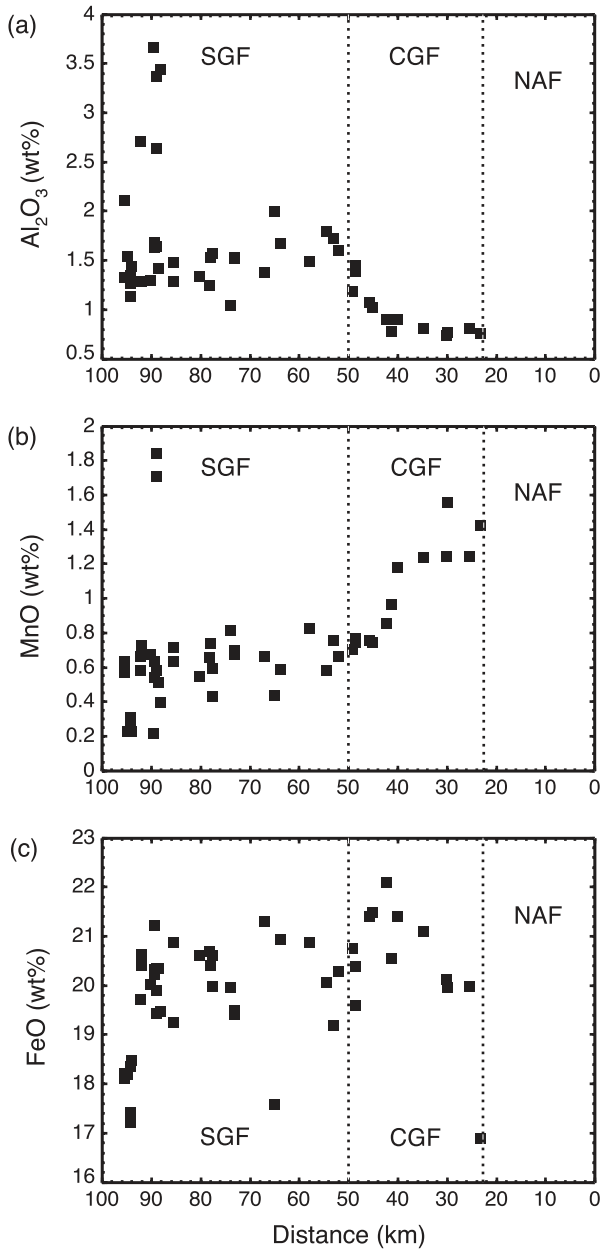

Fig. 8. Plot of orthopyroxene composition for Al_2O_3 (a), MnO (b), and FeO (c) as a function of distance along a traverse going southwards from the northernmost sample (i.e. 95 J3 11; see Fig. 1). Dotted lines designate the approximate boundaries between the higher-grade southern granulite-facies zone (SGF), the lower-grade central granulite-facies zone (CGF) and the northern amphibolite-facies zone (NAF).

southern ends of the traverse. Samples with the highest REE concentrations all occur in the CGF (Fig. 10a). Fluorapatite grains average 0·31 wt % SiO_2 and 0·04 wt % Na_2O, indicating that on an atomic level Si is about four times as abundant as Na. There is also a rough tendency for the SiO_2 concentration to be positively correlated with total REE abundance (Table 6). This implies that the majority of the REE are incorporated in the fluorapatite as the britholite component ($Ca_2REE_3Si_3O_{12}F$) via the coupled substitution $REE^{3+} + Si^{4+} = Ca^{2+} + P^{5+}$ as opposed to the coupled substitution $REE^{3+} + Na^{+} = 2\ Ca^{2+}$ (see Harlov & Förster, 2002*b*). Fluorine concentrations (Fig. 10b) show a great deal of scatter, perhaps partly the result of the problem of halogen diffusion during EMPA (see Stormer *et al.*, 1993). However, they show roughly the same relative halogen patterns as seen for biotite and amphibole, with a tendency for F values to be higher in the southern part of the traverse (compare Figs 6d, 7e and 10b) whereas the Cl content tends to be higher in the CGF compared with the SGF (compare Figs 6e and 10c).

Monazite

Monazite inclusions and rim grains associated with fluorapatite have negligible Th and U contents (Table 7). Chondrite-normalized REE patterns for typical monazite inclusions and rim grains for the six elements detected by EMPA (La, Ce, Pr, Nd, Sm, and Gd) are shown in Fig. 11. For the NAF (Fig. 11a) and the CGF (Fig. 11b) almost all of the rim grains and inclusions fall into a tight cluster of parallel lines of LREE enrichment that are also roughly parallel to the average whole-rock patterns from the same area. Two populations of inclusions and rim grains are evident in the chondrite-normalized plot for the SGF (Fig. 11c). Patterns for Population I inclusions are very similar to the LREE-enriched patterns in the two lower-grade zones. Population II patterns are nearly flat at the LREE end of the plot and in general are richer in heavier LREE. On a plot of chondrite-normalized La/Nd vs distance (Fig. 12), Population I monazite inclusions have La/Nd ratios greater than two. In contrast, Population II monazite inclusions have ratios less than two. In the SGF, Population II monazite makes up 20% (12 out of 61 grains) of the inclusions and rim grains. To the north they make up 4% (two out of 53 grains).

The proportions of monazite inclusions and rim grains relative to their host were obtained for seven samples and ranged from 1·1 to 3·9% (Table 10). These proportions were used to obtain 'reintegrated' compositions for the fluorapatite grains using EMPA results for these samples. A value of 1·6 was used for the ratio between the density of monazite and fluorapatite. These reintegrated compositions imply that the original fluorapatite grains contained from 1·5 to 4·4 wt % total REE (Table 10).

Despite extensive searching, monazite grains independent of fluorapatite were found in only 16 samples, 14 of which occur in the southern quarter of the NAF and the northern half of the CGF (shaded region in Fig. 1; open circles in Fig. 12). This region correlates roughly with the clinopyroxene zone of Hansen *et al.* (1995), in which clinopyroxene rather than orthopyroxene is the dominant pyroxene. Within this area, monazite occurs both as independent

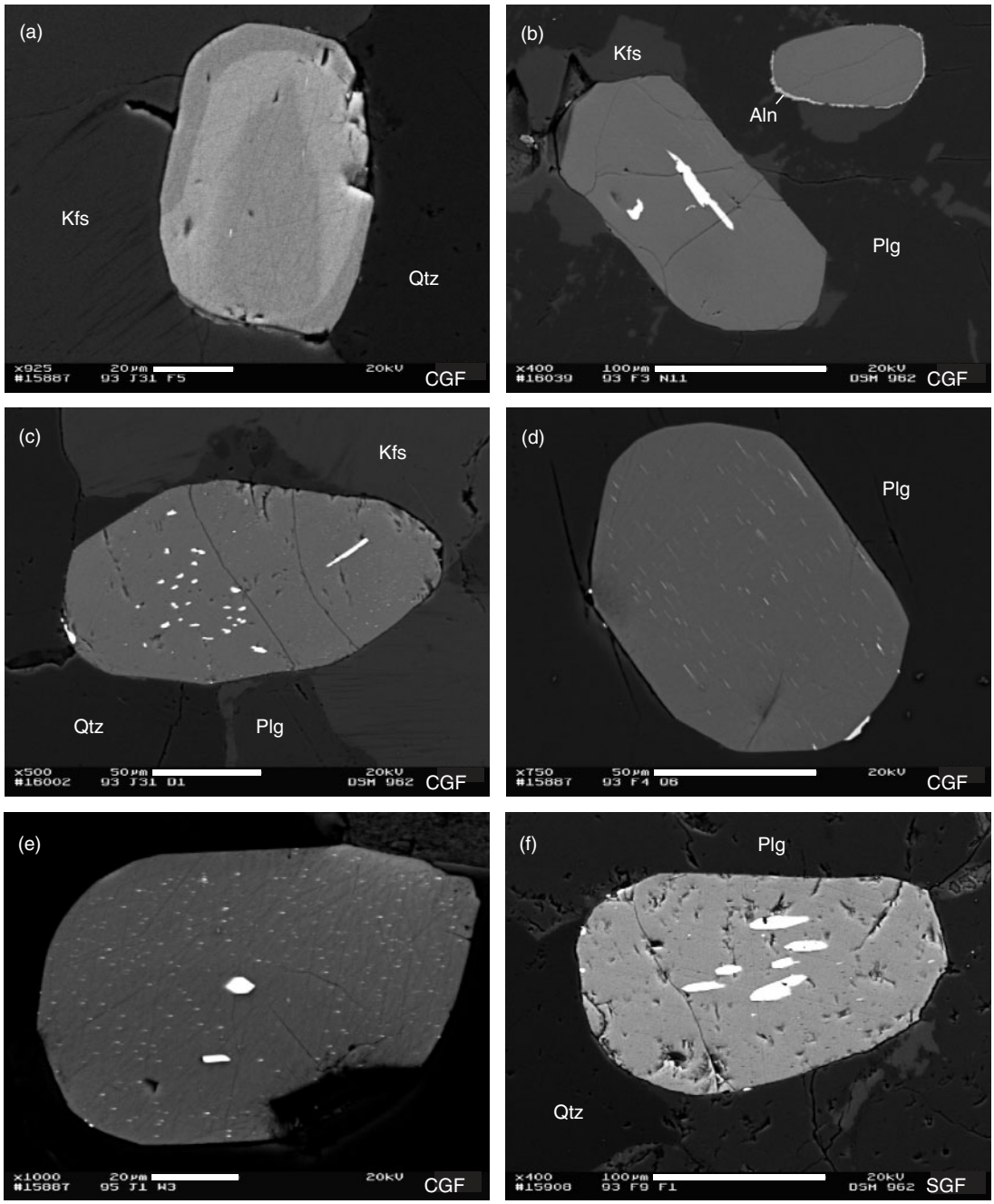

Fig. 9. High-contrast BSE images of a variety of fluorapatite (dark grey) and monazite inclusion and rim grains (bright) textures in a series of samples across the Krishnigiri–Salem traverse (see Fig. 1). (a) Zoned fluorapatite from sample 93 J31 F5. (b) Fluorapatite grain with several large monazite inclusions in the centre. The smaller fluorapatite grain in the upper right-hand corner has a nearly continuous rim of allanite (lighter grey) around the fluorapatite grain (darker grey). (c) Fluorapatite grain with moderate-sized monazite inclusions; a fine powdering of very small (<0·5 μm) monazite inclusions is seen in some areas. Monazite rim grain on left-hand side. (d) Fluorapatite grain with numerous, very thin monazite inclusions preferentially elongated parallel to the *c*-axis. Monazite rim grain on lower right side. (e) Fluorapatite grain with numerous small inclusions (<1 μm). Two moderate-sized monazite inclusions are surrounded by 'halos' devoid of smaller inclusions, suggesting some sort of Ostwald ripening effect (see Harlov *et al.*, 2005). (f) Fluorapatite grain with moderate-sized to large monazite inclusions partially elongated parallel to the *c*-axis typical for the SGF. (g) Small monazite inclusions (<1 μm) in a fluorapatite grain cut perpendicular to the *c*-axis. (h) An example of a fluorapatite grain in which the monazite inclusions are accompanied by partial voids.

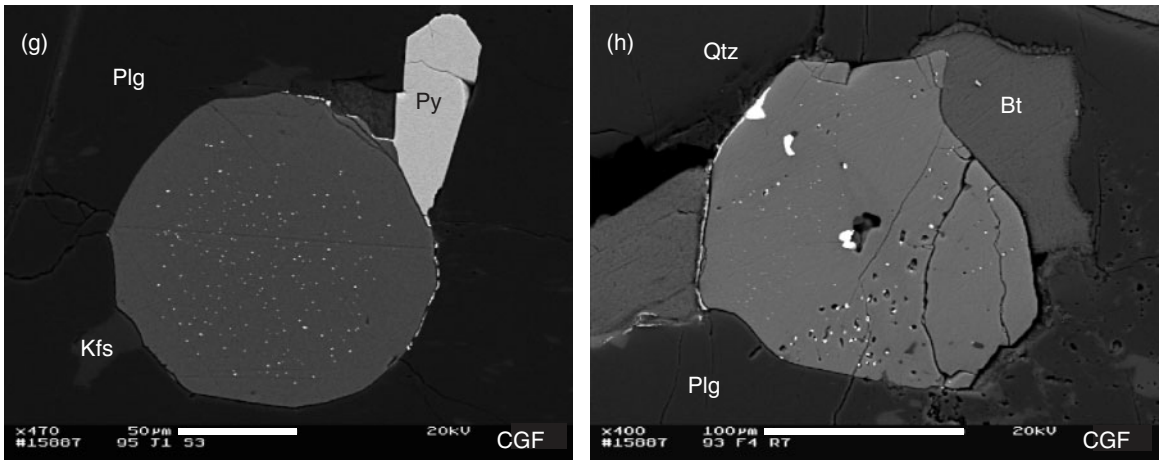

Fig. 9. Continued.

grains, in places rimmed by allanite (Fig. 13a), and as rims and inclusions on and in fluorapatite. Monazite grains not directly associated with fluorapatite all have detectable Th. In a few grains ThO_2 reaches values of 18 wt %, although more typically it ranges from 1 to 10 wt % (Table 8). The grains range from featureless to zoned. Zoning typically takes the form of a series of curvilinear, $ThSiO_4$-enriched, lobate-like intergrowths with sharp compositional boundaries occurring both along grain rims and in grain interiors (Fig. 13b–d). These intergrowths are very similar to intergrowths produced experimentally by the reaction of Th-bearing monazite with high-pH fluids such as NaOH, KOH, and $Na_2Si_2O_5 + H_2O$ (Harlov *et al.*, 2007). In some grains these $ThSiO_4$-enriched zones overprint an earlier, possibly igneous zoning pattern, consisting of rectilinear zones (Fig. 13c).

To the south, this zone of independent monazite grains ends in roughly the same place where Th depletion becomes evident in the whole-rock data (compare Figs 1 and 3c). All monazites found south of this border were inclusions or rim grains directly associated with fluorapatite except for two small independent grains and one grain associated with zircon. Of these only the monazite associated with zircon has Th concentrations high enough to be detectable by EMPA (Table 8). The chondrite-normalized La/Nd ratios from independent monazite grains and monazite inclusions are compared in Fig. 12. Independent monazite grains in the northern CGF and southern NAF show somewhat more enrichment in LREE than do the inclusions and rim grains from the same area. At the same time, the three monazite grains not associated with fluorapatite in the SGF have REE patterns nearly identical to the REE patterns in the monazite inclusions associated with fluorapatite from the same rocks (see also Fig. 11).

Allanite

Allanite is commonly found as thin rims on fluorapatite (Fig. 9b; Tables 1 and 9). Although they occur throughout the traverse, these rims are most common in samples from the CGF and SGF. Allanite was also found as patchy large (10–100 μm), independent grains in some samples from the NAF (Tables 1 and 9) and the northernmost CGF, as well as thick rims on monazite in one sample from the southern half of the NAF (Fig. 13a). Independent allanite grains contain moderate amounts of ThO_2, generally <1 wt %. In contrast, ThO_2 in allanite rims on fluorapatite is generally below the EMPA detection limit (Table 9). Chondrite-normalized REE patterns for the six elements detected by EMPA (La, Ce, Pr, Nd, Sm, and Gd) for allanite are shown in Fig. 14. All allanite grains have negative slopes with strong LREE enrichment. As was the case with monazite inclusions and rim grains associated with fluorapatite compared with independent monazite grains, the allanite rims on fluorapatite are slightly less enriched in LREE compared with the independent allanite grains. The REE patterns for the large allanite grains are somewhat more LREE enriched than the whole-rock pattern from the same area (NAF and the northernmost CGF).

Titanite

Titanite is widespread in the NAF but was found in only one sample south of the orthopyroxene isograd (Table 1). In the northernmost sample, small inclusions of hemoilmenite are found within large titanite grains (Fig. 15a). The thickness of the titanite rims tends to decrease southwards (Fig. 15b and c) such that near the southern border of the NAF titanite generally forms thin rims on the ilmenite grains (Fig. 15d). The titanite is relatively rich in (Y + REE) (up to 2·5 wt %), contains variable amounts of Nb_2O_5, negligible amounts of ThO_2, UO_2 and ZrO_2, and substantial amounts of F (Table 11). The chondrite-normalized REE pattern for the titanite is relatively flat, despite the fact that the whole-rock REE pattern shows

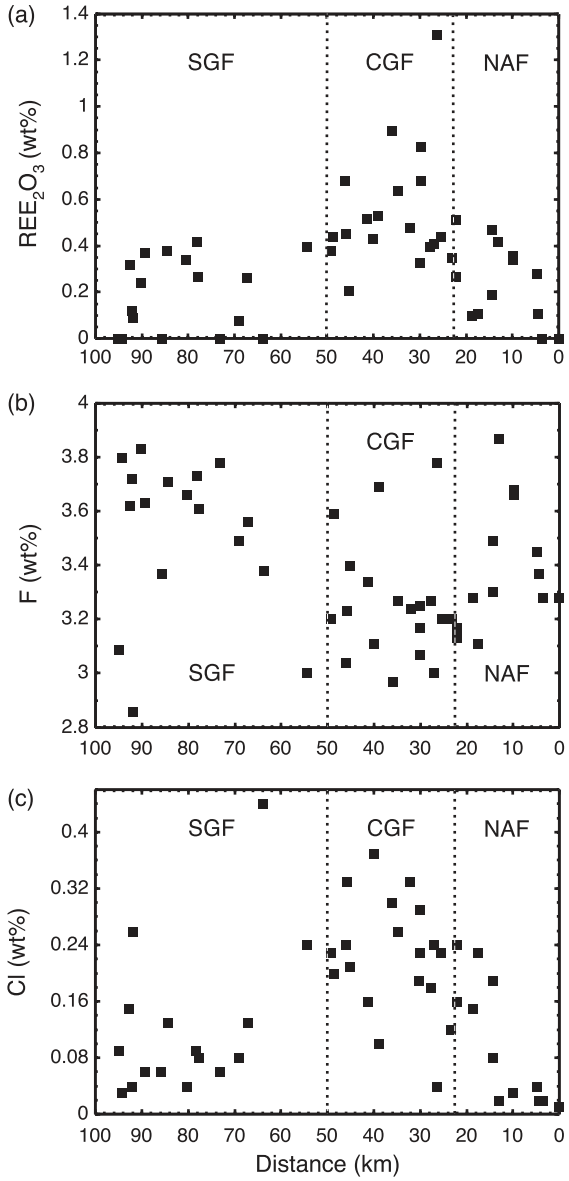

Fig. 10. Plot of fluorapatite composition for REE_2O_3 (a), F (b), and Cl (c) as a function of distance along the traverse going southwards from the northernmost sample (i.e. 95 J3 I1; see Fig. 1). Only one fluorapatite was analyzed in sample 93 F9 E3 and the F value was above the stochiometric maximum (see Table 6). Therefore its value was not included in these plots. Dotted lines designate the approximate boundaries between the higher-grade southern granulite-facies zone (SGF), the lower-grade central granulite-facies zone (CGF), and the northern amphibolite-facies zone (NAF).

a definite LREE enrichment (Fig. 14). Titanite–oxide–silicate relationships in the NAF have already been explored in detail by Harlov & Hansen (2005) and Harlov *et al.* (2006*b*).

Remaining silicate and oxide minerals

Quartz was present in all the samples studied. The occurrence, texture and compositions of plagioclase, garnet, and clinopyroxene have been described by Hansen *et al.* (1995). Plagioclase in the intermediate to felsic orthogneisses typically ranges from An 20 to An 40 in composition. It is generally unzoned, except near the margins with K-feldspar grain boundary blebs, where it may be enriched in anorthite. Replacement antiperthite, as described by Griffin (1969), is also seen in a scattering of samples along the traverse (Fig. 5c and d; Table 1). Reintegration of the antiperthite to a composite composition results in plagioclase grains with a K-feldspar component that plots far out in the feldspar ternary, indicating disequilibrium between the plagioclase and local K-feldspar (Harlov *et al.*, 1998). Perthitic K-feldspar is common in samples with more than 2 wt % K_2O and is most abundant in the NAF and CGF. In intermediate to felsic orthogneisses garnet is found only in the SGF and is abundant only in the southernmost SGF. It most often occurs in euhedral to subhedral crystals with large unzoned cores and a slight enrichment in grossular at the rims. Clinopyroxene in the orthogneisses is generally a low-Al (1·0–3·0 wt % Al_2O_3) augite (Hansen *et al.*, 1995; Harlov & Hansen, 2005).

Oxides and sulphides across the traverse have been described by Harlov *et al.* (1997) and Harlov & Hansen (2005). Magnetite occurs in most samples. Ilmenite is relatively rare in the lower-grade NAF and is generally rimmed by titanite. Ilmenite becomes more abundant southwards in the CGF and is nearly ubiquitous in the SGF. Ilmenite grains in the CGF and especially the SGF typically contain hematite lamellae, which make up anywhere from 10 to 60% of the grain in all but a handful of samples. Pyrrhotite is confined to the SGF and occurs in those samples where the hematite lamellae abundance in ilmenite is less than 40%. Pyrite occurs throughout the traverse.

DISCUSSION

Formation of K-feldspar blebs along grain boundaries

K-feldspar grain boundary networks and associated replacement antiperthite have been interpreted by a series of workers to be due to the action of a K-rich fluid flowing along grain boundaries (e.g. Perchuk & Gerya, 1992; Hansen *et al.*, 1995; Harlov *et al.*, 1998; Harlov & Förster, 2002*a*, 2002*b*). This hypothesis has been confirmed in recent experiments described by Harlov (2005) in which supercritical KCl brines were used to dehydrate a biotite-bearing tonalitic gneiss to an orthopyroxene- and clinopyroxene-bearing enderbite at 900°C and 1000 MPa. One by-product of the experiment was the formation of continuous grain boundary blebs of K-feldspar along quartz–plagioclase grain boundaries, as well as replacement antiperthite.

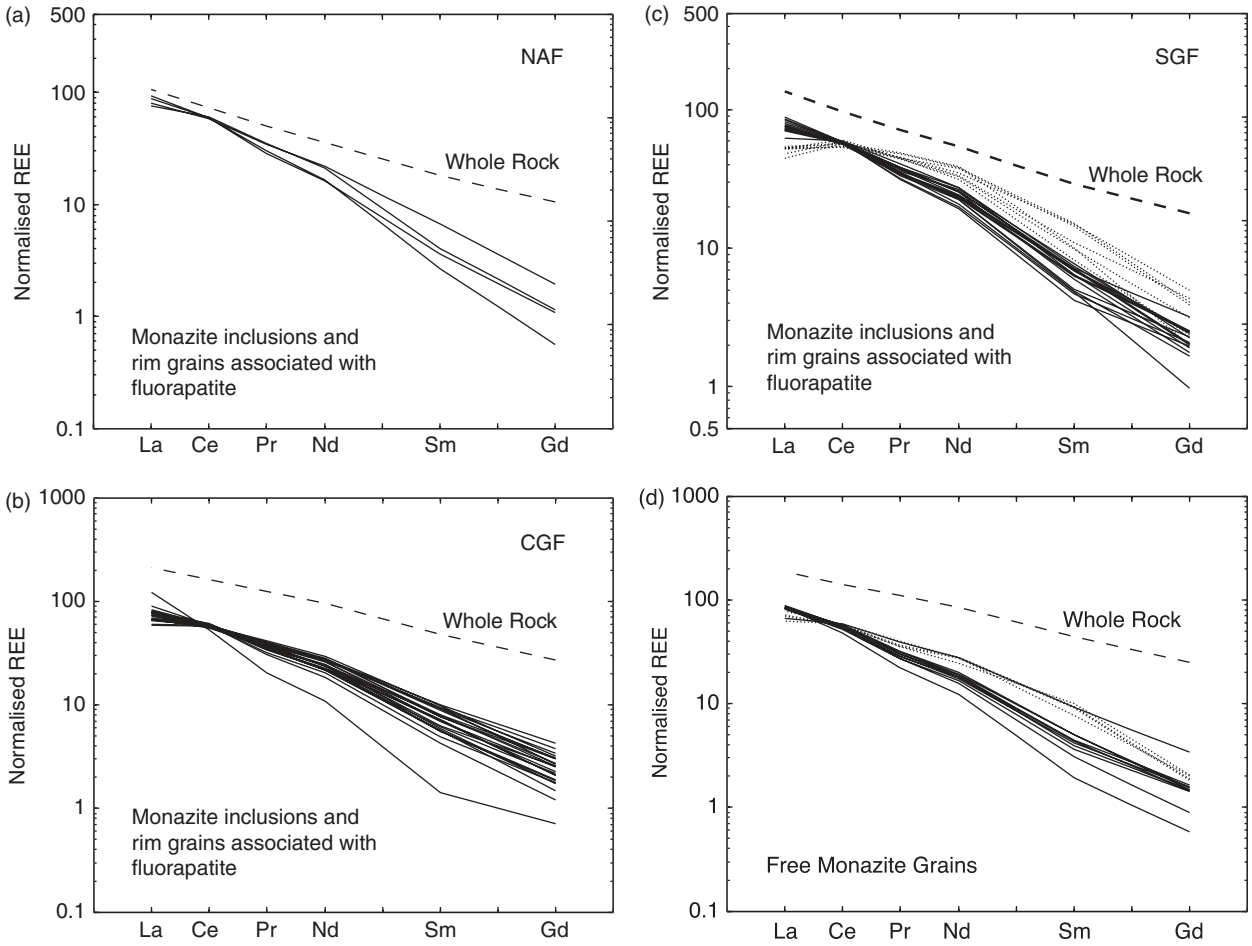

Fig. 11. Chondrite-normalized (divided by 10 000) LREE patterns for typical monazite inclusions in and rim grains on fluorapatite from the northern amphibolite-facies zone (NAF) (a), central granulite-facies zone (CGF) (b), and southern granulite-facies zone (SGF) (c), as well as independent monazite grains not directly associated with fluorapatite (d). Analyses for (a)–(c) are from Table 7, whereas (d) shows the average for each sample in Table 8. The dashed lines represent the average chondrite-normalized (not divided by 10 000) whole-rock composition for each zone. The dotted lines in (c) represent the less LREE rich Population II monazite inclusions and rim grains. The dotted lines in (d) are the independent monazite grains from the SGF. For normalization the average chondrite composition of Anders & Grevesse (1989) was used.

The common occurrence of K-feldspar blebs along plagioclase margins can be explained by a set of metasomatic reactions:

$$\underset{\text{in solution}}{K^+} + \underset{\text{in plagioclase}}{NaAlSi_3O_8} = \underset{\text{K-feldspar}}{KAlSi_3O_8} + \underset{\text{in solution}}{Na^+} \qquad (3)$$

and

$$\underset{\text{in solution}}{2\,K^+} + \underset{\text{in plagioclase}}{CaAlSi_3O_8} + \underset{\text{quartz}}{SiO_2} = \underset{\text{K-feldspar}}{2\,KAlSi_3O_8} + \underset{\text{in solution}}{Ca^{2+}}. \qquad (4)$$

Reaction (3) may explain why the plagioclase near these grain boundary blebs is occasionally enriched in anorthite (Hansen *et al.*, 1995). Reaction (4) could explain why the grain boundary blebs are commonly found along quartz–plagioclase grain boundaries.

The assemblage represented by the K-feldspar grain-boundary blebs (quartz, plagioclase and K-feldspar) is also the assemblage expected from the crystallization of a leucogranite melt. Very similar features in other rocks have been interpreted as the remnants of isolated melt pools (Sawyer, 2001). Harlov (2005) also described experiments in which K-feldspar blebs form on pre-existing quartz grains during the slow isobaric cooling of a tonalitic gneiss that has undergone dry partial melting. Thus the K-feldspar blebs can be interpreted as indicating that the rocks underwent either partial melting or melt infiltration. Replacement antiperthite cannot be interpreted this way and its presence suggests metasomatic reactions similar to reactions (3) and (4). However, whereas K-feldspar grain boundary blebs are nearly ubiquitous throughout the traverse, replacement antiperthite is absent from the NAF,

occurs sporadically in the CGF, and is common only in the SGF (Table 1).

Systematic trends in mineral composition

Systematic changes in mineral composition with increasing metamorphic grade (Figs 6, 7, 8 and 10) can reflect the effect of changes in temperature or pressure, the influence of a fluid phase, systematic changes in whole-rock composition, or fractionation effects during progressive metamorphism. For example, an increase in the Al concentration of orthopyroxene (Fig. 8a) going from the CGF to the SGF probably reflects an increase in temperature. This has been documented experimentally by Aranovich & Berman (1997), and in natural systems by Nijland *et al.* (1998) and Morishita *et al.* (2003). A temperature increase is also indicated by the geothermometry for this area (Harlov & Hansen, 2005).

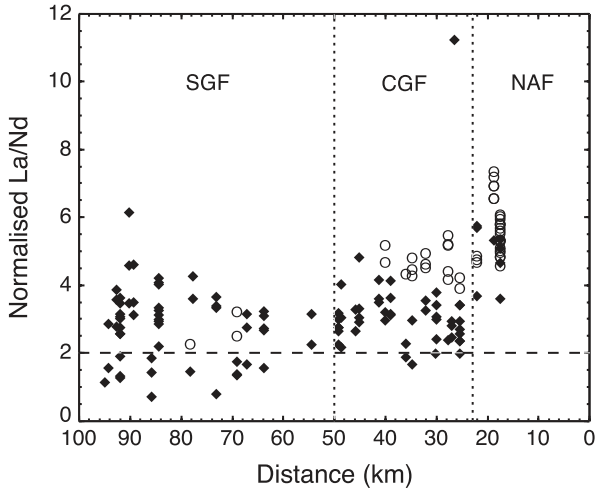

Fig. 12. Chondrite-normalized La/Nd ratios for monazite grains associated with fluorapatite (◆) and monazite grains independent of fluorapatite (○) plotted as a function of distance along the traverse going southward from the northernmost sample (i.e. 95 J31 I1; see Fig. 1). All of the monazite analyses (Electronic Appendix 4) are plotted on this diagram. The horizontal dashed line represents the boundary between more LREE-rich Population I monazite inclusions and rim grains (La/Nd >2) and less LREE-rich Population II monazite inclusions and rim grains (La/Nd <2). Dotted lines designate the approximate boundaries between the higher-grade southern granulite-facies zone (SGF), the lower-grade central granulite-facies zone (CGF) and the northern amphibolite-facies zone (NAF). For normalization the average chondrite compositions of Anders & Grevesse (1989) was used.

An increase in the abundance of K_2O in amphibole (Fig. 7d) southwards across the CGF into the SGF cannot be a consequence of changes in the whole-rock composition because, if anything, whole-rock K_2O appears to decrease in the same direction (Fig. 2e). A similar decrease in K_2O across the amphibolite- to granulite-facies transition has been noted in metabasites from south India (Raase *et al.*, 1986) and Brazil (Ferreira Filho *et al.*, 1998). It has been attributed to a combination of increasing temperature and a fractionation effect as progressive dehydration by reaction (2) enriches the residual amphibole in a $KCa_2(Mg,Fe)_5Si_7AlO_{22}(OH)_2$ component (Raase *et al.*, 1986).

The decrease in the concentration of Fe with respect to Mg in biotite and amphibole southwards along the traverse cannot be a consequence of changes in the whole-rock composition because whole-rock Fe/(Fe + Mg) displays no systematic trend (Fig. 2a). Thus some other phase must have preferentially incorporated Fe in the southern portion of the traverse. This phase cannot be orthopyroxene as it tends to have nearly the same Fe/(Fe + Mg) ratio as the biotite in the same rock, nor can it be clinopyroxene, which tends to have a lower Fe/(Fe + Mg) ratio than biotite (data from Harlov & Hansen, 2005). The other widespread Fe-bearing phases in these rocks are magnetite, pyrite and hemo-ilmenite. Of these only hemo-ilmenite shows a marked increase in abundance to the south (Harlov & Hansen, 2005). This suggests that the decrease in Fe concentrations in amphibole and biotite with increasing

Table 10: Reintegrated REE compositions of fluorapatites with monazite inclusions

Sample	Zone	*D* (km)	% Mnz in FAp	Reintegrated composition (wt %)						
				La_2O_3	Ce_2O_3	Pr_2O_3	Nd_2O_3	Sm_2O_3	Gd_2O_3	Total REE
93 F3 N11	CGF	25·42	1·44	0·42	0·99	0·25	0·29	0·03	0·01	1·99
93 F4 Q6	CGF	38·96	1·12	0·33	0·94	0·27	0·17	0·02	0·01	1·74
93 F4 T10	CGF	45·10	1·35	0·41	0·86	0·18	0·21	0·02	0·01	1·69
95 J1 S3	CGF	49·17	1·52	0·52	0·97	0·24	0·27	0·02	0·01	2·03
93 F11 P2	SGF	67·16	1·17	0·23	0·79	0·22	0·27	0·02	0·01	1·54
93 F9 F5	SGF	90·17	1·50	0·50	0·97	0·18	0·21	0·01	0·01	1·89
93 F8 D1	SGF	94·99	3·89	1·10	2·20	0·29	0·68	0·06	0·03	4·36

Table 11: Mean titanite compositions (wt %)

	Sample	Zone	*D* (km)	No. pts	P_2O_5	Nb_2O_5	SiO_2	TiO_2	ZrO_2	HfO_2	ThO_2	UO_2	Al_2O_3	Fe_2O_3	Y_2O_3	La_2O_3	Ce_2O_3	Pr_2O_3	Nd_2O_3	Sm_2O_3	MgO	CaO	MnO	Na_2O	F	Total
1	95-J3-11	NAF	0	17	0·08(2)	0·14(4)	29·9(3)	36·9(4)	0·02(1)	<0·01	0·02(1)	0·02(2)	1·29(2)	1·50(8)	0·20(5)	0·17(4)	0·69(9)	0·09(4)	0·50(8)	0·07(2)	0·01(1)	27·2(3)	0·09(2)	0·02(1)	0·16(5)	99·1
2	95-J3-H5	NAF	3·53	14	0·03(1)	0·13(3)	30·2(2)	37·0(3)	0·01(1)	<0·01	0·03(1)	0·02(1)	1·63(3)	1·31(5)	0·18(4)	0·10(3)	0·42(6)	0·06(2)	0·32(6)	0·08(2)	0·01(1)	27·4(2)	0·09(3)	0·02(1)	0·24(5)	99·2
3	95-J3-H2	NAF	4·45	17	0·04(1)	0·08(2)	29·3(3)	37·5(3)	0·01(1)	<0·01	<0·02	<0·02	1·56(4)	1·36(6)	0·09(2)	0·05(2)	0·21(3)	<0·05	0·15(3)	0·06(2)	0·01(1)	28·0(4)	0·09(2)	0·02(2)	0·32(6)	98·8
4	93-F11-R1	NAF	4·82	5	0·06(2)	0·38(5)	29·7(2)	35·6(2)	0·03(1)	0·01(1)	<0·02	<0·02	1·64(5)	1·88(4)	0·49(6)	<0·05	0·81(10)	<0·05	0·69(7)	0·15(3)	0·02(1)	26·6(3)	0·12(4)	0·02(1)	0·26(4)	98·3
5	93-F2-J1	NAF	9·83	10	0·07(2)	0·26(4)	30·2(1)	35·9(2)	0·05(2)	<0·01	0·04(1)	<0·02	1·86(5)	1·92(7)	0·20(4)	0·28(5)	1·03(11)	0·12(5)	0·50(8)	0·09(1)	0·03(1)	27·0(3)	0·13(2)	0·03(2)	0·50(8)	100·1
6	93-F2-J2	NAF	9·83	11	0·09(2)	0·33(5)	29·0(2)	34·6(3)	0·04(2)	<0·01	0·02(1)	<0·02	1·88(4)	1·81(6)	0·12(4)	0·15(4)	0·55(5)	0·06(3)	0·27(5)	<0·05	0·03(2)	27·0(4)	0·14(5)	0·03(1)	0·59(6)	96·5
7	93-F2-K2	NAF	12·99	16	0·04(1)	0·18(4)	30·5(2)	35·2(1)	0·02(1)	<0·01	0·02(1)	<0·02	2·49(8)	1·95(8)	0·06(2)	0·11(3)	0·39(4)	<0·05	0·18(4)	0·05(2)	0·03(1)	27·7(2)	0·12(3)	0·03(2)	0·96(9)	99·6
8	93-F2-L1	NAF	14·3	4	0·04(2)	0·23(3)	31·0(1)	37·7(4)	0·01(1)	<0·01	<0·02	<0·02	1·42(7)	1·18(5)	<0·05	0·11(4)	0·23(3)	<0·05	0·05(1)	<0·05	0·01(1)	28·3(4)	0·08(3)	0·01(1)	0·30(3)	100·7
9	93-F2-L2	NAF	14·3	6	0·05(1)	0·20(3)	30·8(3)	37·4(4)	0·03(1)	<0·01	<0·02	<0·02	1·63(5)	1·26(3)	<0·05	<0·05	0·13(2)	<0·05	0·09(4)	<0·05	0·01(1)	28·1(3)	0·09(4)	0·04(1)	0·44(6)	100·3
16	93-J31-F5	CGF	26·35	18	0·06(2)	0·18(2)	29·8(3)	34·0(3)	0·05(2)	0·02(1)	<0·02	<0·02	2·59(9)	2·34(9)	0·31(8)	<0·05	1·30(9)	<0·05	0·77(8)	0·14(3)	0·08(3)	26·5(3)	0·14(4)	0·04(2)	0·81(8)	98·7

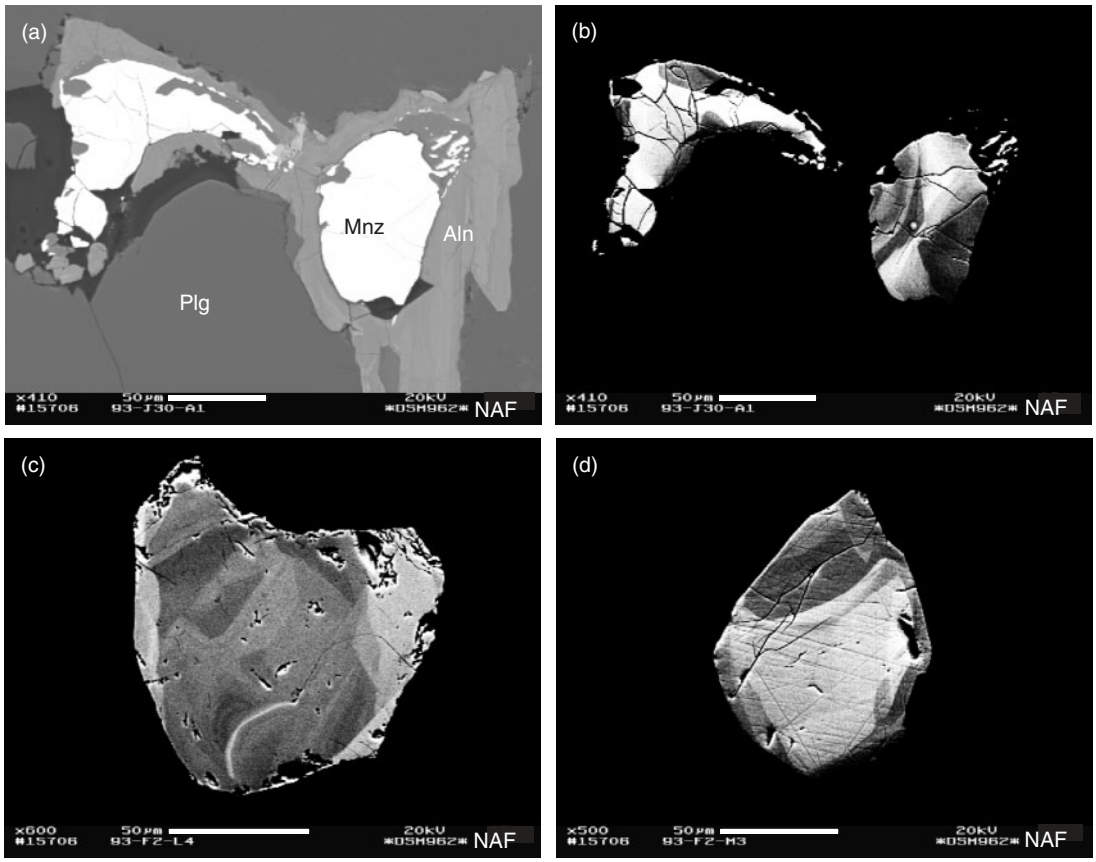

Fig. 13. High-contrast BSE images of a series of independent monazite grains (i.e. not associated with fluorapatite). (a) Allanite enclosing a monazite grain from the southern edge of the NAF. (b) High-contrast image of the monazite grains shown in (a). (b), (c), and (d) Zoned monazite grains showing various curvilinear ingrowths: the brighter the area, the higher the $ThSiO_4$–$CaTh(PO_4)_2$ component.

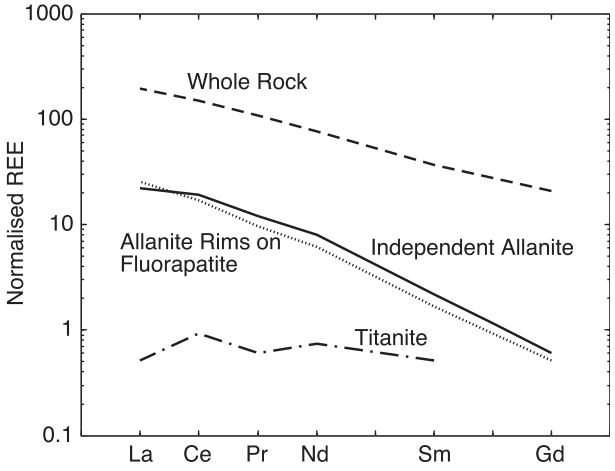

Fig. 14. Average chondrite-normalized (divided by 10 000) LREE patterns for independent allanite grains (continuous line; Table 9), allanite rims on fluorapatite (dotted line; Table 9), and titanite (dot–dash line; Table 11). Also included are whole-rock chondrite-normalized patterns from the NAF and northern CGF zones (dashed line; Table 2). The whole-rock plots were not divided by 10 000. For normalization the average chondrite composition of Anders & Grevesse (1989) was used.

grade could be due to oxidation/dehydration reactions such as

$$2\,\underset{\text{in biotite}}{KFe_3AlSi_3O_{10}(OH)_2} + 1{\cdot}5\,O_2 = 2\,\underset{\text{K–feldspar}}{KAlSi_3O_8} + 3\,\underset{\text{in ilmenite}}{Fe_2O_3} + 2\,H_2O \quad (5)$$

and

$$2\,\underset{\text{in hornblende}}{Ca_2Fe_5Si_8O_{22}(OH)_2} + 1{\cdot}5\,O_2 = 4\,\underset{\text{in clinopyroxene}}{CaFeSi_2O_6} + \underset{\text{quartz}}{SiO_2} + 3\,\underset{\text{in ilmenite}}{Fe_2O_3} + 2\,H_2O. \quad (6)$$

Biotite (Fig. 6c), amphibole (Fig. 7c), and orthopyroxene (Fig. 8b) all show a decrease in Mn concentrations southwards across the CGF zone, which is not reflected by a decrease in the whole-rock Mn concentrations (Fig. 2c). Garnet can preferentially incorporate Mn but is absent in the CGF where the major decrease in biotite, orthopyroxene and amphibole Mn concentrations occur. The decrease in Mn in these phases could be due to the partitioning of Mn into hemo-ilmenite. Although the concentration of Mn into hemo-ilmenite does not increase southwards, the abundance of hemo-ilmenite does (Harlov *et al.*, 1997; Harlov & Hansen, 2005).

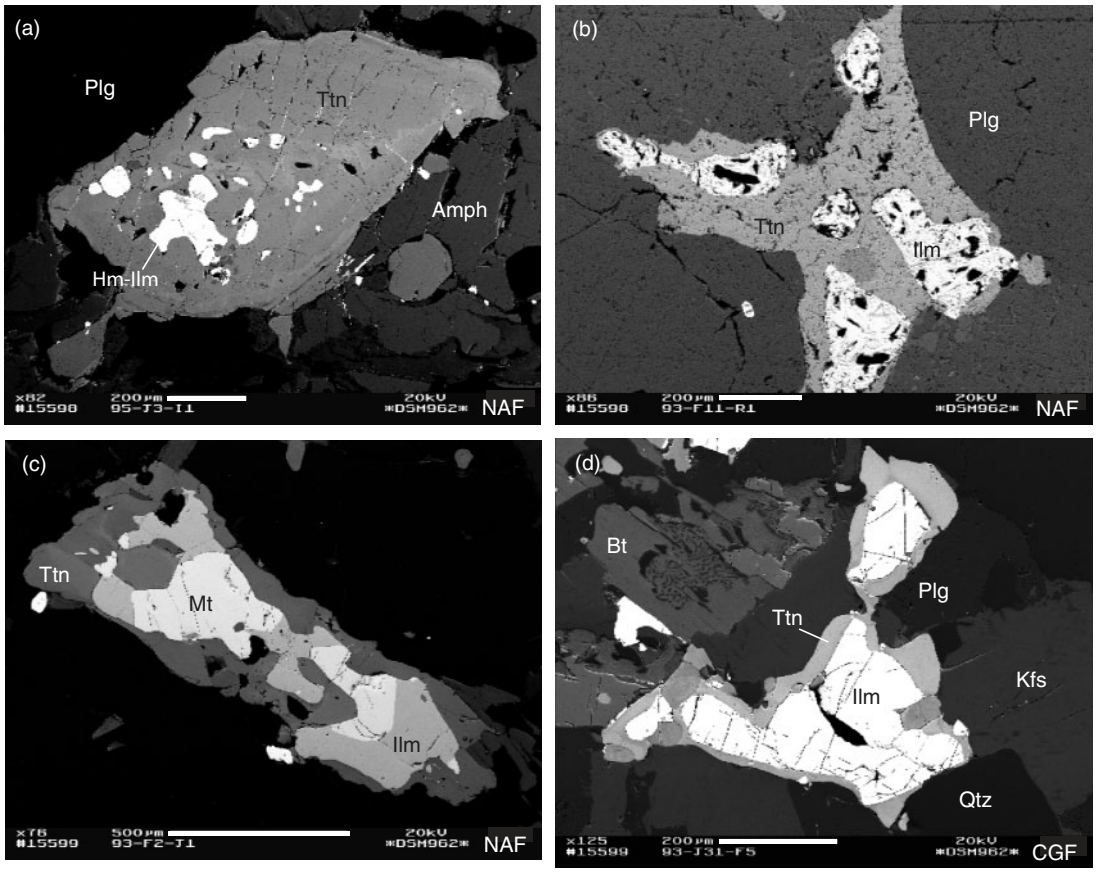

Fig. 15. BSE images of titanite–ilmenite associations for a series of samples across the northern amphibolite-facies zone (NAF). (a) Relatively small hemo-ilmenite inclusions in large titanite grains from the northern edge of the NAF. (b)–(d) Typical titanite–ilmenite relationships from the central and southern NAF. The faint zoning in the titanite in (a)–(c) should be noted. The lighter the area the higher the (Y + REE) concentration.

Biotite (Fig. 6d), amphibole (Fig. 7e) and fluorapatite (Fig. 10b) all tend to have higher F concentrations in the higher-grade rocks. Harlov & Förster (2002*a*, 2002*b*) found similar trends in fluorapatite and biotite across the two dehydration zones they investigated. In the case of fluorapatite this appears to be part of a general tendency for F concentrations to increase with increasing grade from greenschist to amphibolite facies (Kapustin, 1987; Spear & Pyle, 2002). The migration of an externally derived fluid relatively rich in F from higher to lower grade, as suggested by Harlov & Forster (2002*b*), would explain the increase in F concentrations.

However, the increase in F concentrations could also be due to the fractionation of F during the progressive breakdown of biotite and amphibole by any process that forms a fluid or a melt that takes in less F than do the Fe–Mg silicates. As long as the system remains closed, a decrease in the abundance of amphibole and biotite would be accompanied by an increase in the F concentrations in both the residual grains of these minerals and the fluorapatite grains in equilibrium with them. Figure 16 shows model calculations of F concentrations that, although too simple for modelling the natural systems in detail, can illustrate the general principle. Here the rock is assumed to initially contain 10% biotite with an F concentration of 0·5 wt % and 0·5% fluorapatite with an F concentration of 1 wt %. The ratio of F in the biotite to F in the fluid (or melt) was assumed to be 10 and the ratio of F in the biotite to F in the fluorapatite was assumed to be 0·5. These ratios were kept constant throughout the dehydration process. Calculations were performed using ratios of mass of biotite consumed to mass of fluid or melt produced of 1·0 (more appropriate for dehydration partial melting) and 0·04 (more appropriate for solid-state dehydration). As Fig. 16 shows, in both cases dehydration causes a smooth, progressive increase of F in both biotite and fluorapatite.

Fe–Mg silicate composition and H_2O activity

Orthopyroxene (Fig. 8c) and magnetite (Harlov & Hansen, 2005) have nearly constant Fe concentrations

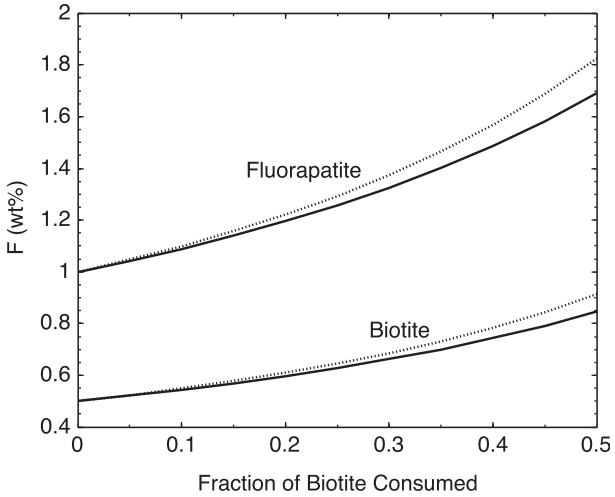

Fig. 16. The results of simple mass balance modelling of the effects of progressive dehydration reactions involving biotite on the F concentration of biotite and fluorapatite. The continuous lines are for the ratio (mass of biotite consumed)/(mass of fluid or melt produced) = 1 (dehydration melting), whereas the dotted lines are for the ratio (mass of biotite consumed)/(mass of fluid or melt produced) = 0·04 (solid-state dehydration). Calculation details are described in the text.

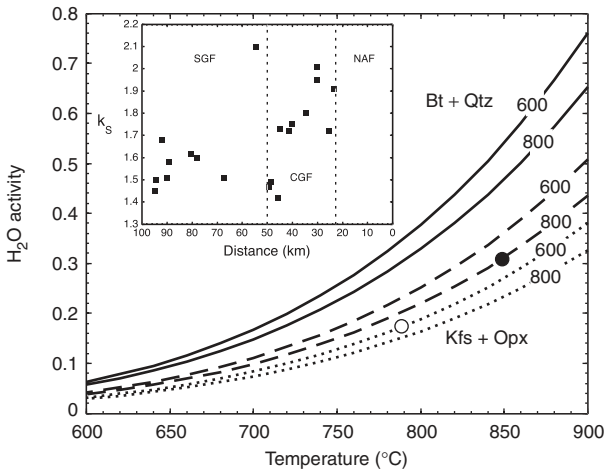

Fig. 17. Biotite breakdown reactions as a function of H_2O activity and temperature. The curves shown are for $k_s = 1$ [i.e. pure Mg end-members] (continuous line); $k_s = 1{\cdot}5$ (dashed line); $k_s = 2$ (dotted line) for pressures of 600 and 800 MPa. ●, $P-T$ conditions inferred for the SGF; ○, $P-T$ conditions inferred for the northern boundary of the CGF. Details of the calculations are given in the text. In the inset, k_s [$= (a^3_{En}a_{Or})/a_{Ph}$] is plotted as a function of distance along the traverse going southwards from the northernmost sample (i.e. 95 J3 I1; see Fig. 1). Dotted lines designate the approximate boundaries between the higher-grade southern granulite-facies zone (SGF), the lower-grade central granulite-facies zone (CGF) and the northern amphibolite-facies zone (NAF).

across the traverse. One of the consequences is that, with the exception of a handful of more reduced samples in the southern SGF, oxygen fugacities in these rocks are all buffered at approximately 2–3 log units above fayalite–magnetite–quartz (FMQ) (Harlov *et al.*, 1997; Harlov & Hansen, 2005). On the other hand, Fe concentrations in the amphibole and biotite decrease steadily as their abundance decreases across the CGF zone. The composition of these phases are in part determined by their equilibrium with the pyroxenes [i.e. reactions (1) and (2)].

Of these, the easiest to model is the reaction between orthopyroxene, K-feldspar, biotite, and quartz [i.e. reaction (1)]. From reaction (1) the following relationship for the H_2O activity may be derived:

$$a_{H_2O} = K_1/k_s \tag{7}$$

where

$$k_s = a^3_{En}a_{Or}/a_{Ph} \text{ and } K_1 = a_{H_2O}a^3_{En}a_{Or}/a_{Ph}. \tag{8}$$

Here K_1 is the equilibrium constant for reaction (1) at the pressure and temperature of interest. Figure 17 is a plot of k_s against distance from the northern boundary of the CGF. An ideal one-site mixing model was used for enstatite and K-feldspar. The activity of phlogopite was estimated using an ideal multi-site mixing model modified from Holland & Powell (1990):

$$a_{Ph} = 4X^A_K X^{M1}_{Mg}(X^{M2}_{Mg})^2 X^{T2}_{Al} X^{T2}_{Si}(X_{OH})^2. \tag{9}$$

Tetrahedral Al above the 1 atom per formula unit in the ideal phlogopite formula was first used to balance the charge on octahedral Al. The remaining excess tetrahedral Al was used to charge balance a fraction of the Ti. The charge on the rest of the Ti was balanced by vacancies (Henry & Guidotti, 2002) that were evenly distributed among the octahedral sites. As the majority of K-feldspar occurs as blebs along quartz–plagioclase grain boundaries, the composition of these blebs (Or = 0·95) was used in the calculations (Hansen *et al.*, 1995; Harlov *et al.*, 1998). Also shown in Fig. 17 are the positions of the biotite breakdown curve [reaction (1)] at 600 and 800 MPa as a function of temperature and H_2O activities for different values of k_s. These curves were calculated using the ΔG° for reaction (1) for enstatite and phlogopite derived by Aranovich & Newton (1998) from their experiments. H_2O fugacities were taken from Burnham *et al.* (1969).

With the exception of one anomalous sample (93 F3 O3), k_s for samples from the SGF lies within a relatively narrow range (1·45–1·62, average 1·55; Fig. 17). This suggests that throughout most of the SGF, the mineral assemblages record roughly the same H_2O activity. At 850°C and 800 MPa, the calculated range in H_2O activity is from 0·29 to 0·32. An increase in the Fe concentration in biotite relative to orthopyroxene, coupled with a decrease in the F concentration, causes k_s to increase from roughly 1·4 to 2·0 from south to north across the CGF (Fig. 17). Thus as Fig. 17

illustrates, the orthopyroxene–K-feldspar–biotite–quartz assemblage at the northern end of the CGF apparently records lower H_2O activities than the rocks at the southern end. However, there are several potential problems with these determinations. The isotherms in Fig. 17 are fairly close together at lower temperatures so that small errors in the calculation of k_s will lead to relatively large errors in the H_2O activity. The disproportionate effect of F or Ti in stabilizing biotite is probably not accounted for by the ideal mixing models used in these calculations. In many of the rocks K-feldspar is restricted to plagioclase–quartz grain boundary blebs or replacement antiperthite. Texturally the K-feldspar blebs are distinctly different than the larger quartz, plagioclase and orthopyroxene grains in the matrix. The blebs also have the wrong composition to be in equilibrium with plagioclase at high temperatures. Given all of these potential problems, perhaps the simplest conclusion here is that the mineral composition apparently does not record a clear decrease in H_2O activity as the proportions of H_2O-bearing minerals decrease southwards across the CGF into the SGF.

Accessory minerals and trace-element budgets

Different REE-rich accessory mineral populations occur in three separate areas along the Krishnagiri–Salem traverse (Fig. 1) that do not correspond exactly to the three metamorphic zones. In the SGF and southern CGF zone the principal REE-bearing accessory minerals are the monazite inclusions and rim grains associated with fluorapatite. The monazite and whole-rock LREE patterns (Fig. 11) are roughly parallel, suggesting that the monazite inclusions and rim grains could be the principal reservoir for these elements. Estimates based on comparisons between the reintegrated fluorapatite compositions (Table 10) and whole-rock compositions (Table 2) from this zone indicate that it would take 0·3–0·6 wt % (0·2–0·5 vol. %) monazite-bearing fluorapatite grains to account for the whole-rock LREE abundances. This is not out of line with the estimated modal abundances (~0·5%) for monazite-bearing fluorapatite grains.

In the northern half of the CGF and the southern quarter of the NAF (shaded region Fig. 1) independent monazite grains were found in 80% of the samples. Monazite inclusions and rim grains associated with fluorapatite are also found (Table 1). The chondrite-normalized, whole-rock REE patterns in these rocks are roughly parallel to the patterns for both the free monazite grains and monazite associated with fluorapatite. This would suggest that both types are probably the dominant REE reservoirs. Whole-rock Th concentrations drop sharply in approximately the same area where independent monazite grains almost completely disappear (compare Figs 1 and 12 with Fig. 3c), suggesting that independent monazite grains are the most important host for Th in this area. Uranium abundances also decrease in about the same region (Fig. 3d). However, because the monazite grains contain only small amounts of U (Tables 7 and 8), another mineral, probably zircon, must be the major host for U.

In the northern three-quarters of the NAF no monazite occurs either as independent grains or as inclusions and rim grains associated with fluorapatite. Both allanite and titanite in this area contain significant amounts of REE (Tables 9 and 11). The average whole-rock REE pattern is less LREE enriched than that of the allanite but more LREE enriched than that of titanite (Fig. 14). Together these two minerals may be the principal reservoir for these elements in this area. Despite the absence of monazite, Th abundances in the northern NAF are not low, indicating another host. The low Th abundances seen in allanite exclude it as a likely host for Th (see Table 9; Electronic Appendix 5).

Stähle *et al.* (1987), Raith & Srikantappa (1993), and Harlov *et al.* (2006a) all noted evidence for the selective depletion of (Y + HREE) in localized granulite-facies dehydration zones in amphibolite-facies gneisses. However, a selective depletion of (Y + HREE) is not evident along the Krishnagiri–Salem traverse. Instead, chondrite-normalized REE patterns from the SGF show less enrichment in LREE than do the patterns at lower grades (Fig. 4). Monazite inclusions and rim grains associated with fluorapatite are less enriched in LREE than are the independent monazite of the southern NAF and northern CGF (Figs 11 and 12). Finally, the proportion of monazite inclusions in fluorapatite that show the least LREE enrichment (Population II) increases southwards with increasing grade (Fig. 12). These features all indicate that if there was any REE depletion along the Krishnagiri–Salem traverse it involved the selective removal of LREE from the higher-grade rocks.

Unless the present-day distribution of monazite and Th simply reflects their original distributions in the orthogneiss protoliths along the Krishnagiri–Salem traverse (Fig. 1), then the loss of monazite and the concomitant decrease in Th abundance in the central CGF is a metamorphic effect. The decline in REE abundances in this area is much less pronounced (Fig. 3e) than the decrease in Th abundances (Fig. 3c), implying that, if it occurred at all, the loss of REE was much smaller. The main reservoirs of REE in the southern part of the traverse are apparently the monazite inclusions in fluorapatite grains. Thus it appears that independent monazite was probably replaced by the precursors of the monazite-bearing fluorapatite grains (see next section) during prograde metamorphism.

Bingen *et al.* (1996) described an amphibolite- to granulite-facies transition within orthogneisses from Rogaland–Vest-Agder, southwestern Norway, in which monazite also occurs in a relatively narrow zone.

They attributed the appearance of monazite at the clinopyroxene-in isograd to a prograde reaction involving the breakdown of allanite, titanite and amphibole and the decline in monazite abundance after the orthopyroxene-in isograd to a prograde fluorapatite-forming reaction. As a consequence, a relatively narrow zone, containing discrete monazite grains between a titanite–allanite zone (similar to the northern NAF) coupled with a zone that contains either REE-enriched fluorapatite (as in Rogaland–Vest-Agder) or fluorapatite with monazite inclusions (similar to what is seen in the SGF and CGF), may be a common feature in high-grade terranes.

Formation of monazite inclusions

The close association of monazite and fluorapatite, the evidence for crystallographic control with respect to the orientation of many of the inclusions, and the negligible amounts of Th in the monazite inclusions and rim grains all indicate that it formed *in situ* from a REE-bearing fluorapatite (Harlov & Förster, 2003). Experimentally, monazite has been produced by the incongruent melting of fluorapatite in peraluminous granitic melts (Wolf & London, 1995). These experiments produced trails of monazite grains in the melt in the immediate vicinity of the fluorapatite rim but no monazite inclusions. As a consequence, the resulting textures are distinctly different from those seen along the Krishnagiri–Salem traverse (Fig. 9). On the other hand, fluorapatite–monazite textures (both inclusions and rim grains) very similar to those in the CGF and SGF have been replicated experimentally by the reaction of (Y + REE)-bearing fluorapatite with fluids including H_2O, KCl brines, and acids such as 1M HCl and H_2SO_4 in a process involving metasomatism of the host fluorapatite via dissolution and reprecipitation (see Harlov *et al.*, 2002, 2005; Harlov & Förster, 2003).

Britholite ($Ca_2REE_3Si_3O_{12}F$) appears to be the main REE-bearing component in the fluorapatite (Table 6). In a quartz-saturated system monazite could form by the following reaction between a britholite-bearing fluorapatite and a fluid:

$$\underset{\text{britholite component}}{Ca_2REE_3Si_3O_{12}F} + \underset{\text{fluorapatite}}{Ca_5P_3O_{12}F} + 14\,H^+ = 3\,\underset{\text{monazite}}{(REE)PO_4} + 3\,\underset{\text{quartz}}{SiO_2} + 7\,Ca^{2+} + 6\,H_2O + 2\,HF. \quad (10)$$

As this reaction indicates, a decrease in pH and decreases in the H_2O activity, Ca activity, and HF activity will all drive this reaction to the right, leading to the formation of monazite. A change in pressure and temperature could conceivably do the same thing.

Sample 93 J31 F5 from the northern CGF is particularly significant when considering the origin of monazite inclusions. The fluorapatite in this sample contains occasional monazite inclusions but they are much less abundant than in other samples from the same area (Fig. 9a). At the same time, the fluorapatite grains contain bright zones that have REE abundances that are higher ($REE_2O_3 = 2{\cdot}5$ wt %) than most of the estimated compositions of fluorapatite grains before the formation of monazite inclusions (Electronic Appendix 3). Sample 93 J31 F5 has the same mineralogy as other samples in the area and presumably has the same *P–T* history. Thus, the formation of monazite inclusions and rim grains cannot be a simple consequence of changes in temperature or pressure [see also the discussion by Harlov *et al.* (2005)]. If, on the other hand, the formation of monazite inclusions resulted from a change in the composition of the metamorphic fluid, then the combination of a relatively low fluid to rock ratio and a high initial REE content (which would require more fluid for the reaction to go to completion) could explain the survival of high-REE fluorapatite in sample 93 J31 F5.

The role of melts and fluids in the granulite-grade metamorphism

If the grain boundary K-feldspar blebs do represent melt pools, then their presence throughout the Krishnagiri–Salem traverse (Table 1) suggests that the entire area either has undergone partial melting or has been infiltrated by a melt. There is also a rough tendency for orthogneisses north of the orthopyroxene isograd to have somewhat lower concentrations of SiO_2 and K_2O than orthogneisses south of the isograd; a relationship to be expected if a K- and Si-rich partial melt had been extracted from the higher-grade portion of the traverse. Many of the changes in mineral proportions and composition southwards across the CGF could be explained by dehydration-melting reactions of the form

$$\text{biotite} + \text{feldspar} + \text{quartz} = \text{orthopyroxene} + \text{hemo-ilmenite} + \text{melt} \quad (11)$$

and

$$\text{hornblende} + \text{feldspar} + \text{quartz} = \text{clinopyroxene} + \text{orthopyroxene} + \text{hemo-ilmenite} + \text{melt}. \quad (12)$$

This would assume that the protolith was already highly oxidized. Some of the melt produced by these reactions could have migrated out of the rock whereas some of it could have solidified *in situ* forming the K-feldspar blebs. Upon cooling, residual fluids along grain boundaries would have reacted with orthopyroxene and clinopyroxene to form the relatively small biotite and amphibole grains commonly associated with pyroxenes in samples from the CGF and SGF. These back-reactions would buffer the system to relatively low H_2O activities, thereby ensuring the long-term preservation of orthopyroxene and clinopyroxene (Yardley & Valley, 1997).

Unless the low Rb, Cs, U, and Th abundances are a feature of the premetamorphic protolith (e.g. Rollinson &

Tarney, 2005), these elements must have been carried out of the orthogneisses in the SGF and southern CGF by some agent. A migrating partial melt is one possibility. However, biotite from Rb-depleted rocks in this area has much lower abundances of Rb than does biotite from undepleted rocks, and, given what is known about the partition coefficients, this is a very difficult pattern to produce by partial melting (Hansen *et al.*, 2002). Thorium depletion appears to have coincided with the consumption of free monazite grains in a reaction that produced REE-enriched fluorapatite. However, monazite is generally much less soluble than fluorapatite in partial melts of approximate granitic compositions (Wolf & London, 1995). Hence partial melting could be expected to produce the opposite effect. Thus, partitioning into a migrating fluid phase may more easily explain the pattern of trace-element depletion.

Any fluid involved in trace-element depletion, able to transport these trace elements, must have had a low H_2O activity in order to be in equilibrium with orthopyroxene-bearing assemblages, and must have been able to flow extensively through the rocks along grain boundaries on the kilometre scale. High-temperature, high-pressure brines have these properties and it has been suggested that they play an important part in granulite-facies metamorphism (Aranovich & Newton, 1996, 1997; Newton *et al.*, 1998). Hansen *et al.* (1995) suggested that high-grade metamorphism in this area was accompanied by an influx of concentrated brines released by the crystallization of mafic magmas at the base of the crust. As these low H_2O activity fluids migrated upwards through the crust they would have driven reactions (1) and (2) to the right, accounting for the progressive north to south replacement of biotite and amphibole by clinopyroxene and orthopyroxene and the enrichment of amphibole in K_2O. Newton & Manning (2005) have noted that deep-seated brines could contain oxidizing agents such as $CaSO_4$ in relatively large amounts. The upward migration of these brines would therefore drive reactions (5) and (6) to the right, accounting for both the southward increase in hemo-ilmenite and decreases in Fe and Mn in biotite and amphibole. Migrating brines may also have carried away some of the K released during biotite breakdown and could have also redistributed some of the K into replacement antiperthite and K-feldspar blebs along plagioclase–quartz grain boundaries via reactions (3) and (4). Hansen *et al.* (2002) have shown that partitioning of Rb into migrating brines can account for the Rb depletion in both whole-rock and biotite compositions in the SGF and southern CGF.

As brines migrated upwards through the crust they initially drove reaction (10) to the left, replacing the independent monazite grains with REE-bearing fluorapatite and releasing Th. Later changes in the composition of the fluid, perhaps accompanied by decreases in pressure and temperature during uplift, drove reaction (10) to the right, leading to the formation of the low-Th monazite inclusions and rim grains. In the Rogaland–Vest-Agder area monazite breakdown was accompanied by the formation of thorite and Th-bearing fluorapatite grains (Bingen *et al.*, 1996). Neither of these minerals is important along the Krishnagiri–Salem traverse and Th appears to have been transported out of the rocks. There is some experimental evidence (Oelkers & Poitrasson, 2002; Schmidt *et al.*, 2007) that in monazite-bearing systems, Th mobility increases as pH increases. In addition, as reaction (10) indicates, at higher pH monazite should be less stable relative to a britholite component in fluorapatite. Monazite breakdown was not accompanied by removal of HREE, although there may have been a slight depletion in LREE (Figs 11 and 12). Both experiments and theoretical calculations (Haas *et al.*, 1995; Pan & Fleet, 1996; Schmidt *et al.*, 2007) indicate that under high-grade conditions Cl enhances the mobility of LREE and F enhances the mobility of HREE. The southern edge of the free monazite zone coincides with elevated levels of Cl in fluorapatite (Fig. 10c) and biotite (Fig. 6e), which may indicate that during the breakdown of monazite the fluids were relatively high in Cl.

Partial melting and the upward migration of concentrated brines are not mutually exclusive. Thus dehydration melting may have preceded or even accompanied the movement of brines into the rocks. It is possible that many of the changes in mineralogy and major-element mineral composition may be due to dehydration melting reactions whereas the trace-element depletions are largely due to migrating brines.

CONCLUSIONS

The north (higher crustal levels) to south (lower crustal levels), amphibolite- to granulite-facies transition in intermediate to felsic orthogneisses along the Krishnagiri–Salem traverse is characterized by a number of systematic changes in mineralogy and both whole-rock and mineral composition.

(1) Biotite and amphibole are the dominant Fe–Mg silicates in the north of the traverse. Moving southwards, first clinopyroxene and then orthopyroxene appear. As the abundances of amphibole and biotite decrease southwards, the abundances of orthopyroxene and hemo-ilmenite increase.

(2) Systematic decreases in Fe and Mn in biotite and amphibole and increases in K in amphibole with increasing grade cannot be accounted for by changes in whole-rock composition, but appear to be an effect of dehydration and dehydration/oxidation reactions. Increases in F in biotite and fluorapatite with

increasing grade can be accounted for by any biotite breakdown reaction in which the reaction products have less of an affinity for F than does biotite.

(3) The principal host for REE shifts from allanite and titanite north of the clinopyroxene isograd, to independent monazite grains in the central part of the traverse, and to monazite inclusions and rim grains in fluorapatite in the southern portion.

(4) Low whole-rock abundances of Rb, Cs, Th, and U become common 15–20 km south of the orthopyroxene isograd. The depletion of Th appears to be related to the replacement of independent monazite grains by REE-bearing fluorapatite grains. Monazite inclusions formed in these fluorapatite grains later in the history of the rocks.

(5) K-feldspar blebs occur along plagioclase and quartz grain boundaries throughout the traverse. In contrast, K-feldspar 'replacement' antiperthite is common only in the southern high-grade portion.

These features can all be accounted for by a model in which concentrated low H_2O activity brines migrate upward from a source lower in the crust. However, the evidence does not rule out the possibility that the influx of this brine was preceded or accompanied by dehydration melting.

ACKNOWLEDGEMENTS

We thank Helga Kemnitz for assistance with the SEM, as well as Dieter Rhede and Oona Appelt for help with the electron microprobe analyses at the GeoForschungsZentrum Potsdam. We thank Wolfgang Seifert for obtaining the titanite analyses. We especially thank Peter Dulski for his hard work in obtaining trace-element REE analyses for approximately half the samples at the GeoForschungsZentrum. The manuscript was improved as a result of reviews from Bernard Bingen, Robert C. Newton, and an anonymous reviewer. This work was supported by an India–US co-operative research grant from the US National Science Foundation, #INT-9117842 to Bob Newton and E.C.H. We also thank the GeoForschungsZentrum Potsdam and Hope College, which helped to finance E.C.H.'s trips to the GeoForschungsZentrum Potsdam, where this paper was researched and written.

SUPPLEMENTARY DATA

Supplementary data for this paper are available at *Journal of Petrology* online.

REFERENCES

Anders, E. & Grevesse, N. (1989). Abundances of the elements: meteoritic and solar. *Geochimica et Cosmochimica Acta* **53**, 197–214.

Aranovich, L. Ya. & Berman, R. G. (1997). A new garnet–orthopyroxene thermometer based on reversed Al_2O_3 solubility in $FeO–Al_2O_3–SiO_2$ orthopyroxene. *American Mineralogist* **82**, 345–353.

Aranovich, L. Ya. & Newton, R. C. (1996). H_2O activity in concentrated NaCl solutions at high pressures and temperatures measured by the brucite–periclase equilibrium. *Contributions to Mineralogy and Petrology* **125**, 200–212.

Aranovich, L. Ya. & Newton, R. C. (1997). H_2O activity in concentrated NaCl solutions at high pressures and temperatures measured by the brucite–periclase equilibrium. *Contributions to Mineralogy and Petrology* **127**, 261–271.

Aranovich, L. Y. & Newton, R. C. (1998). Reversed determination of the reaction: phlogopite + quartz = enstatite + potassium feldspar + H_2O in the ranges 750–875°C and 2–12 kbar at low H_2O activity with concentrated KCl solutions. *American Mineralogist* **83**, 193–204.

Bingen, B., Demaiffe, D. & Hertogen, J. (1996). Redistribution of rare earth elements, thorium and uranium over accessory minerals in the course of amphibolite- to granulite-facies metamorphism: the role of apatite and monazite in orthogneisses from southwestern Norway. *Geochimica et Cosmochimica Acta* **60**, 1341–1354.

Burnham, C. W., Holloway, J. R. & Davis, N. F. (1969). Thermodynamic properties of water to 1,000°C and 10,000 bars. *Geological Society of America, Special Papers* **132**, 1–96.

Collerson, K. D. & Fryer, B. J. (1978). The role of fluids in the formation and subsequent development of early continental crust. *Contributions to Mineralogy and Petrology* **67**, 151–167.

Condie, K. C. & Allen, P. (1984). Origin of Archean charnockites from southern India. In: Kroner, A., Hansen, G. N. & Goodwin, A. M. (eds) *Archean Geochemistry*. Berlin: Springer, pp. 182–203.

Condie, K. C., Allen, P. & Narayana, B. L. (1982). Geochemistry of the Archean low- to high- grade transition zone, southern India. *Contributions to Mineralogy and Petrology* **81**, 157–167.

Dulski, P. (2001). Reference materials for geochemical studies: new analytical data by ICP-MS and critical discussion of reference values. *Geostandards Newsletter* **25**, 87–125.

Ferreira Filho, C. F., DeMoraes, R., Fawcett, J. J. & Naldret, A. J. (1998). Amphibolite to granulite progressive metamorphism in the Niquelândiq Complex, central Brazil, regional tectonic implications. *Journal of South American Earth Sciences* **2**, 35–50.

Franz, L. & Harlov, D. E. (1998). High-grade K-feldspar veining in granulites from the Ivrea–Verbano Zone, northern Italy: fluid flow in the lower crust and implications for granulite facies genesis. *Journal of Geology* **106**, 455–472.

Frost, B. R. & Frost, C. D. (1987). CO_2 melts and granulite metamorphism. *Nature* **327**, 503–506.

Griffin, W. L. (1969). Replacement antiperthite in gneisses of the Babbit–Embarrass area, Minnesota, USA. *Lithos* **2**, 171–186.

Haas, J. R., Shock, E. L. & Sasani, D. C. (1995). Rare earth elements in hydrothermal systems: estimates of standard partial molal thermodynamic properties of aqueous complexes of the rare earth elements at high pressures and temperatures. *Geochimica et Cosmochimica Acta* **59**, 4329–4350.

Hansen, E. C., Newton, R. C., Janardhan, A. S. & Lindenberg, S. (1995). Differentiation of Late Archean crust in the eastern Dharwar Craton, Krishnagiri–Salem Area, South India. *Journal of Geology* **103**, 629–651.

Hansen, E., Harlov, D. E. & Bigler, C. J. (1997). Non-silicate mineralogy and mineral chemistry along a late Archean, deep-crustal profile in South India. *Geological Society of America, Abstracts with Programs* **29**, 398.

Hansen, E. C., Khurram, A. & Harlov, D. E. (2002). Rb depletion in biotites and whole rocks across an amphibolite- to granulite-facies transition zone, Tamil Nadu, south India. *Lithos* **64**, 29–47.

Harlov, D. (2005). KCl metasomatism in the lower crust: nature and experiment. *Geochimica et Cosmochimica Acta* **69**, A660.

Harlov, D. E. & Förster, H.-J. (2002a). High-grade fluid metasomatism on both a local and regional scale: the Seward Peninsula, Alaska and the Val Strona di Omegna, Ivrea–Verbano Zone, northern Italy part I: Petrography and silicate mineral chemistry. *Journal of Petrology* **43**, 769–799.

Harlov, D. E. & Förster, H.-J. (2002b). High-grade fluid metasomatism on both a local and regional scale: the Seward Peninsula, Alaska and the Val Strona di Omegna, Ivrea–Verbano Zone, northern Italy Part II: Phosphate mineral chemistry. *Journal of Petrology* **43**, 801–824.

Harlov, D. E. & Förster, H.-J. (2003). Fluid-induced nucleation of (Y + REE)-phosphate minerals within apatite: nature and experiment. Part II. Fluorapatite. *American Mineralogist* **88**, 1209–1229.

Harlov, D. E. & Hansen, E. C. (2005). Oxide and sulphide isograds along a late Archean, deep-crustal profile in Tamil Nadu, south India. *Journal of Metamorphic Geology* **23**, 241–259.

Harlov, D. E., Newton, R. C., Hansen, E. C. & Janardhan, A. S. (1997). Oxide and sulphide minerals in highly oxidized, Rb-depleted, Archaean granulites of the Shevaroy Hills Massif, South India: oxidation states and the role of metamorphic fluids. *Journal of Metamorphic Geology* **15**, 701–717.

Harlov, D. E., Hansen, E. C. & Bigler, C. (1998). Petrologic evidence for K-feldspar metasomatism in granulite-facies rocks. *Chemical Geology* **151**, 373–386.

Harlov, D. E., Förster, H.-J. & Nijland, T. G. (2002). Fluid-induced nucleation of REE-phosphate minerals in apatite: nature and experiment. Part I. Chlorapatite. *American Mineralogist* **87**, 245–261.

Harlov, D. E., Wirth, R. & Förster, H.-J. (2005). An experimental study of dissolution–reprecipitation in fluorapatite: fluid infiltration and the formation of monazite. *Contributions to Mineralogy and Petrology* **150**, 268–286.

Harlov, D. E., Johansson, L., Van den Kerkhof, A. & Förster, H.-J. (2006a). The role of advective fluid flow and diffusion during localized, solid-state dehydration: Söndrum Stenhuggeriet, Halmstad, SW Sweden. *Journal of Petrology* **47**, 3–33.

Harlov, D. E., Tropper, R., Seifert, W., Nijland, T. & Förster, H.-J. (2006*b*). Formation of Al-rich titanite ($CaTiSiO_4$–$CaAlSiO_4OH$) reaction rims on ilmenite in metamorphic rocks as a function of f_{H_2O} and f_{O_2}. *Lithos* **88**, 72–84.

Harlov, D. E., Wirth, R. & Hetherington, C. J. (2007). The relative stability of monazite and huttonite at 300–900°C and 200–1000 MPa: metasomatism and the propagation of metastable mineral phases. *American Mineralogist* (in press).

Henry, D. J. & Guidotti, C. (2002). Titanium in biotite from metapelitic rocks: temperature effects, crystal-chemical controls, and petrological applications. *American Mineralogist* **87**, 375–382.

Holland, T. J. B. & Powell, R. (1990). An enlarged and updated internally consistent thermodynamic dataset with uncertainties and correlations; the system K_2O–Na_2O–CaO–MgO–MnO–FeO–Fe_2O_3–Al_2O_3–TiO_2–SiO_2–C–H_2–O_2. *Journal of Metamorphic Geology* **8**, 89–124.

Jarosewich, E. & Boatner, L. A. (1991). Rare-earth element reference samples for electron microprobe analysis. *Geostandards Newsletter* **15**, 397–399.

Jarosewich, E., Nelen, J. A. & Norberg, J. A. (1980). Reference samples for electron microprobe analysis. *Geostandards Newsletter* **4**, 43–47.

Kapustin, Y. L. (1987). The composition of apatite from metamorphic rocks. *Geochemistry International* **4**, 45–51.

Morishita, T., Arai, S. & Green, D. H. (2003). Evolution of low-Al orthopyroxene in the Horoman peridotite, Japan: an unusual indicator of metasomatizing fluids. *Journal of Petrology* **44**, 1237–1246.

Munoz, J. L. (1992). Calculation of HF and HCl fugacities from biotite compositions: revised equations. *Geological Society of America, Abstracts with Programs* **26**, 221.

Newton, R. C. & Manning, C. E. (2005). Solubility of anhydrite, $CaSO_4$ in NaCl–H_2O solutions at high pressures and temperatures: applications to fluid–rock interaction. *Journal of Petrology* **46**, 701–716.

Newton, R. C., Aranovich, L. Ya., Hansen, E. C. & Vanderheuvel, B. A. (1998). Hypersaline fluids in Precambrian deep-crustal metamorphism. *Precambrian Research* **91**, 41–63.

Nijland, T. G., Touret, J. L. R. & Visser, D. (1998). Anomalously low temperature orthopyroxene, spinel, and sapphirine occurrences in metasediments from the Bamble amphibolite- to granulite-facies transition zone (south Norway): possible evidence for localized action of saline fluids. *Journal of Geology* **106**, 575–590.

O'Connor, J. T. (1965). A classification for quartz-rich igneous rocks based on feldspar ratios. *US Geological Survey Professional Papers* **525B**, 79–84.

Oelkers, E. H. & Poitrasson, F. (2002). An experimental study of the dissolution stoichiometry and rates of a natural monazite as a function of temperature from 50 to 230°C and pH from 1·5 to 10. *Chemical Geology* **191**, 73–87.

Pan, Y. & Fleet, M. E. (1996). Rare earth element mobility during prograde granulite-facies metamorphism: significance of fluorine. *Contributions to Mineralogy and Petrology* **123**, 251–262.

Pattison, D. R. M., Chacko, T., Farquhar, J. & McFarlane, R. M. (2003). Temperature of granulite-facies metamorphism: constraints from experimental phase equilibria and thermobarometry corrected for retrograde exchange. *Journal of Petrology* **44**, 867–900.

Perchuk, L. L. & Gerya, T. V. (1992). The fluid regime of metamorphism and the charnockite reaction in granulites: a review. *International Geological Reviews* **34**, 1–58.

Peucat, J. J., Mahabaleswar, B. & Jayanada, M. (1993). Age of younger tonalitic magmatism and granulite metamorphism in the South Indian transition zone (Krishnigiri area); comparison with older Peninsular gneisses from the Gorur–Hasssan area. *Journal of Metamorphic Geology* **11**, 879–888.

Pouchou, J. L. & Pichoir, F. (1985). 'PAP' (φ–r–Z) procedure for improved quantitative microanalysis. In: Armstrong, J. T. (ed.) *Microbeam Analysis*. San Francisco, CA: San Francisco Press, pp. 104–106.

Pride, C. & Muecke, G. K. (1980). Rare earth element geochemistry of the Scourian Complex, N.W. Scotland—evidence for the granite–granulite link. *Contributions to Mineralogy and Petrology* **73**, 403–412.

Pyle, J. M., Spear, F. S. & Wark, D. A. (2002). Electron microprobe analyses of REE in apatite, monazite and xenotime: protocols and pitfalls. In: Kohn, J. M., Rakovan, J. & Hughes, J. M. (eds) *Phosphates: Geochemical, Geobiological and Materials Importance. Mineralogical Society of America, Reviews in Mineralogy and Geochemistry* **48**, 337–362.

Raase, P., Raith, M., Ackermand, D. & Lal, R. K. (1986). Progressive metamorphism of mafic rocks from the greenschist- to granulite-facies in the Dharwar Craton of South India. *Journal of Geology* **94**, 261–282.

Raith, M. & Srikantappa, C. (1993). Arrested charnockite formation at Kottavattam, southern India. *Journal of Metamorphic Geology* **11**, 815–832.

Rameshwar Rao, D., Narayanana, B. L. & Balaram, V. (1991a). Nature and origin of lower crustal rocks of Dhamapuri area, Tamil Nadu, southern India—a geochemical approach. *Geochemical Journal* **25**, 57–74.

Rameshwar Rao, D., Charan, S. N. & Natarajan, R. (1991b). *P–T* conditions and geothermal gradient of gneiss–enderbite rocks: Dhamapuri area, Tamil Nadu, India. *Journal of Petrology* **32**, 539–554.

Rollinson, H. R. & Tarney, J. (2005). Adakites—the key to understanding LILE depletion in granulites. *Lithos* **79**, 61–81.

Rudnick, R. L. & Presper, T. (1990). Geochemistry of intermediate to high pressure granulites. In: Vielzeuf, D. & Vidal, P. (eds) *Granulites and Crustal Evolution*. Dordrecht: Kluwer Academic, pp. 523–550.

Rudnick, R. L., McLennan, S. M. & Taylor, S. R. (1985). Large ion lithophile elements in rocks from high-pressure granulite-facies terrains. *Geochimica et Cosmochimica Acta* **49**, 1645–1655.

Sawyer, E. R. (2001). Melt segregation in the continental crust: distribution and movement of melt in anatectic rocks. *Journal of Metamorphic Geology* **19**, 291–309.

Schmidt, C., Rickers, K., Bilderback, D. H. & Huang, R. (2007). *In situ* SR-XRF study of REE phosphate dissolution in aqueous fluids to 800°C. *Lithos* **95**, 87–102.

Spear, F. S. & Pyle, J. M. (2002). Apatite, monazite, and xenotime in metamorphic rocks. In: Kohn, M. J., Rakovan, J. & Hughes, J. M. (eds) *Phosphates: Geochemical, Geobiological and Materials Importance. Mineralogical Society of America, Reviews in Mineralogy and Geochemistry* **48**, 293–331.

Stähle, H. J., Raith, M., Hoernes, S. & Delfs, A. (1987). Element mobility during incipient granulite formation at Kabbaldurga, Southern India. *Journal of Petrology* **28**, 803–834.

Stormer, J. C., Jr, Pierson, M. J. & Tacker, R. C. (1993). Variation of F and Cl X-ray intensity due to anisotropic diffusion of apatite during electron microprobe analyses. *American Mineralogist* **78**, 641–648.

Todd, C. S. & Evans, B. W. (1994). Properties of CO_2-induced dehydration of amphibole. *Journal of Petrology* **35**, 1213–1239.

Wolf, M. B. & London, D. (1995). Incongruent dissolution of REE- and Sr- rich apatite in peraluminous granitic liquids: differential apatite, monazite and xenotime solubilities during anatexis. *American Mineralogist* **80**, 765–775.

Yardley, B. W. D. & Valley, J. W. (1997). The petrologic case for a dry lower crust. *Journal of Geophysical Research* **102**, 12173–12185.